

## Experimental Vision Studies of Flow and Structural Effects on Wind Turbines

**Najafi, Nadia; Schmidt Paulsen, Uwe; Mann, Jakob; Sjöholm, Mikael**

*Publication date:*  
2015

*Document Version*  
Publisher's PDF, also known as Version of record

[Link back to DTU Orbit](#)

*Citation (APA):*  
Najafi, N., Schmidt Paulsen, U., Mann, J., & Sjöholm, M. (2015). Experimental Vision Studies of Flow and Structural Effects on Wind Turbines. DTU Wind Energy. (DTU Wind Energy PhD; No. 0055(EN)).

### DTU Library

Technical Information Center of Denmark

---

#### General rights

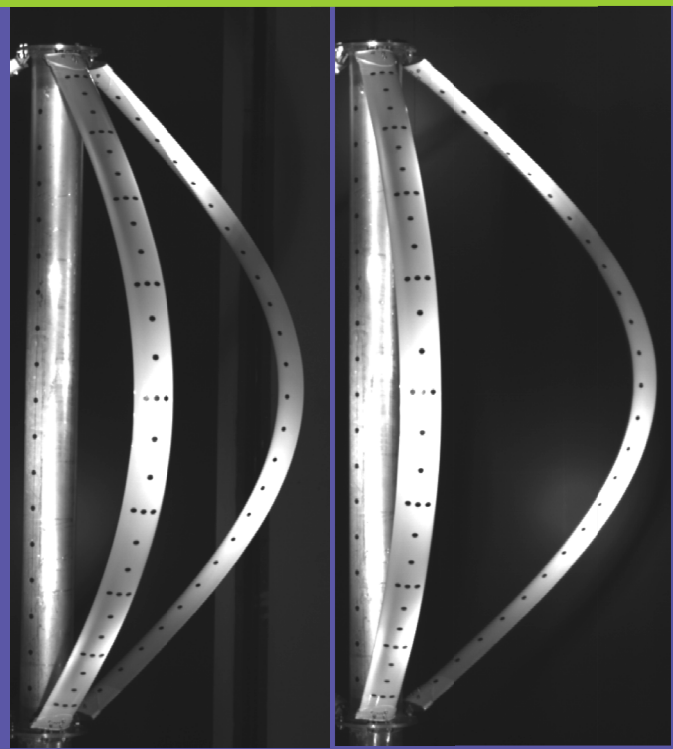
Copyright and moral rights for the publications made accessible in the public portal are retained by the authors and/or other copyright owners and it is a condition of accessing publications that users recognise and abide by the legal requirements associated with these rights.

- Users may download and print one copy of any publication from the public portal for the purpose of private study or research.
- You may not further distribute the material or use it for any profit-making activity or commercial gain
- You may freely distribute the URL identifying the publication in the public portal

If you believe that this document breaches copyright please contact us providing details, and we will remove access to the work immediately and investigate your claim.

# Experimental Vision Studies of Flow and Structural Effects on Wind Turbines

Department of  
Wind Energy  
PhD Report 2015



Nadia Najafi

DTU Wind Energy PhD-0055 (EN)

August 2015





**Authors:** Nadia Najafi

**Title:** Experimental Vision Studies of Flow and Structural Effects on Wind Turbines

**Department:** Wind Energy

### **Abstract**

In the present thesis we have developed and used two modern vision technologies to study wind turbines: stereo vision to study dynamics of a Vertical Axis Wind Turbine (VAWT) via Operational Modal Analysis (OMA) and Background-oriented schlieren method (BOS) to study tip vortices of a Horizontal Axis Wind Turbine (HAWT) blade.

The thesis starts with an introduction to stereo vision and OMA and it is followed by two practical implementations of those two techniques. In the first experiment which is conducted on a VAWT blade, we developed the image processing tools for obtaining the displacement time series from the images. Afterwards we devised an averaged approach of the covariance SSI (COV-SSI) method which enables us to involve short measurement sets in OMA. The first four natural frequencies are identified in this experiment which fairly agreed with classical modal analysis (EMA) and finite element simulation (FEM). In the second experiment the displacement time series of a three bladed VAWT rotor in a wind tunnel is obtained with an improved image processing algorithm while one of the blades was missing in the images due to the hardware limitations. In OMA part, we have developed the DD-SSI and FDD codes for studying the dynamic behaviour of the turbine. The structural modes of the VAWT which are obtained with OMA are validated with the simulation and the classical modal analysis and then the differences are explained with aerodynamic effect and boundary conditions. The other frequencies obtained by OMA, are interpreted via vortex shedding phenomena and guy wire effects. The uncertainty of the obtained displacement time series via stereo vision in the two above-mentioned experiments is evaluated by the law of error propagation and several solutions are presented to decrease the uncertainty in the stereo vision experiments.

In the last part of the thesis, the BOS method has been used to study the tip vortices behind a Nordtank HAWT based on the density gradient in the vortex core. BOS does not need complicated equipment such as special cameras or seeded flow which makes it a convenient method to study big scale flows. But the challenging part in the current case is the small refractive index change due to the small Mach number in the flow behind the HAWT. This issue has been addressed in the last chapter by designing a proper experiment setup according to the preliminary estimation of the vortex. The changes due to the vortex are modelled and the tip vortex properties such as vortex size, density distribution and the maximum pressure drop in the vortex core are estimated successfully by comparison between the model and the experiment observations.

**August 2015**

**Project Period:**  
2012.03.01-2015.08.31

**Education:**  
Doctor of Philosophy

**Field:**  
Wind Energy

**Supervisors:**  
Uwe S.Paulsen  
Jakob Mann  
Mikael Sjöholm

**Project no.:**  
DTU Wind Energy PhD-0055 (EN)

**Technical University of Denmark**  
Department of Wind Energy  
Frederiksborgvej 399  
Building 118  
4000 Roskilde  
Denmark  
Telephone

[www.vindenergi.dtu.dk](http://www.vindenergi.dtu.dk)

# Preface

The present research was conducted during 2012–2015 at Denmark Technical University (DTU), wind energy department. This project was partly supported by the European DeepWind project and grant supported by the DTU Wind Energy department.

Initially, it was planned to study the motions of an operating floating kW-sized VAWT (DeepWind demonstrator) in the main part of this PhD and the hardware had been granted via the project. This was subjected to changes due to some technical problems of not having the VAWT for testing at the site. Therefore it has changed into studying the parked VAWT in the Milan wind tunnel. In the first part of this thesis (chapter 1 to 5), a measurement system has been developed to measure the displacements on the large wind turbines based on the processing of the stereo images and analyse the resultant displacement time series to study vibrations and dynamics. In the second part of the thesis, the setup design has been proposed for the Background-oriented schlieren (BOS) experiment and a set of measurements have been conducted to quantify the tip vortex behind a HAWT by means of the BOS technique.

I am grateful to both my supervisors, Uwe Schmidt Paulsen and Jakob Mann, for the invaluable advice and discussions regarding both stereo vision and BOS parts and also the other supervisor, Mikael Sjöholm, for proofreading the thesis.

I would like to particularly thank Anders Melchior Hansen for his great guidance in SSI identification and also Morten Hartvig Hansen for his help in conducting classical modal analysis with PULSE. I also appreciate the technicians at the department for help with the realization of the experiments and specially Per Hansen and Michael Rasmussen for accompanying me during the Milano experiment, as well as my colleagues in the test and measurement (TEM) program for their valuable input.

I wish to thank my parents who have always been loving and supportive for encouraging me to do my best in my education. I would like to say something to my father who I lost a few days before my original thesis submission deadline: daddy, I never told you how much I love you and how much I thank you for all of your efforts in life for me, but I am telling you while I miss you, your hands and your eyes: thank you daddy for all you have done for me, thank you!

Finally, I would like to thank my loving husband for his endless love, patience and support during my PhD. I also appreciate his kind and helpful guidance for understanding the vibration part of my project.

Nadia Najafi

July 2015, Roskilde, Denmark.

# Contents

1.	Stereo vision technique.....	11
1.1	Motivation.....	11
1.2	Introduction to stereo vision.....	12
1.3	Introduction to the concept of stereo vision.....	15
1.3.1	Correspondence problem.....	15
1.3.2	3D reconstruction.....	17
2.	Introduction to Operational Modal Analysis.....	22
2.1	Motivation.....	22
2.2	Time Domain Identification.....	23
2.2.1	NExT-type Procedures.....	23
2.2.2	ARMA-Type Methods.....	24
2.2.3	Stochastic Subspace Identification.....	25
2.2.4	Modal parameters identification.....	32
2.3	Frequency Domain Identification.....	33
2.3.1	Frequency Domain Decomposition.....	33
3.	Turbine blade experiment in the field.....	39
3.1	Motivation.....	39
3.2	Blade Description.....	39
3.3	Classical modal experiment.....	41
3.3.1	Experiment setup.....	41
3.3.2	Results.....	43
3.4	Numerical Simulation.....	43
3.5	Operational Modal Analysis.....	44
3.5.1	Camera calibration.....	46
3.5.2	Image Processing.....	48
3.5.3	SSI-COV analysis.....	50
3.5.4	Results.....	53
3.6	Conclusions.....	56
4.	VAWT experiment in the wind tunnel.....	58
4.1	Motivation.....	58
4.2	Experiment setup.....	58
4.2.1	Data acquisition.....	62
4.3	Camera Calibration.....	62
4.4	Image Processing.....	64
4.4.1	Perspective correction.....	66
4.5	DD-SSI analysis.....	69
4.5.1	Analytical validation of the DD-SSI code.....	69
4.5.2	Numerical validation of the DD-SSI code.....	72
4.5.3	DD-SSI results.....	74
4.6	Structural modes.....	76
4.6.1	HAWC2 simulation.....	76
4.6.2	Wind tunnel experiment.....	78

4.7	Guy wire effects .....	84
4.8	Induced vortex shedding frequency.....	86
4.9	Modal Identification using FDD.....	88
4.10	Classical modal experiment on the VAWT rotor .....	90
4.11	Conclusion.....	92
5.	Uncertainty Analysis in Stereo reconstruction.....	95
5.1	Introduction .....	95
5.2	Propagation of uncertainty .....	95
5.3	Uncertainty propagation in the stereo vision reconstruction.....	97
5.3.1	Uncertainty propagation in camera calibration .....	97
5.3.2	Uncertainty Propagation in stereo reconstruction .....	98
5.4	Uncertainty analysis for the blade experiment.....	100
5.5	Uncertainty analysis for the VAWT experiment in the wind tunnel.....	104
5.6	Conclusion.....	106
6.	Background-oriented schlieren study of the turbine tip vortex.....	108
6.1	Motivation .....	108
6.2	Introduction to the Background-oriented Schlieren method.....	108
6.3	Density distribution through the tip vortices .....	111
6.4	Angular deflection and displacement due to the density gradient .....	113
6.5	Density and displacement estimation in a tip vortex .....	114
6.6	New setup.....	118
6.7	Estimation of the tip vortex parameters.....	122
6.8	Conclusion.....	133
7.	Conclusions and future work .....	135
7.1	Conclusions .....	135
7.2	Future work.....	138

## Summary

In the present thesis, two modern vision technologies are developed and used to study wind turbines:

- 1- Stereo vision to study vibrations and dynamics of the Vertical Axes Wind Turbine (VAWT) via operational modal analysis (OMA)
- 2- Background-oriented Schlieren (BOS) method to study the tip vortices that are shed from a Horizontal Axis Wind Turbine (HAWT) blades

The thesis starts with an introduction to the stereo vision and OMA and is followed by two practical implementations of the basics derived in the introduction. In the first experiment, we developed the image processing tools to extract the displacement time series from stereo images taken from a VAWT blade subjected to the random vibrations. For analysing the time series, we devised an averaged approach of the covariance-driven stochastic subspace identification (COV-SSI) method. The method enables us to involve short measurement sets in OMA. Therefore, the first four natural frequencies are identified and agreed fairly with classical modal analysis (EMA) and finite element simulation (FEM).

The second experiment is conducted on a VAWT rotor in the wind tunnel in a more controlled and designed condition, and the displacement time series are obtained using a more elaborated image processing algorithm. In OMA part, we developed the data-driven stochastic subspace identification (DD-SSI) and frequency domain decomposition (FDD) codes for studying the dynamic behaviour of the turbine. The structural modes of the VAWT obtained with OMA are validated with the simulation and EMA, and then, the differences are explained with the aerodynamic effect and boundary conditions. The other frequencies obtained by OMA are interpreted via vortex shedding phenomena and guy wire effects. In the fifth chapter, the uncertainty of the displacements obtained in the two experiments mentioned above, is evaluated using the law of error propagation and several solutions are presented to decrease the uncertainty in the stereo vision experiments.

In the last chapter of the thesis, the BOS method has been used to study the tip vortices behind a Nordtank horizontal axis wind turbine based on the density gradient in the vortex. The BOS method does not need complicated equipment such as special cameras or seeded flow, which makes it a convenient method to study large scale flows. However, the challenging part in the current case is the small refractive index change due to the small Mach number in the flow behind the HAWT. This issue has been addressed in the last chapter by designing a proper experimental setup according to the preliminary estimation of the tip vortex. The changes due to the vortex are modelled, and the tip vortex properties such as vortex size, density distribution and the maximum pressure drop in the vortex core are successfully estimated by comparison between the model and the experimental observations.

## Resumé

I nærværende afhandling udvikler vi to moderne kamerateknologier til at studere vindmøller med, dels med stereovision til at måle deformationer med og ved hjælp af Operational Modal Analysis (OMA) at studere dynamikken på en lodret-akslet vindmølle (VAWT) dels med en Background-oriented schlieren metode (BOS) for at studere tiphvirvler fra en 500 kW horisontal-akslet vindmølle under drift. Afhandlingen introducerer stereovision og OMA, og efterfølges af to praktiske implementeringer. I det første forsøg, der er udført på en VAWT vinge, har vi udviklet billedbehandlingsværktøjer til at analysere tidsserier af markører, som forskydes i tid og rum i billedplanen. Efterfølgende gør en udtænkt kovariant Sub Space Identification (COV-SSI) metode os i stand til at fortolke korte måleserier. Vi identificer de fire første egenfrekvenser og sammenligner resultaterne med klassisk modal analyse (EMA) og med finite element method (FEM) beregning. I et andet forsøg studerer vi deformationer på en stillestående, 3-bladet, 1-kW VAWT rotor med vindpåvirkning opnået i Polytecnico di Milano's vindtunnel. Vi anvender en forbedret billedbehandlingsalgoritme, dog med den begrænsning at et af bladene med den anvendte 2-kamera opstilling ikke kan ses i billederne. I OMA afsnittet har vi udviklet data driven SSI (DD-SSI) og Frequency Domain Decomposition (FDD) koder for at studere dynamikken. De modale VAWT former er identificeret med OMA og valideres med simuleringer og med klassisk modalanalyse. Resultatforskelle forklares ud fra aero -og strukturdynamiske randbetingelseeffekter, hvirvelafløsning og bardun effekter. Usikkerheder for målte deformationer evalueres i de to nævnte eksperimenter ved fejlophobningsloven, og flere løsninger præsenteres for at mindske usikkerheden. I den sidste del af afhandlingen er BOS metoden blevet brugt til at studere tiphvirvler fra en Nordtank vindmølle i drift i naturlig vind. BOS baseres på synlig detektering af hvirvelkernens luftmassefyldegradient, og metoden behøver ikke kompliceret udstyr eller seedet flow, hvilket gør det til en bekvem metode for at studere flow i større skala. Udfordringen ligger i at kunne måle den lille brydningsindeksændring som følge af det lille Mach-tal. Spørgsmålet behandles i sidste kapitel, og ved at designe eksperimentet ud fra en foreløbig vurdering af tiphvirvlens egenskab, såsom størrelsen, tæthed og det maksimale trykfald henover kernen, kan tiphvirvlen estimeres ved at tilpasse model og observationer.

## List of Symbols

$Y_{02i}$	Block Hankel matrix	
$\hat{G}_{yy}$	Power spectral density (PSD) matrix	
$\varepsilon$	Angular deflection in BOS	
$A$	State matrix	
$a$	Induction factor	
$B$	Input matrix	
$C$	Observation matrix	
$C_d$	Drag coefficient	
$C_l$	Lift coefficient	
$d$	Disparity	[m]
$D^1$	Direct term matrix	
$D$	Drag force	[N]
$E$	Expectation operator	
$f$	Focal length	[mm]
$f_i$	$i^{\text{th}}$ natural frequency	[Hz]
$G$	Output-state covariance matrix	
$I$	Pixel intensity	
$K$	Stiffness matrix	
$k$	Gladstone–Dale constant	
$L$	Lift force	[N]
$l$	Turbine tip vortex pitch	
$M$	Mass matrix	
$Ma$	Mach number	
$n$	Refractive index of fluid	
$n_c$	Number of measurement channels	
$O$	Centre of projection	
$O_i$	Projection matrix	
$p$	Pressure	[Pa]
$p_\infty$	Free stream pressure (atmospheric pressure)	[Pa]
$R$	Rotation matrix	
$r_c$	Vortex core radius	[cm]
$Re$	Reynolds number	

---

<sup>1</sup> It is used only in chapter 2.



$R_{xy}$	The cross-correlation function between $x(t)$ and $y(t)$	
$R_{yy}$	The auto correlation function of $y(t)$	
$\Sigma$	State covariance matrix	
$St$	Strouhal number	
$s_x$	Effective pixel size in the horizontal direction	[ $\mu\text{m}$ ]
$s_y$	Effective pixel size in the vertical direction	[ $\mu\text{m}$ ]
$T^1$	Translation matrix	
$T$	Wire tension force	[N]
$T_{ i}$	Block Toeplitz matrix	
$U \ u(x_{wi}^W), u(y_{wi}^W), u(z_{wi}^W)$	Uncertainty of the calibration grid points coordinates in x, y and z directions	[mm]
$u(x_{ui}^I), u(y_{ui}^I)$	Uncertainty of the grid point localization in x and y directions	[pixel]
$u(x^W), u(y^W), u(z^W)$	Uncertainty of the measured displacement by stereo vision in x, y and z directions	[mm]
$V_0$	Free stream wind speed	[m/s]
$W$	Image window size	[Pixel]
$w_k$	Process noise in time step of $k$	
$x(t)$	State vector	
$y_i$	Block of measured displacement data at time $i$	
$\alpha$	Cone skewness in x direction	
$\alpha_i$	Angle of attack	[Degree]
$\beta$	Cone skewness in y direction	
$\Gamma$	Extended observability matrix	
$\gamma$	Cone sharpness	
$\gamma^2$	Specific heat ratio of air	
$\Gamma_\infty$	Vortex circulation	[m <sup>2</sup> /s]
$\Delta$	Extended stochastic observability matrix	
$\Delta y$	Image displacement in BOS	[mm]

<sup>1</sup> It used only in section 4.7.

<sup>2</sup> It used only in section 4.4.1.

$\Delta y'$	Virtual image displacement in BOS	[mm]
$\zeta_i$	$i^{th}$ natural Damping ratio	
$\Lambda_i$	Output covariance matrix with time lag of $i$	
$\lambda$	Light wave length	[ $\mu\text{m}$ ]
$v_k$	Measurement noise in time step of $k$	
$v_\theta$	Tangential velocity in the Rankine vortex	[m/s]
$\rho$	Density	[kg/m <sup>3</sup> ]
$\rho_\infty$	Free stream air density	[kg/m <sup>3</sup> ]
$\sigma$	Standard deviation	
$\Phi_i$	$i^{th}$ mode shape	

# 1. Stereo vision technique

## 1.1 Motivation

Real world objects appear to us in 3 dimensions, whereas information captured are placed on paper, film, eye retina or similar 2D planes. However, there exist methods for reconstructing a 3D scene from 2D images. From experience, objects close to the observing eyes are larger on paper than objects in the background appearing smaller, with additional effects on whether to focus on the foreground or background as the main theme. Visual space, or the third dimension, has been developed by evolution and needs good guess and cognitive skills of a simultaneous look from two eyes. Charles Wheatstone was a modern founder who understood this basis mechanism at the end of the last century<sup>1</sup> in his contribution to understanding the physiology of vision: ‘When an object is viewed at so great a distance that the optic axes of both eyes are sensibly parallel when directed towards it, the perspective projections of it, seen by each eye separately, are similar, and the appearance to the two eyes is precisely the same as when the object is seen by only one eye. There is, in such case, no difference between the visual appearance of an object in relief and its perspective projection on a plane surface; and hence, pictorial representations of distant objects, when those circumstances that would prevent or disturb the illusion are carefully excluded, may render perfect resemblances of the objects that they are intended to represent such that they may be mistaken for them; the Diorama is an instance of this. But this similarity no longer exists when the object is placed so near the eyes that the optic axes must converge to view it; under these conditions a different perspective projection of it is seen by each eye, and these perspectives become more dissimilar as the convergence of the optic axes becomes greater.’ To translate in effect these principles into a contemporary technical stereo vision application, triangulation and effective use of non-costly blocks to hold memory images (charged coupled device; CCD) needs the relentless computing power from computers.

Since stereo vision is a technique based on the processing of images, it has technical potentials for the wind turbine industry over existing techniques; the technology addresses particular topics for the wind power industry within vibration testing and measurement techniques, vibration data analysis techniques, modelling and simulation of vibration testing results, structural monitoring, experimental characterization of

---

<sup>1</sup> Contributions to the Physiology of Vision.—Part the First. On some remarkable, and hitherto unobserved, Phenomena of Binocular Vision. By CHARLES WHEATSTONE, F.R.S., Professor of Experimental Philosophy in King's College, London., 1838

dynamic actions, system identification and model updating, vibration based structural assessment and damage detection techniques, vibration isolation and mitigation, effects of shock and vibration on humans and structures and methodologies and standards. Hence, many facets, the stereo vision technique in this thesis has to be narrowed and focused on specific issues.

## 1.2 Introduction to stereo vision

Stereo vision is the technique of 3D reconstruction of a target from two or more images. It has been developed with powerful computer vision tools on non-costly CCDs. Stereo vision stems from stereoscopy based on binocular vision perception known from individuals and animals in nature. The capability of humans to capture 3D dimensional fixed and moving objects, e.g. with optical sensors (eyes) and image reconstruction procedures (brain) to reconstruct the images into 3D information is made visible in Figure 1.1. Here, the perception of the third dimension (stereopsis) [1] is made tangible via stereo vision by the projection of the object into the left and right image, and then, by comparing the horizontal positions of these images using the difference between the two images (disparity) as a measure for the depth. As the computer is good at handling even large quantities of information, the task for the engineer is to translate the information back to an identical representation of the object by performing algorithms developed into a vision tool. A computer vision system can comprise multiple cameras ensuring redundant images over an angular sphere surrounding the object.

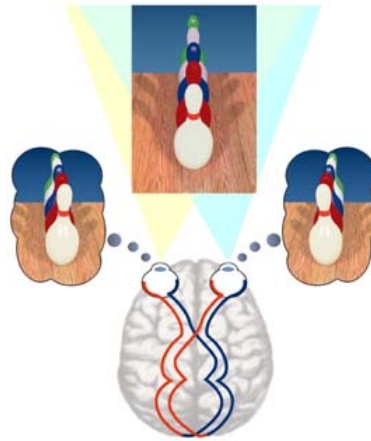


**Figure 1.1:** The brain merges the views of each eye to form a 3D view

The stereo vision method has been widely used for different technical applications such as surveillance, 3D scanning/cognition/recognition of objects or patterns in civilian and military applications, technology for measuring length (see Figure 1.2), structural dynamics & mechanics, inspection and robotics.

Robotics as an example uses stereo vision to provide information of the real target and process these into actions, such as in positioning different parts of the robots like robot

arms [2], controlling oscillations [3] and robot navigation [4]. Depth information is one of the most important information that stereo vision provides [5]. With good performance stereo vision can be applied to far distance evaluation and obstacle detection [6]. Stereo vision could also accurately measures 3D displacement or strain fields that are applicable in defining 3D strain fields in sheet metal forming [7] and 3D elastic surface deformations [8].

Measuring 3D displacement of the structures is an important issue for monitoring their dynamic behaviour. Strain gauges and accelerometers have been traditionally employed for displacement measurements [9]. These measurements usually need a lot of wiring to other devices like data logger and power supply, which is costly and time consuming [10]. Strain gauges have to be installed between the measurement points and a fixed point is required as a reference, which is difficult for big structures. Accelerometer signals also need two levels of integration to get displacement information; this introduces errors due to initial conditions and other computation issues [11]. In measuring 3D displacement by stereo vision, very simple sensing markers such as reflecting or non-reflecting paper are used as 3D sensors. The installation of many sensory markers needs no long preparation time. By mounting two identical equipped cameras that are looking onto the markers applied on the structure with a mutual, horizontal distance in between, the displacements can be found using a proper image processing algorithm (triangulation).

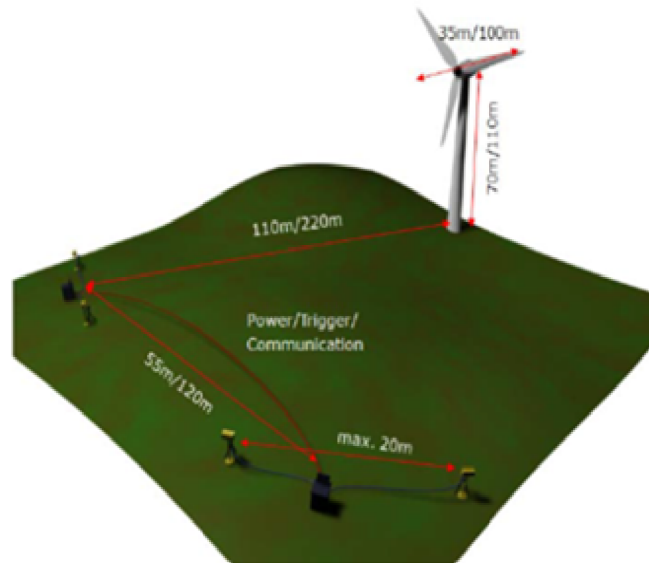


**Figure 1.2:** Camera setup for stereo vision in the case of large objects [22]

Stereo vision displacement measurements can be used in both classical and operational modal analysis. In classical modal analysis, stereo vision results have shown good agreement with the accelerometer results in addition to having more convenience in implementation and higher capability for presenting very small modal frequencies [12]. In OMA the input will not be measured and stereo vision will be the proper method to

simultaneously measure the output displacement of many points of the structure as the output [13, 14].

Stereo vision has been used in strain and full displacement field analyses with either digital images correlation (DIC), which gives a continuous displacement distribution, [15, 16] or measuring discrete points on the surface or structure (point tracking approach). However, stereo vision is new in measuring vibration; it shows good correlation with conventional methods like accelerations in this field [17]. For operating structures, the use of conventional methods introduces several limitations and drawbacks; they might load the structure with a weight accounted by the sensors and can measure in only a few number of points [18]. Even using roving methods with accelerometers is very time consuming. In addition, in rotating structures like wind turbines, the measured signal from conventional methods like accelerometers will be quite noisy and the centrifugal acceleration should be removed from the final response. The robustness and simplicity of the stereo vision make it a proper approach for outdoor and large scale experiments in difficult conditions. Regarding all these issues, stereo vision shows good potentials for studying the structural and modal properties of wind turbines.

Structural response and modal properties of wind turbines have been studied by stereo vision in recent years [19-22]. Stereo vision with both DIC and point tracking techniques shows very high correlation with conventional methods and the structural modes are successfully captured in operation beside all the convince of the method with an enormous number of sensors, low noise and high accuracy.



**Figure 1.3:** Point tracking markers on wind turbine rotor for investigating the effects of seismic activity. UCSD, California [thanks to Tim Schmidt Trillion, USA]

## 1.3 Introduction to the concept of stereo vision

In stereo vision, a 3D model of a scene is reconstructed by taking two or more pictures from different viewpoints [23]. The model of a stereo vision system is shown in Figure 1.4, comprising two identical cameras separated with distance  $b$ . One of the important parameters in 3D reconstruction is *disparity* defined as the distance between the positions of corresponding points or features (e.g. an interesting part of an image, such as a corner, blob, edge or line) in the image planes of the cameras [24].

The plane passing through the scene point and the camera centres is called *epipolar plane*, and the intersections of this plane with the image planes are called *epipolar lines* [24]. They are shown in Figure 1.4.

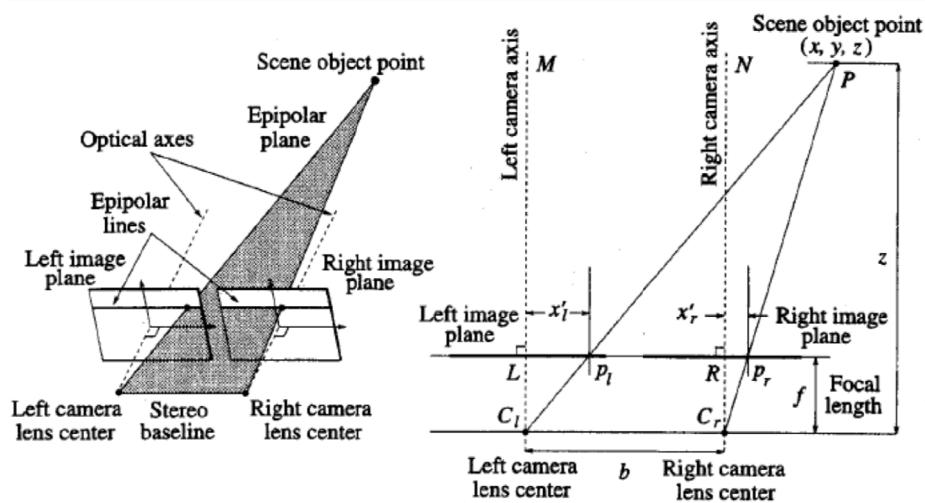


Figure 1.4: A simple stereo vision system [24]

In stereo vision, two main challenges have to be considered to reconstruct a 3D object from the information of the 2D images: The first challenge is determining which item in the left image corresponds to which item in the right image; this is referred to as the correspondence problem [25]. The second challenge is the 3D reconstruction of the scene from the 2D images. A disparity map, which defines the disparity distribution all over the image, is key for solving this problem by looking into the differences of left and right images on the pixel level.

### 1.3.1 Correspondence problem

Correspondence or stereo matching is described as follows: looking for the corresponding feature or point in the right image for each feature or point in the left image. For matching those elements, similarity between them should be measured [24]. The correspondence problem is solved easily using the following two assumptions: most of the points can be seen in both viewpoints and the corresponding image areas are



similar. These requirements will be mostly met when the distance between the cameras and the scene is much larger than the baseline.

The similarity between image elements is measured with two different approaches, correlation- and feature-based methods, which imply different conditions [25].

## Correlation based methods

In correlation based methods, images are divided into windows or search boxes that are the elements to be matched. In fact the similarity criterion is the correlation measurements between two windows of image pairs [25]. The correlation function between the left ( $I_l$ ) and right ( $I_r$ ) image windows will be maximized instead of the disparity values between two windows ( $d = [d_1, d_2]$ ).

If the window width is  $2W + 1$  in pixels and  $\psi(u, v)$  is a function of two pixel values,  $u$  and  $v$ , the correlation function is as follows [25]:

$$c(d) = \sum_{k=-W}^W \sum_{l=-W}^W \psi(I_l(i+k, j+l), I_r(i+k-d_1, j+l-d_2)) \quad (1.1)$$

There are two more common descriptions of the function  $\psi(u, v)$ . The first description is the cross correlation between the windows of the left and right images [25]:

$$\psi(u, v) = uv \quad (1.2)$$

The second one is called sum of squared differences (SSD):

$$\psi(u, v) = -(u - v)^2 \quad (1.3)$$

Both equations (1.2) and (1.3) give the same correspondence if the energy of the right image in each window is constant all over the search region (energy of an image is the sum of the intensity values of the squares of the image); however, in real application, this rarely happens [25]. When cross correlation, equation (1.2), is biased, the intensity values are very small or very large; hence, SSD is preferable in most cases.

## Feature-based methods

Feature-based methods search for a sparse set of features in the images and use numerical and analytical properties of the features to solve the correspondence problem [25]. Epipolar constraint is defined to facilitate easy finding of corresponding features in image pairs. Epipolar constraint indicates that the corresponding points must lie along corresponding epipolar lines [26]. This constraint confines the correspondence problem into a 1D search of the match along the epipolar line.

The properties that need to be matched are different for different features and change with the overall condition of the images, such as illumination or average contrast of the

image. As an example, length, orientation and average contrast along the edges describe the line features. Hence, these features should be matched for corresponding lines in the image pairs [25].

In real applications, choosing the method to solve the correspondence problem depends on the application and hardware and software facilities; however, there are a few general remarks about the fields that each of the methods are more qualified for [25]. The two next paragraphs will state some of these remarks for clarification.

Correlation-based methods are easier to implement and because of making windows all over the images provide a dense disparity map. However, they are sensitive to illumination changes and do not work well for images taken from very different viewpoints. In addition, as they give only one value for disparity for each window, the resolution reduces to the window size and interpolation to increase the precision from pixels to sub pixels is also expensive.

When there is prior knowledge about the scene and the image features, feature-based methods are implemented that are faster and provide sparse disparity maps. In fact, when the motion of a few particular features or elements is studied through the images, feature-based methods are the faster and more accurate choice. Furthermore, these methods are not sensitive to illumination changes and different viewpoints.

### **1.3.2 3D reconstruction**

After finding the corresponding points in the stereo images, the 3D coordinates of the scene can be constructed. The 3D reconstruction method depends on the knowledge of the intrinsic and extrinsic parameters of the cameras. If they are already known by the camera calibration, then the 3D reconstruction problem will be solved via triangulation; otherwise, there are methods to estimate those parameters up to a few unknowns in parallel with the reconstruction process. However, the most common way is calibrating the cameras before doing the stereo vision 3D reconstruction. Therefore, the stereo vision steps to go from the pixel coordinates to 3D world coordinates can be summarized in the following figure:

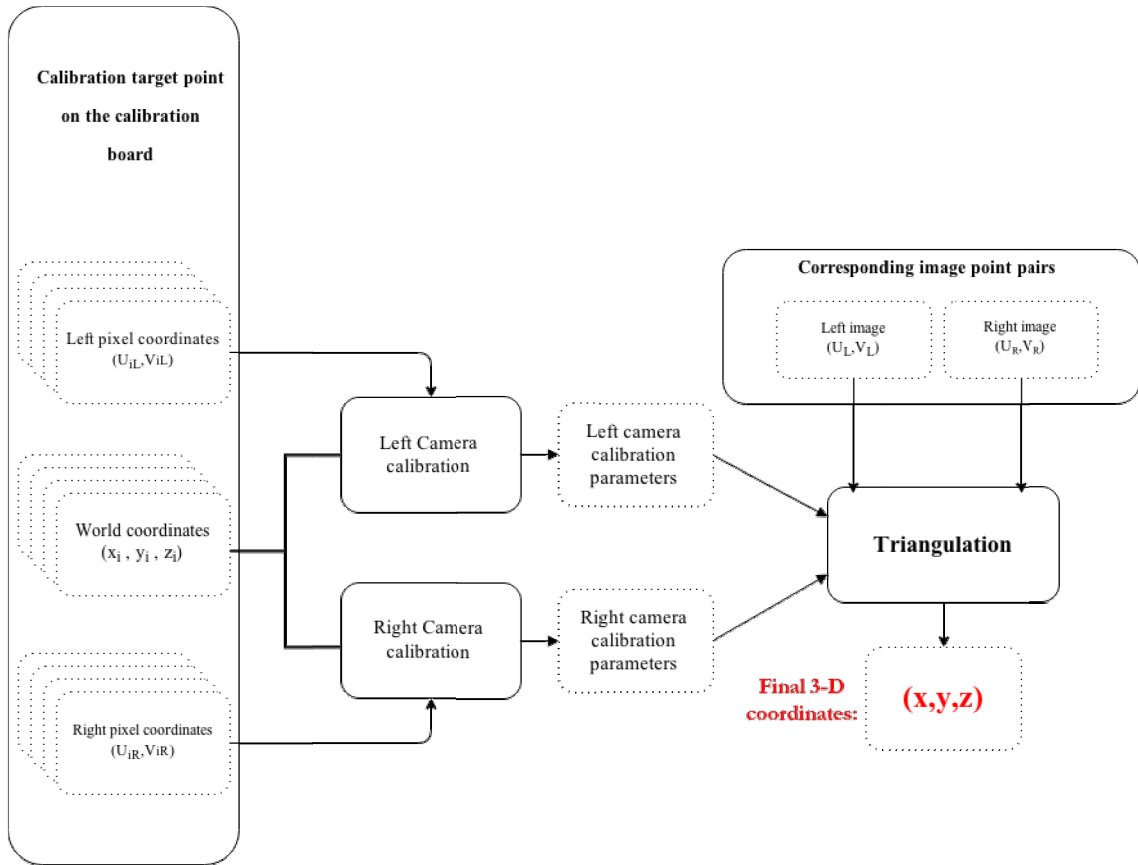


Figure 1.5: Stereovision process in time instance  $T = t_0$

## Triangulation

Let the projection of the point  $P$  be  $p_l$  in the left image and  $p_r$  in the right image. The ray  $l$ , passing from  $O_l$  (left camera centre of projection) through  $p_l$  will intersect ray  $r$ , passing from  $O_r$  through  $p_r$ , in point  $P$ . However, while the camera parameters are estimated with an uncertainty, the ray will not actually intersect in space. Therefore, the intersection will be estimated as the midpoint of their minimum distance.

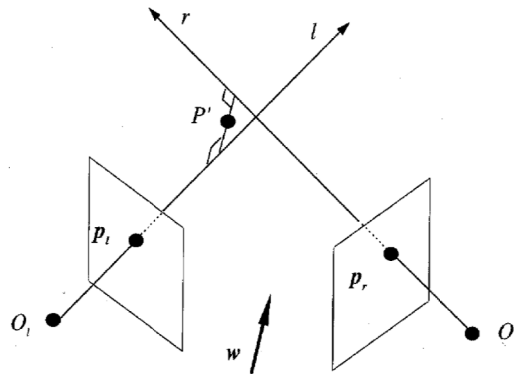


Figure 1.6 : Triangulation with nonintersecting rays [16]

If the point  $O_l$  is the reference point, ray  $l = ap_l$  passing through  $O_l(a=0)$  and  $p_l(a=1)$  and ray  $r$  will be  $T+bR^T p_r$  passing through  $O_r(b=0)$  and  $p_r(b=1)$ . Let  $w = p_l \times R^T p_l$  be the vector orthogonal to both  $l$  and  $r$ , then  $\omega = ap_l + cw$  is the line through  $ap_l$  and parallel to  $w$ .

The midpoint of the segment  $s$ , between the intersections of  $\omega$  with  $l$  and  $r$ , will be the triangulated point  $P'$ .

If  $T_l, R_l$  and  $T_r, R_r$  are extrinsic parameters of two cameras in the world coordinate system, the extrinsic parameters of the stereo system are as follows [16]:

$$\begin{aligned} R &= R_r R_l^T \\ T &= T_l - R^T T_r \end{aligned} \tag{1.4}$$

## References

- [1] Westheimer, G. (2010): Three-dimensional displays and stereo vision, pp. 2257-2281, Proceeding of the Royal Society B.
- [2] Chiang, M. H., Lin, H. T., and Hou, C. L. (2011): Development of a Stereo Vision Measurement System for a 3D Three-Axial Pneumatic Parallel Mechanism Robot Arm, pp. 2257-2281, Journal of Sensors 11.
- [3] Hitaka, G., Murakami, T., and Ohnishi, K. (2001): An Approach to Vibration Control by Stereo Vision System in Mobile Manipulator, IEEWASME International Conference on Advanced intelligent Mechatronics Proceedings 8-12 July 2001, Como, Italy.
- [4] Ghazouani, H., Tagina, M., and Zapata, R. (2010): Robot Navigation Map Building Using Stereo Vision Based 3D Occupancy Grid, pp. 63-72, Journal of Artificial Intelligence: Theory and Application 1.
- [5] Shimon, Y. N. (1999): Handbook of Industrial Robotics, pp. 269-294, John Wiley & Sons.
- [6] Nedeveschi, S., et al. (2004): High Accuracy Stereo Vision System for Far Distance Obstacle Detection, IEEE Intelligent Vehicles Symposium University of Parma, Parma, Italy, June 14-17.
- [7] Garcia, D., Orteu, J. J., and Penazzi, L. (2002): A combined temporal tracking and stereo-correlation technique for accurate measurement of 3D displacements: application to sheet metal forming, P 736-742, Journal of Materials Processing Technology 125-126.
- [8] Chan, Y. H., et al. (2009): Modeling of Elastic Deformation using Stereo Vision and Smoothed Particle Hydrodynamics, 24th International Conference Image and Vision Computing New Zealand.
- [9] Hoffmann, K. (1989): An introduction to measurements using strain gages, Hottinger Baldwin Messtechnik GmbH, Darmstadt.
- [10] Fukuda, Y., et al. (2013): Vision-Based Displacement Sensor for Monitoring Dynamic Response Using Robust Object Search Algorithm, pp. 4725-4732, IEEE Sensors Journal 13.
- [11] Park, K., T., Kim, S. H., Park, H. S., Lee, K. W. (2005): The determination of bridge displacement using measured acceleration, pp. 371-378, Journal of Engineering Structures 27.
- [12] Peeters, B., et al. (2004): Experimental modal analysis using camera displacement measurements: a feasibility study, pp. 298-309 Sixth International Conference on Vibration Measurements by Laser Techniques: Advances and Applications, Proceedings of SPIE Vol. 5503 (SPIE, Bellingham, WA, 2004).
- [13] Kohut, P., Kurowski, P. (2009): Application of Modal Analysis Supported by 3D Vision-Based Measurements, pp. 855-870, Journal of Theoretical and Applied Mechanics 47.
- [14] Ozbek, M., Rixen, D. J. (2013): Operational modal analysis of a 2.5 MW wind turbine using optical measurement techniques and strain gauges, pp. 367-381, Journal of Wind Energy 16.
- [15] Helm, J. D., McNeil, S. R., Sutton, M. A. (1996): Improved three-dimensional image correlation for surface displacement measurement, pp. 1911-1920, Journal of Optical Engineering 35.
- [16] McNeil, S. R., Peters, W. H., Sutton, M. A. (1987): Estimation of stress intensity factor by digital image correlation, pp. 101-112, Journal of Engineering Fracture Mechanics 28.
- [17] Warren, C., et al. (2010): Comparison of Image Based, Laser, and Accelerometer Measurements, Proceedings of the IMAC-XXVIII, February 1-4, 2010, Jacksonville, Florida USA.
- [18] Helfrick, M. N., et al. (2011): 3D digital image correlation methods for full-field vibration measurement, pp. 917-927, Journal of Mechanical Systems and Signal Processing 25.
- [19] Warren, C., Niezrecki, C., Avitabile, P. (2010): Optical Non-contacting Vibration Measurement of Rotating Turbine Blades II, Proceedings of the IMAC-XXVIII, February 1-4, 2010, Jacksonville, Florida USA.
- [20] Prowell, I., et al. (2011): Measuring Global Response Of A Wind Turbine To Simulated Earthquake Shaking Assisted By Point Tracking Videogrammetry, 52nd AIAA/ASME/ASCE/AHS/ASC Structures, Structural Dynamics and Materials Conference, 19<sup>th</sup> 4-7 April 2011, Denver, Colorado.

- [21] Prowell, I., et al. (2012): Shake Table Testing of a Utility-Scale Wind Turbine, pp. 900-909, Journal of Engineering Mechanics 138.
- [22] Paulsen, U. S., Erne, O., Klein, M. (2012): Modal Analysis on a 500 kW Wind Turbine with Stereo Camera Technique, IOMAC'09 – 3rd International Operational Modal Analysis Conference.
- [23] Szeliski, R. (2010): Computer Vision: Algorithms and Applications, Springer, London.
- [24] Jain, R., Kasturi, R., Schunck, B. G. (1995): Machine Vision, McGraw-Hill.
- [24] Trucco, E., Verri. A. (1998): Introductory Techniques for 3-D Computer Vision, Prentice Hall, New Jersey, United States.
- [26] Hartley, R., Zisserman, A. (2003): Multiple View Geometry in Computer Vision, Cambridge University Press, Cambridge, United Kingdom.

## 2. Introduction to Operational Modal Analysis

### 2.1 Motivation

Modal analysis has been used for studying the structural and modal properties of structures for many years. In classical (experimental) modal analysis (EMA), the structure is excited by an external force, and both output response and input excitation are measured. The theoretical basis of this measurement technique is establishing a mathematical relationship between the input and output of a linear time invariant (LTI) system called the frequency response function (FRF), as a function of excitation frequency [1]. The FRF matrix represents the modal properties of the structure, such as natural frequencies, damping ratios and the mode shapes. EMA has some limitations [2]:

- In EMA, input excitation of the structure needs to be measured, which is difficult to achieve on large structures like bridges and wind turbines that are always under ambient and uncontrollable loadings from traffic, wind, etc.
- Modal properties depend on operating conditions that often cannot be measured, such as aerodynamic forces on different parts of an operating wind turbine. For that reason, EMA is mostly conducted in the laboratory environment, controlling all the conditions and measuring both input and output. For this reason, EMA is difficult or practically impossible to conduct on industrial applications under operation.

Operational modal analysis estimates the modal properties of an LTI system, which is excited by an unknown, uncorrelated and distributed input, only from the output response [3]. Since early 1990's OMA has become widely used in civil engineering applications for modal identification of buildings, towers, bridges, etc. The development also stimulated areas in aerospace and mechanical engineering because of the advantages such as [2]

- Being cheaper and faster than EMA
- No need to have much knowledge about the input
- No boundary condition simulation
- Modelling of the system under real loading
- Ability to perform vibration-based health monitoring and damage detection

OMA is used in both time and frequency domains. In both domains, the input is assumed to be approximately white noise [7]. OMA is based on the following principles:

- 1- Correlation function is interpreted as free decays in the time domain.



- 2- Spectral density is interpreted as the corresponding functions in the frequency domain.

In this chapter, operational modal identification methods in time and frequency domain are explained and the procedure and difficulties associated with each of them are described.

## 2.2 Time Domain Identification

### 2.2.1 NExT-type Procedures

In the 1990's some time domain methods in combination with correlation functions, called natural excitation techniques (NExT), were developed [4,5,6]. The cross-correlation function,  $R_{xy}$ , of the two random vector responses  $x(t)$  and  $y(t)$  is the expected value of their products at the time separation of  $k$  [4]. In other words,  $R_{xy}$  is the long term average value of the products of  $x(t)$  and  $y(t)$ , in time:

$$R_{xy}(k) = E[x(t+k) \cdot y(t)] \quad (2.1)$$

where  $E$  is the expectation operator. The auto correlation function of  $y(t)$  is

$$R_{yy}(k) = E[y(t+k) \cdot y(t)] \quad (2.2)$$

It is shown in [4] that the correlation function is the summation of decaying sinusoids. NExT uses a correlation function of the response as the sum of decaying sinusoids that contains natural frequencies, damping ratios and mode shape coefficients.

Main NExT-type methods are:

- Least squares complex exponential (LSCE)
- Ibrahim time domain (ITD)
- Eigensystem realization algorithm (ERA)

In the LSCE method, a curve fitting problem is solved for finding modal parameters from correlation functions [3]. The correlation function in terms of decaying sinusoids in discrete time will be written as:

$$R_{ij}(k\Delta t) = \sum_{r=1}^{N_m} (C_{ij,r} e^{\lambda_r k\Delta t} + C_{ij,r}^* e^{\lambda_r^* k\Delta t}) \quad (2.3)$$

As the poles are complex conjugate pairs, the correlation function is written as:

$$R_{ij}(k\Delta t) = \sum_{r=1}^n \bar{C}_{ij,r} e^{\bar{\lambda}_r k\Delta t} \quad (2.4)$$

where  $C_{ij,r}$  is the constant associated to the  $r$ -th pole  $\lambda_r$  and  $n = 2N_m$ . As the poles are conjugate pairs, a polynomial with roots of  $z_r = e^{\lambda_r \Delta t}$  ( $r=1, \dots, n$ ) (known as Prony's equation) can be established:

$$\beta_0 z_r^0 + \beta_1 z_r^1 + \dots + \beta_{n-1} z_r^{n-1} + z_r^n = 0 \quad (2.5)$$

Having the correlation function between all the data channels for all the time separations gives us a set of equations that can be solved for the polynomial coefficients

$\beta_k$  in a least square sense and  $\left\{ \begin{array}{c} \beta_0 \\ \beta_1 \\ \vdots \\ \beta_{n-1} \end{array} \right\}$  is related to modal parameters.

ITD is another NExT method for extracting modal parameters. In this method, a correlation function is formulated as a linear summation of complex exponentials. By arranging the measured correlation functions in a Block Hankel matrix, the modal identification will be conducted through a set of decompositions. A Hankel matrix is a square matrix with equal anti-diagonal elements. The elements of a Hankel matrix are related by the following equation:

$$A_{i,j} = A_{i-1,j+1} \quad (2.6)$$

For more information about the ITD method, refer to [3] and [7]. Moreover, in ERA, modal parameters are identified by eigenvalue decomposition of Hankel matrices of the correlation function [8,9,10].

## 2.2.2 ARMA-Type Methods

This method fits an auto regressive (AR) moving average (MA) model to the measured time series:

$$y(t) + A_1 y(t-1) + A_2 y(t-2) + \dots + A_n y(t-n) = B_0 u(t) + B_1 u(t-1) + B_2 u(t-2) + \dots + B_m u(t-m) \quad (2.7)$$

where  $y(t)$  is the measurement output at time  $t$  and  $u(t)$  is the input.  $n$  is the AR and  $m$  is the MA order. For OMA with no measured input,  $u(t)$  will be modelled as white Gaussian noise. In ARMA, equation (2.7) is written for each data channel and the  $\{A_1, A_2, \dots, A_n\}$  coefficients make up the AR matrix. Regarding the discrete state space equations (equation (2.13)), the AR matrix is the system matrix and modal parameters

can be extracted by its eigenvalue decomposition. More detailed information can be found at [7,11].

For finding AR and MA matrices, a nonlinear minimization problem needs to be solved. This can require considerable computation effort, especially with a large number of data channels convergence problems may be encountered [12,13]. By eliminating the MA part in equation (2.7), modal parameters can be found by solving a least square problem in an AR model [14]. To get the right modal values in the AR model, the model order should approach infinity. This generates a number of spurious poles that need to be separated from real poles via a stability diagram, which is described in the ‘Stability Diagram’ section.

### 2.2.3 Stochastic Subspace Identification

In the 1990’s, subspace identification methods were developed in engineering for complex dynamic identification [15]. SSI is robust and computationally less demanding compared with other methods [13]; it also has easy parameterization and fast and noniterative convergence [17]. In these methods, unmeasured forces and ambient excitations are modelled as stochastic values with unknown parameters and known behaviour, such as white noise with known zero mean value and unknown covariance. Before going to the model details, the stochastic space state system is explained in discrete time domain.

#### Stochastic space state system in discrete time

The motion of a discrete system with multi degrees of freedom and several masses, springs and dampers will be described by following equation:

$$M\ddot{U}(t) + C_2\dot{U}(t) + KU(t) = f(t) \quad (2.8)$$

where  $M, K$  and  $C_2$  are the mass, stiffness and damping matrices, respectively;  $f(t)$  and  $U(t)$  are the excitation force and displacement vector in time  $t$ , respectively<sup>1</sup>. By defining the state vector, equation (2.8) goes to state space:

$$\begin{aligned} \dot{x}(t) &= A_c x(t) + B_c f(t) \\ x(t) &= \begin{pmatrix} U(t) \\ \dot{U}(t) \end{pmatrix}, A_c = \begin{pmatrix} 0 & I \\ -M^{-1}K & -M^{-1}C_2 \end{pmatrix}, B_c = \begin{pmatrix} 0 \\ M^{-1} \end{pmatrix} \end{aligned} \quad (2.9)$$

---

<sup>1</sup> One dot denotes the first time derivative and two dots denotes the second time derivative

where  $A_c$  is the state matrix,  $B_c$  is the input matrix and  $x(t)$  is state vector. Equation (2.9) is called the state equation.

By measuring the acceleration, velocity or displacement, the observation will be a linear combination of them:

$$y(t) = C_a \ddot{U}(t) + C_v \dot{U}(t) + C_d U(t) \quad (2.10)$$

$C_a$ ,  $C_v$  and  $C_d$  are the output matrices that form the following definitions:

$$C = \begin{bmatrix} C_d - C_a M^{-1} K & C_v - C_a M^{-1} C_2 \end{bmatrix}, \quad D = C_a M^{-1} \quad (2.11)$$

Using equation (2.10) and (2.11), the observation equation is:

$$y(t) = Cx(t) + Df(t) \quad (2.12)$$

State and observation equations are in continuous time but real data is measured in discrete time instances  $k\Delta t$ ,  $k \in \mathbb{N}$ . In discrete time, the state-space model will be:

$$\begin{aligned} x_{k+1} &= Ax_k + Bf_k \\ y_k &= Cx_k + Df_k \end{aligned} \quad (2.13)$$

where  $x_k = x(k\Delta t)$  is the discrete time state vector,  $A = \exp(A_c \Delta t)$  is the discrete state matrix and  $B = (A - I)A_c^{-1}B_c$  is the discrete input matrix. By adding stochastic components (noise), the discrete state-space model will be [14]:

$$\begin{aligned} x_{k+1} &= Ax_k + Bf_k + w_k \\ y_k &= Cx_k + Df_k + v_k \end{aligned} \quad (2.14)$$

where  $w_k$  is the process noise due to the inaccuracies of linear and time invariant state space assumptions in the modelling and  $v_k$  is the measurement noise caused by measurement devices, measurement methods, experiment conditions like assumption of distributed and uncorrelated inputs, etc.  $w_k$  and  $v_k$  are immeasurable but assumed to be zero mean, white noise and with covariance matrices of [14]:

$$E \left[ \begin{pmatrix} w_p \\ v_p \end{pmatrix} \begin{pmatrix} w_p^T & v_p^T \end{pmatrix} \right] = \begin{pmatrix} Q & S \\ S^T & R \end{pmatrix} \delta_{pq} \quad (2.15)$$

where  $E$  is the expected operator and  $\delta_{pq}$  is the Kronecker delta.

## Properties of stochastic state space models

In OMA, the input  $f_k$  cannot be measured and it is removed from equation (2.14). Then, the input is modelled with the noise terms  $w_k$  and  $v_k$  with the same assumptions as in the stochastic state space model [14]:

$$\begin{aligned} x_{k+1} &= Ax_k + w_k \\ y_k &= Cx_k + v_k \end{aligned} \quad (2.16)$$

The stochastic process is assumed to be a stationary and zero mean process with the constant state covariance matrix of  $\Sigma$  (independent of time,  $w_k$  and  $v_k$ ):

$$\begin{aligned} E[x_k] &= 0 \\ E[x_k (x_k)^T] &= \Sigma \\ E[x_k w_k^T] &= 0 \\ E[x_k v_k^T] &= 0 \end{aligned} \quad (2.17)$$

The output and output-state covariance matrices are defined as follows:

$$\begin{aligned} \Lambda_i &\equiv E[y_{k+i} y_k^T] \\ G &\equiv E[x_{k+1} y_k^T] \end{aligned} \quad (2.18)$$

where  $i$  is the time lag. From the mentioned properties and definitions the following relations are obtained for a stationary stochastic process:

$$\begin{aligned} \Sigma &= A\Sigma A^T + Q \\ \Lambda_0 &= C\Sigma C^T + R \\ G &= A\Sigma C^T + S \end{aligned} \quad (2.19)$$

Then, the output covariance is

$$\Lambda_i = CA^{i-1}G \quad (2.20)$$

Equation (2.20) is one of the important properties in stochastic identification, which implies that the output covariance matrix can be decomposed to state space matrices.

## Kalman filter

One of the most important parts in stochastic subspace identification (SSI) is the optimal prediction of the future measurement based on the past measurement. The optimal predictor can estimate a model for a stochastic system that reveals the space state matrices and other system properties.

A Kalman filter is trying to predict the state vector  $x_{k+1}$  using the measurements up to time  $k$ , and the system matrices are determined by solving a regression problem. The non-steady state Kalman estimates,  $\hat{x}_{k+1}$ , are defined by the following recursive equations:

$$\begin{aligned}\hat{x}_{k+1} &= A\hat{x}_k + K_k e_k \\ e_k &= y_k - C\hat{x}_k \\ K_k &= (G - AP_k C^T)(\Lambda_0 - CP_k C^T)^{-1} \\ P_{k+1} &= AP_k A^T + (G - AP_k C^T)(\Lambda_0 - CP_k C^T)^{-1}(G - AP_k C^T)^T\end{aligned}\quad (2.21)$$

The matrix  $K_k$  is called Kalman gain and  $e_k$  is called innovation, which is the zero mean Gaussian white noise. The Kalman state estimates form the Kalman filter state sequence, which will be used in the stochastic subspace algorithm:

$$\hat{X}_i \equiv \begin{pmatrix} \hat{x}_i & \hat{x}_{i+1} & \cdots & \hat{x}_{i+j-1} \end{pmatrix} \quad (2.22)$$

## Stochastic subspace algorithm

In SSI the measurement data are gathered in a block Hankel matrix, which is divided into past and future parts:

$$Y_{0|2i} = \begin{pmatrix} y_1 & y_2 & \cdots & y_j \\ \cdots & \cdots & \cdots & \cdots \\ y_{i-1} & y_i & \cdots & y_{i+j-2} \\ y_i & y_{i+1} & \cdots & y_{i+j-1} \\ y_{i+1} & y_{i+2} & \cdots & y_{i+j} \\ y_{i+2} & y_{i+3} & \cdots & y_{i+j+1} \\ \cdots & \cdots & \cdots & \cdots \\ y_{2i} & y_{2i-1} & \cdots & y_{2i+j-1} \end{pmatrix} = \begin{pmatrix} Y_{0|i} \\ Y_{i+1|2i} \end{pmatrix} = \begin{pmatrix} Y_p \\ Y_f \end{pmatrix} = \frac{\text{"past"}}{\text{"future"}} \quad (2.23)$$

where  $j = N - 2i + 1$  is the number of block columns,  $2i$  is the number of block rows that indicate the total data shift and  $i$  is called model order.  $y_i$ ,  $i = 1, 2, \dots, N$ , is called the block of data; it contains the measurements taken from all the channels in a particular time step ( $N$  is the number of time steps). Each block is a column vector with  $n_c$  element for  $n_c$  measurement channels. Therefore, the dimension of the block Hankel matrix is  $2n_c i \times j$ . Another block Hankel matrix division that will be used in subspace identification is:

$$Y_{0|2i} = \begin{pmatrix} Y_{0|i+1} \\ Y_{i+2|2i} \end{pmatrix} = \begin{pmatrix} Y_p^+ \\ Y_f^- \end{pmatrix} = \begin{matrix} \text{"past"} \\ \text{"future"} \end{matrix} \quad (2.24)$$

The extended stochastic observability matrix is an important matrix that comes into play in the identification process:

$$\Gamma_i \equiv \begin{pmatrix} C \\ CA \\ CA^2 \\ \vdots \\ CA^{i-1} \end{pmatrix} \quad (2.25)$$

The matrix pair of  $\{A, C\}$  is assumed to be observable, which means that all the dynamic modes are observed in the output [17].

If the extended stochastic controllability matrix is defined as:

$$\Delta_i \equiv (A^{i-1}G \quad A^{i-2}G \quad \dots \quad AG \quad G) \quad (2.26)$$

equation (2.20) converts to:

$$\Lambda \equiv \Gamma_i \Delta_i \quad (2.27)$$

## Data-driven SSI

Data-driven SSI (SSI-Data) is based on the decomposition of the projection matrix. The projection matrix is another important matrix that is described as the projection of the future outputs on the past outputs [15]:



$$\begin{aligned}
O_i &\equiv Y_f / Y_p \\
O_i &\equiv Y_f^- / Y_p^+
\end{aligned} \tag{2.28}$$

These projections can be calculated using LQ decomposition of the block Hankel matrix. In the first step, the block Hankel matrix should be partitioned [15]:

$$\begin{matrix}
& & n_c i & n_c & n_c(i-1) & j \\
n_c i & \begin{pmatrix} Y_{0|i-1} \\ Y_{i|i} \\ Y_{i+1|2i} \end{pmatrix} & = & \begin{pmatrix} L_{11} & 0 & 0 \\ L_{21} & L_{22} & 0 \\ L_{31} & L_{23} & L_{33} \end{pmatrix} & \begin{pmatrix} Q_1^T \\ Q_2^T \\ Q_3^T \end{pmatrix}
\end{matrix} \tag{2.29}$$

The projection matrices are obtained using the following equations:

$$\begin{aligned}
O_i &= \begin{pmatrix} L_{21} \\ L_{31} \end{pmatrix} Q_1^T \\
O_{i-1} &= (L_{31} \quad L_{32}) \begin{pmatrix} Q_1^T \\ Q_2^T \end{pmatrix}
\end{aligned} \tag{2.30}$$

It can be proven that the projection matrix will be decomposed to the observability matrix and Kalman state matrix [15]:

$$\begin{aligned}
O_i &= \Gamma_i \hat{X}_i \\
O_{i-1} &= \Gamma_{i-1} \hat{X}_{i+1}
\end{aligned} \tag{2.31}$$

By singular value decomposition (SVD) of the projection matrix, the observability matrix and the Kalman state matrix can be estimated:

$$O_i = (U_1 \quad U_2) \begin{pmatrix} S_1 & 0 \\ 0 & 0 \end{pmatrix} \begin{pmatrix} V_1^T \\ V_2^T \end{pmatrix} \tag{2.32}$$

where  $U_1 \in \mathbb{R}^{n_c i \times n}$ ,  $S_1 \in \mathbb{R}^{n \times n}$ ,  $V_1 \in \mathbb{R}^{n_c i \times n}$  and  $n$  (model order) is the rank of the  $O_i$  matrix.  $\Gamma_i$  and  $\hat{X}_i$  can be chosen as follows:

$$\begin{aligned}
\Gamma_i &= U_1 S_1^{1/2} \\
\hat{X}_i &= S_1^{1/2} V_1^T
\end{aligned} \tag{2.33}$$

The shifted Kalman state sequence is obtained using equation (2.31):

$$\hat{X}_{i+1} = (\Gamma_{i-1})^+ O_{i-1} \tag{2.34}$$

where  $\Gamma_{i-1}$  is obtained by removing  $n_c$  rows of the  $\Gamma_i$  matrix and  $^+$  denotes the Pseudo inverse<sup>1</sup>.

Finally, the system and observability matrices are estimated:

$$\begin{pmatrix} \hat{A} \\ \hat{C} \end{pmatrix} = \begin{pmatrix} \hat{X}_{i+1} \\ Y_{i|i} \end{pmatrix} \hat{X}_i^+ \quad (2.35)$$

## Covariance-driven SSI

Covariance-driven SSI relies on this fundamental property of the stochastic state-space system that the output covariances can be decomposed as equation (2.20) [17]. A block Toeplitz matrix comprising output covariances could be decomposed to extended the observability matrix,  $\Gamma_i$ , and extended the stochastic contorability matrix,  $\Delta_i$ :

$$T_{\parallel i} = \begin{pmatrix} \Lambda_i & \Lambda_{i-1} & \cdots & \Lambda_1 \\ \Lambda_{i+1} & \Lambda_i & \cdots & \Lambda_2 \\ \cdots & \cdots & \cdots & \cdots \\ \Lambda_{2i-1} & \Lambda_{2i-2} & \cdots & \Lambda_i \end{pmatrix} = \begin{pmatrix} C \\ CA \\ \vdots \\ CA^{i-1} \end{pmatrix} \begin{pmatrix} A^{i-1}G & \cdots & AG & A \end{pmatrix} = \Gamma_i \Delta_i \quad (2.36)$$

By having  $n_c$  measurement channels, each of the covariance matrices will have dimensions  $n_c \times n_c$  [3]:

$$\Lambda_i = \frac{1}{N-i} \mathcal{Y}_{(1:N-i)} \cdot \mathcal{Y}_{(1+i:N)} \quad (2.37)$$

Thus, the dimension of the block Teoplitz matrix is  $n_c i \times n_c i$ .  $\Gamma_i$  and  $\Delta_i$  can be estimated by SVD of  $T_{\parallel i}$ :

$$\begin{aligned} T_{\parallel i} &= U_1 S_1 V_1^T \\ \Gamma_i &= U_1 S_1^{1/2} \\ \Delta_i &= S_1^{1/2} V_1^T \end{aligned} \quad (2.38)$$

---

<sup>1</sup> a pseudoinverse  $A^+$  of a matrix  $A$  is a generalization of the inverse matrix. [Ben-Israel, Adi; Thomas N.E. Greville (2003). Generalized Inverses. Springer-Verlag. ISBN 0-387-00293-6.]

The system matrix (or state matrix) can be obtained using two methods. The first method uses the decomposition property of one lag shifted Toeplitz matrix as follows [3]:

$$T_{2i+1} = \begin{pmatrix} \Lambda_{i+1} & \Lambda_i & \cdots & \Lambda_2 \\ \Lambda_{i+2} & \Lambda_{i+1} & \cdots & \Lambda_3 \\ \cdots & \cdots & \cdots & \cdots \\ \Lambda_{2i} & \Lambda_{2i-1} & \cdots & \Lambda_{i+1} \end{pmatrix} = \Gamma_i A \Delta_i \quad (2.39)$$

The combining of equations (2.36) and (2.39) results in an equation for calculating the state matrix:

$$A = \Gamma_i^+ T_{2i+1} \Delta_i^+ \quad (2.40)$$

In the other method, matrix  $A$  is given by

$$\Gamma_{i(2:n)} \hat{A} = \Gamma_{i(1:n-1)} \quad (2.41)$$

where  $\Gamma_{i(2:n)}$  and  $\Gamma_{i(1:n-1)}$  are found by removing the first and last block of  $\Gamma_i$ . In both approaches, the observability matrix is obtained using the  $\Gamma_i$  matrix:

$$\hat{C} = \Gamma_{i(1:1)} \quad (2.42)$$

$\Gamma_{i(1:1)}$  is the first row block of the extended observability matrix

## 2.2.4 Modal parameters identification

As mentioned in section ‘Stochastic space state system in discrete time’,  $A = \exp(A_c \Delta t)$ .  $A_c$  can be decomposed to eigenvalues and eigenvectors; therefore, the discrete system matrix will be [11]

$$A = \Psi_A \mu \Psi_A^{-1} = \exp(\Psi \lambda \Psi^{-1} \Delta t) = \Psi \exp(\lambda \Delta t) \Psi^{-1} \quad (2.43)$$

Equation (2.43) shows that the complex modal matrix  $\Psi_A$  is equivalent to  $\Psi$ , except for an arbitrary scaling. As the observation matrix is the same for both continuous and discrete system, the mode shapes will be [11]:

$$[\Phi_1 \quad \Phi_2 \quad \dots \quad \Phi_m] = C.\Psi \quad (2.44)$$

From (2.43) the eigenvalues of a discrete system are:

$$\mu_j = e^{\lambda_j \Delta t}, j = 1, 2, \dots, m \quad (2.45)$$

Then, the natural eigenfrequencies and damping ratios are as follows:

$$\begin{aligned} \lambda_i &= \frac{\ln(\mu_i)}{\Delta t} \\ f_i &= \frac{|\lambda_i|}{2\pi}, j = 1, 3, \dots, 2n-1 \\ \zeta_i &= -\frac{\text{Re}(\lambda_i)}{|\lambda_i|} \\ \Phi &= C.\Psi \end{aligned} \quad (2.46)$$

## 2.3 Frequency Domain Identification

The frequency domain methods are based on the auto and cross spectrum calculation. In the basic frequency domain (BFD) method, modal properties are identified by picking the peaks of power spectral density (PSD) plots [3]. In this method, if only one mode is dominant around a resonance, the structural response can be estimated as the modal response. This method has problems with closely spaced modes and noisy measurements. In closely spaced modes, the stronger mode is dominant, and in noisy measurements, peaks are not clear in PSD plots. In this simple peak picking method damping ratio estimation is not accurate according to [19] and the estimated eigenfrequency depends on the frequency resolution. Apart from the disadvantages, BFD is a simple, user friendly and undemanding method in terms of computational effort [3].

### 2.3.1 Frequency Domain Decomposition

Frequency domain decomposition (FDD) has been introduced as an extension to BFD for removing disadvantages [20]. This method is based on the SVD of the PSD matrix of the measured output. The mathematical background of this method is based on the modal decomposition of a dynamic response [21]:

$$y(t) = \varphi_1 q_1(t) + \varphi_2 q_2(t) + \dots \quad (2.47)$$

Here,  $q(t)$  is the modal coordinate and  $\varphi$  is the mode shape. By gathering all the modal coordinates in the column vector  $p(t)$  and all mode shapes in matrix  $\Phi$ , the equation (2.47) becomes:

$$y(t) = \Phi \cdot p(t) \quad (2.48)$$

Regarding equation (2.48), the correlation matrix is obtained by the following equation:

$$R_{yy}(\tau) = E[y(t+\tau)y(t)^T] = \Phi \cdot R_{pp}(\tau) \cdot \Phi^T \quad (2.49)$$

where  $R_{pp}(\tau)$  is the correlation matrix of the modal coordinates that are uncorrelated for the stochastic dynamics. Hence,  $R_{pp}(\tau)$  is a diagonal matrix with the auto-correlations of modal coordinates as the diagonal elements [21]. By taking the Fourier transform of equation (2.49), the response PSD matrix can be formulated as:

$$G_{yy}(\omega) = \Phi G_{pp}(\omega) \Phi^T \quad (2.50)$$

where  $G_{pp}(\omega)$  is the PSD matrix of the modal coordinates and it is diagonal for uncorrelated modal coordinates.

The response PSD matrix at frequency  $\omega$  can be decomposed by SVD:

$$G_{yy}(\omega) = USV^T \quad (2.51)$$

Since the PSD matrix is a Hermitian positive definite matrix,  $U = V$  [3], and equation (2.51) becomes:

$$G_{yy}(\omega) = USU^T \quad (2.52)$$

By comparing equation (2.51) with equation (2.52), it is realized that singular vectors can be equivalent to the mode shapes. The singular values are also the auto PSD functions of the corresponding single degree of freedom (SDOF) system associated with the same mode [3]. Since singular values are stored in a descending order, near the resonance frequency, first singular value contains information about the dominant mode at that frequency.

The number of nonzero elements in  $S$  matrix at a particular frequency indicates the rank of the PSD matrix at that frequency which can identify the closely spaced or coincident modes [3]. In other words, the number of dominant singular values shows the number of modes contributing on that frequency.

Frequency domain decomposition starts with the calculation of the PSD matrix. This matrix contains the cross spectrum between all the measurement channels in every particular frequency. Consequently, the PSD matrix in each frequency is decomposed by the SVD method. Therefore, for each frequency, a set of singular values and vectors are obtained, and singular values are all plotted in a singular value plot.

More detailed modal identification in FDD is conducted using the modal assurance criterion (MAC) number. The estimated mode shapes (singular vectors) around a peak frequency in the singular value plot are compared using the MAC number [22]:

$$MAC = \frac{|\Phi_i^T \Phi_j|}{\{\Phi_i^T \Phi_i\} \{\Phi_j^T \Phi_j\}} \quad (2.53)$$

where MAC is the modal assurance criterion between two singular vectors of  $\Phi_i$  and  $\Phi_j$ . The MAC number is a measure of the correlation between two singular vectors; therefore, as long as the MAC number between the singular vector at the peak and the singular vectors around the peak are larger than the MAC rejection level, the singular values belong to the same SDOF power spectrum density function. For calculating the damping ratio and natural frequency, this range around each peak of resonance in the singular value plot is taken to the time domain by inverse fast Fourier transform (FFT). In the time domain, the spectral density function is transformed to free decay of the auto-correlation function of the SDOF system; then, the natural frequency and the damping ratio are obtained by cross times and logarithmic decrement of the free decay [22]. In this way, the natural frequency is estimated by counting the number of times that the auto-correlation function crosses the time axis, and the damping ratio is obtained by fitting a logarithmic curve to the auto-correlation function free decay [23], as shown in Figure 2.1.

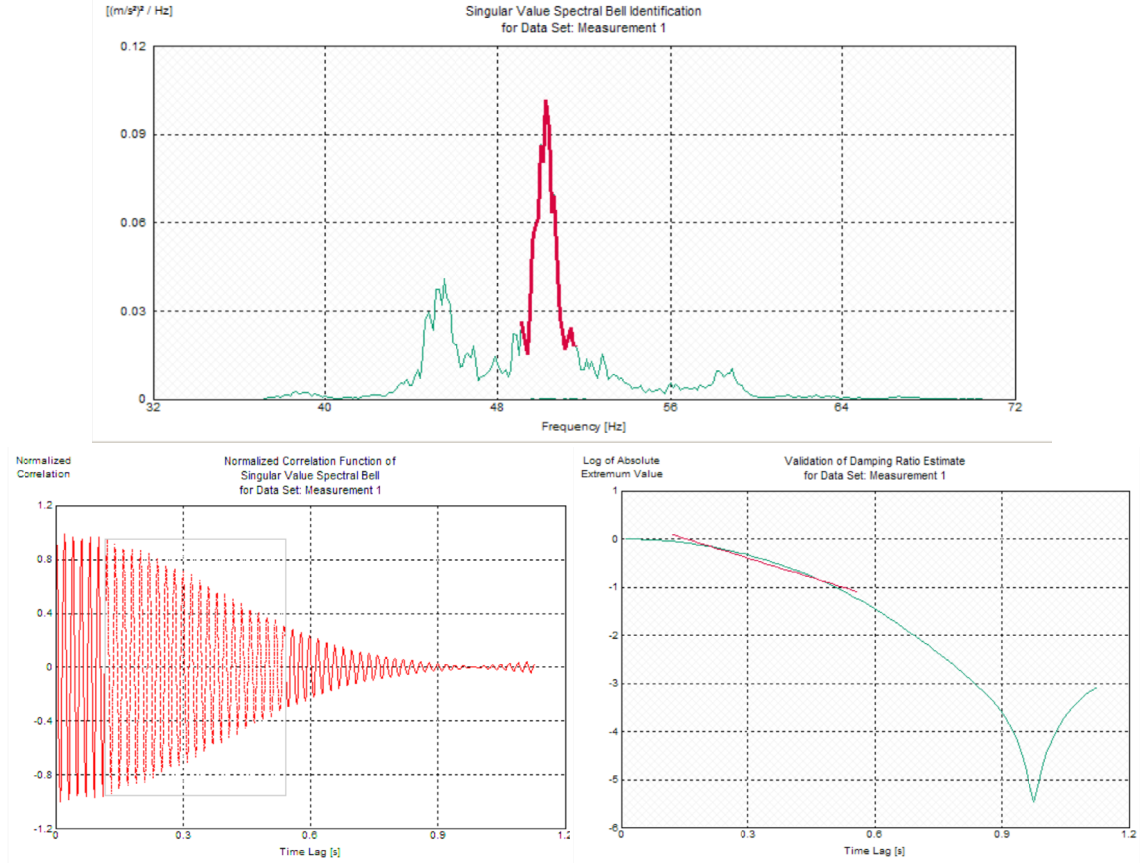


**Figure 2.1:** Top: Singular value spectral function identification using MAC rejection level. Bottom-Left: corresponding auto-correlation function of the SDOF. Bottom - Right: fitting the logarithmic curve to the free decay for finding damping ratio [23]

After numbering all the extrema (peaks and deeps) in the auto-correlation function plot, the logarithmic decrement  $\delta$  is calculated using the initial value ( $r_0$ ) and the  $k^{\text{th}}$  extremum value ( $r_k$ ) of the correlation function [22]:

$$\delta = \frac{2}{k} \ln\left(\frac{r_0}{r_k}\right) \quad (2.54)$$

Then, the damping ratio is given by:

$$\zeta = \frac{\delta}{\sqrt{\delta^2 + 4\pi^2}} \quad (2.55)$$

The undamped natural frequency  $f$  is obtained using damped natural frequency from the crossing zeros  $f_d$  and the damping ratio:

$$f = \frac{f_d}{\sqrt{1 - \zeta^2}} \quad (2.56)$$

## References

- [1] He, J., and Fu, Z. F. (2001): *Modal Analysis*, Butterworth-Heinemann, Oxford.
- [2] Zhang, L., Brincker, R., and Andersen, P. (2005): An Overview of Operational Modal Analysis: Major Development and Issues, Proceedings of the 1st International Operational Modal Analysis Conference, April 26-27, 2005, Copenhagen, Denmark.
- [3] Rainieri, C., and Fabbrocino, G. (2014): *Operational Modal Analysis of Civil Engineering Structures*, Springer, New York.
- [4] George, H., et al. (1993): The Natural Excitation Technique (NExT) for Modal Parameter Extraction From Operating Wind Turbines, SANDIA REPORT SAND92-1666 1 UC-261, National Technical Information Service, United States.
- [5] Ashwill, T. D. (1992): Measured Data for the Sandia 34-Meter Vertical Axis Wind Turbine, SAND91-222, National Technical Information Service, United States.
- [6] Carne, T. G., et al. (1988): Modal Testing the EOLE, SANDIA REPORT SAND87-1506.UC-60, National Technical Information Service, United States.
- [7] Brincker, R., and Ventura, C. (2015): *Introduction to Operational Modal Analysis*, Wiley, United States.
- [8] Richard, S., et al. (1992): A Consistent-Mode Indicator for The Eigensystem Realization Algorithm, NASA Technical Memorandum 107607.
- [9] Bazan, F. S. V. (2004): Eigensystem realization algorithm (ERA): reformulation and system pole perturbation analysis, pp. 433-444, *Journal of Sound and Vibration* 274.
- [10] De Callafon, R. A., et al. (2008): General Realization Algorithm for Modal Identification of Linear Dynamic Systems, pp. 712-722, *Journal of Engineering Mechanics* 134.
- [11] Andersen, P. (1997), *Identification of Civil Engineering Structures using Vector ARMA Models*, Ph.D. Thesis.
- [12] Peeters, B., De Reock, G., and Andersen, P. (1999): Stochastic System Identification; Uncertainty of the estimated Modal Parameters, IMAC XVII - 17th International Modal Analysis Conference.
- [13] Kirkegaard, P. H., and Andersen, P. (1997): State Space Identification of Civil Engineering structures from Output Measurements, Proceedings of the 15th International Modal Analysis Conference, Orlando, Florida.
- [14] Peeters, B., and De Reock, G. (1999): Reference-Based Stochastic Subspace Identification For Output-Only Modal Analysis, pp. 855-878, *Journal of Mechanical Systems and Signal Processing* 13.
- [15] Overschee, P. V., De Moor, B. (1996): *Subspace Identification for Linear Systems*, Kluwer Academic Publishers.
- [16] Naik, A. S. (2010): Subspace based data-driven designs of fault detection systems, Ph. D. Thesis, University of Duisburg-Essen, Department of Electrical and Computer Engineering.
- [17] Peeters, B., et al. (1995): Stochastic subspace techniques applied to parameter identification of civil engineering structures, Proceedings of New Advances in Modal Synthesis of Large Structures: Nonlinear, Damped and Nondeterministic Cases, pp. 151-162, Lyon, France, 5-6 October 1995.
- [18] Hermans, L., and Der Auweraer, H. V. (1999): Modal Testing And Analysis Of Structures Under Operational Conditions: Industrial Applications, pp. 193-216, *Journal of Mechanical Systems and Signal Processing* 13.
- [19] Peeters, B. (2000): *System Identification and Damage Detection in Civil Engineering*, Ph. D. Thesis
- [20] Bincker, R., Zhang, L., and Andersen (1999): Modal Identification from Ambient Response using Frequency Domain Decomposition, pp. 625-630, MAC 18: Proceedings of the International Modal Analysis Conference (IMAC), San Antonio, Texas, USA.
- [21] Bincker, R. and Zhang, L. (2009): Frequency Domain Decomposition Revisited, Proceedings of the 3rd International Operational Modal Analysis conference, IOMAC 09.



- [22] Bincker, R., Ventura, C. E., and Andersen, P. (2001): Damping Estimation by Frequency Domain Decomposition, Proceedings of the 19th International Modal Analysis Conference (IMAC), p 698-703.
- [23] Gade, S. (2006): Frequency Domain Techniques for Operational Modal Analysis, IMAC-XXIV: Conference & Exposition on Structural Dynamics.

## **3. Turbine blade experiment in the field**

### **3.1 Motivation**

The following chapter describes the application of the stereo vision technique on a 1-kW vertical-axis wind turbine rotor blade subjected to random vibrations. The operational modal analysis (OMA) study has also been implemented on the derived data to obtain mode shapes and numerical simulation has been conducted. Finally, the numerical results were compared with the classical modal analysis (EMA) and OMA results. The displacement time series used in the analysis are very short because of the limitations in the image acquisition system. Short time series are not fully qualified for OMA, and the analysis of the data needs a proper method. The covariance-driven stochastic subspace identification method (SSI-COV) has been performed for short time series like earthquakes. In the SSI-COV method, a block Toeplitz matrix that contains output correlation functions is formed. Ten displacement time series have been recorded with a 187-Hz sampling rate, and the time series from three measurements were chosen to be analysed and the block Toeplitz matrix of the time series are averaged out. For OMA validation, an EMA is conducted with signals from accelerometers mounted on the blade. The blade is excited with a hammer and the natural frequencies are estimated by picking the peaks from the frequency response functions (FRFs) obtained at different points. Finally, the natural frequencies and mode shapes obtained from the EMA and OMA results are compared with those of the numerical simulations of the blade with COMSOL (a multiphysics simulation tool).

### **3.2 Blade Description**

The blade used in this experiment is a modified Troposkein blade fitted on a small 1-kW vertical-axis wind turbine with a 2 m diameter. The Troposkein blade shape is slightly modified at the top and at the bottom and the blades are supported by two spokes, as shown in the Figure 3.1.

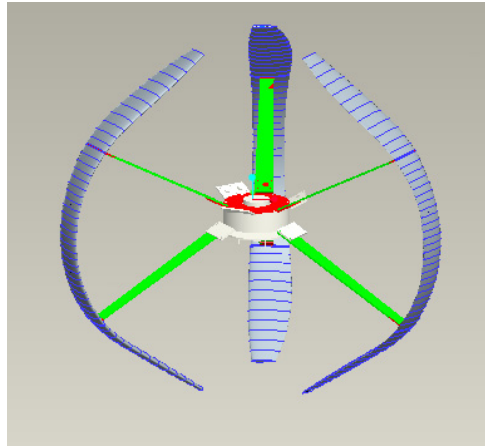


**Figure 3.1:** Rotor

The blade is made with a rapid prototyping material with the following mechanical properties:

- Material density =  $1150 \text{ kg/m}^3$ ;
- Young's modulus,  $E = 1.285 \text{ GPa}$ ;
- Weight =  $16 \text{ kg}$

The blade is designed with varying airfoil chord and thickness, as represented in Figure 3.2, where the hinges connected to the blades are shown with red squares:

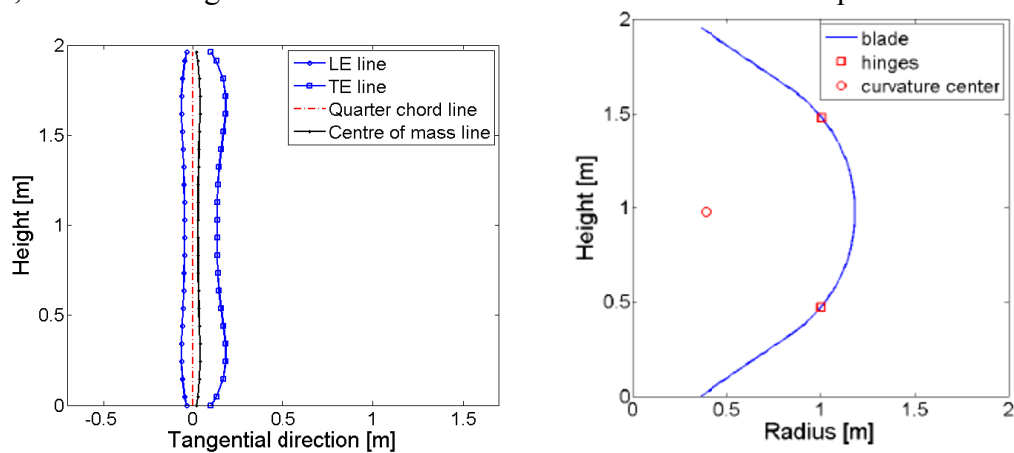


**Figure 3.2 :** Blade profile (LE: leading edge, TE: trailing edge)

An internal steel frame was designed to strengthen the entire structure. One rectangular void and two circular holes were made on the blade profile. Two steel plates with  $30 \times 1 \text{ mm}^2$  sections and four 1-mm-diameter steel wires were inserted into the rectangular void and the circular holes, respectively. The blade profile can be seen in Figure 3.3.

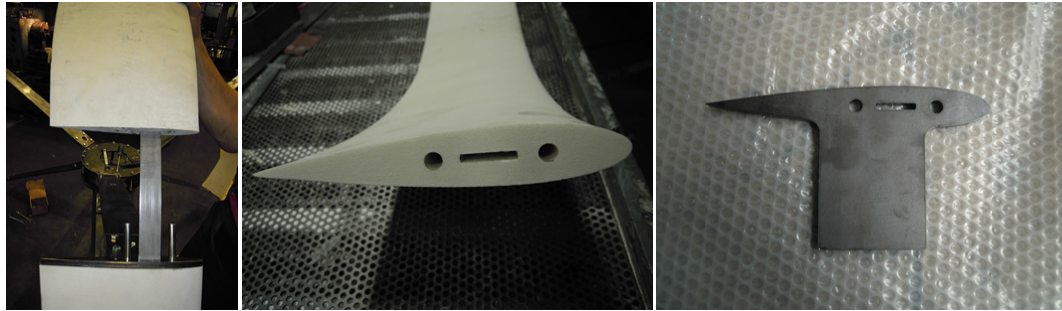


**Figure 3.3:** Blade profile details

## **3.3 Classical modal experiment**

### **3.3.1 Experiment setup**

In EMA, single-axis accelerometers are used to detect the mode shapes of the structure. In this experiment, the accelerometers were installed on the blade external surface at several points. These points were obtained by projecting the structure centroid line (centre of mass line) on the blade external surface. Indeed, by mounting the accelerometers on the projected centroid line of the blade on the surface, the accelerometers are placed on a row with a distance from the centroid line and can sense the torsional motion; therefore, torsional natural frequencies can be detected. On the other hand, while there is just one row of sensors, the torsional modes around the elastic axis are observed like a rigid body motion, and the torsional natural frequencies will be picked up and seen in the spectra. The instrumented blade was placed horizontally on two symmetrically spaced supports (red points in Figure 3.4).

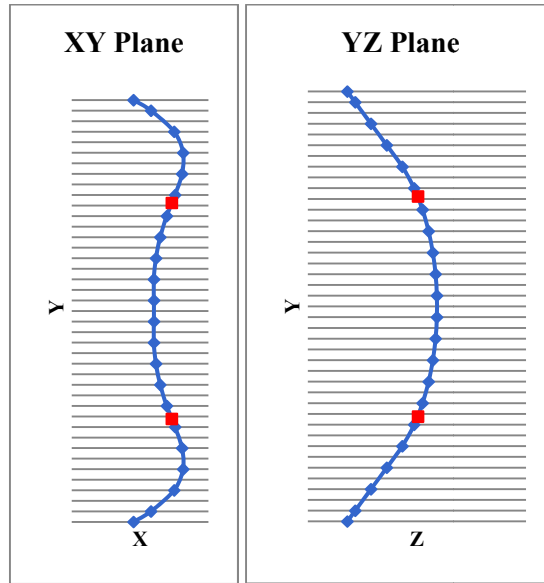


**Figure 3.4:** 24 Accelerometer positions (blue points) and two support points (red points); vertical axes represents the  $Y$  direction and horizontal axes represents  $X$  and  $Z$  directions.

The blade is resting with its weight on the supports that can rotate around the  $X$  axis and around the  $Y$  direction. Actually, these points represent the hinge position on the real wind turbine (Figure 3.5).

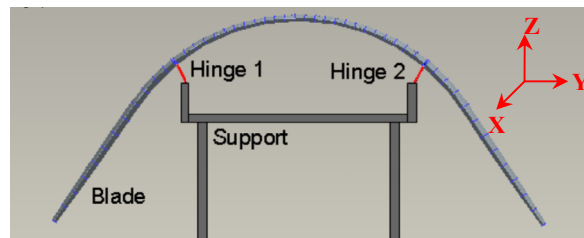


**Figure 3.5:** Configuration of the supports

Measurements were set up in the PULSE LabShop software (product of Brüel and Kjær Company). Thirty-six sets of measurements are organized in Pulse, and 3 points are measured in each set while the blade is hammered. In the first 18 sets, the blade was hammered in point 14, and the accelerometers moved around and measured acceleration in the  $Y$  and  $Z$  directions with a sampling frequency of  $256 \text{ Hz}$ . In the next 18 sets, the blade was hammered with the excitation force of about  $7 \text{ N}$  in point 24 and the accelerometers were moved along the blade (Figure 3.6).

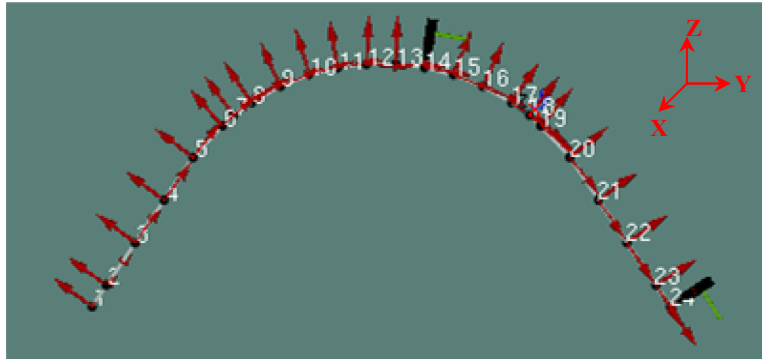


**Figure 3.6:** Measurement setup in the YZ plane

### 3.3.2 Results

The FRFs obtained in the 24 points were investigated to identify the natural frequencies. FRFs obtained in four points are seen in Figure 3.7 according to the sense orientation of the particular accelerometer.

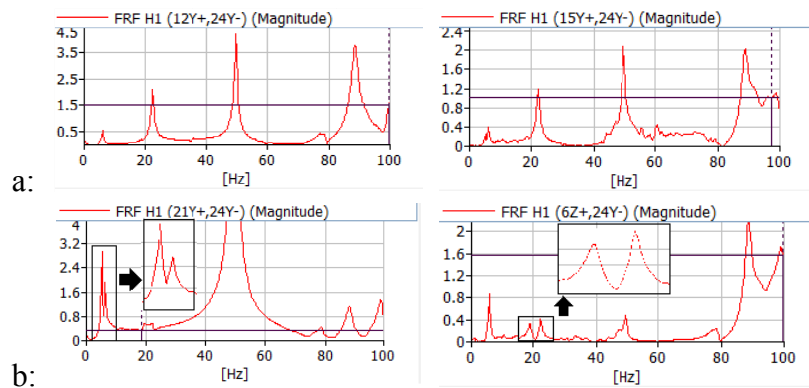


**Figure 3.7:** FRF in point No.6, 12, 15 and 21. The sensing direction (Z, Y) is indicated

By inspecting the FRFs, several obvious peaks in the plots indicate natural frequencies. In Figure 3.7-b the zoomed peaks in the FRF plots show two close modes in the frequency range of 4.5–6.5 Hz and two close modes between 18 and 22 Hz. The first four natural frequencies obtained by peak picking are estimated as follows:

**Table 3.1:** Natural frequencies by EMA

Mode No.	1	2	3	4
Natural Freq. (Hz)	4.75	6.50	18.25	22.00

### 3.4 Numerical Simulation

The blade modal behaviour was simulated using Solid Mechanics: Eigenfrequency module of the commercial finite element package COMSOL<sup>®</sup>. The model's geometry

comprises an isotropic material body with a core including a steel plate and two wires. Density, Young modulus and Poisson ratio of the blade are provided by the experiments. A free tetrahedral mesh is used to construct the FEM model. Supports are modelled as fixed rigid connectors with constrained rotation around the vertical axis, and they can freely rotate around the other axes so as to resemble the experimental conditions.

The natural frequencies and mode shapes are shown in Table 3.2 and Figure 3.8, respectively.

**Table 3.2:** Natural frequencies by numerical simulation

Mode No.	1	2	3	4
Natural Freq. (Hz)	4.78	6.45	20.41	22.33

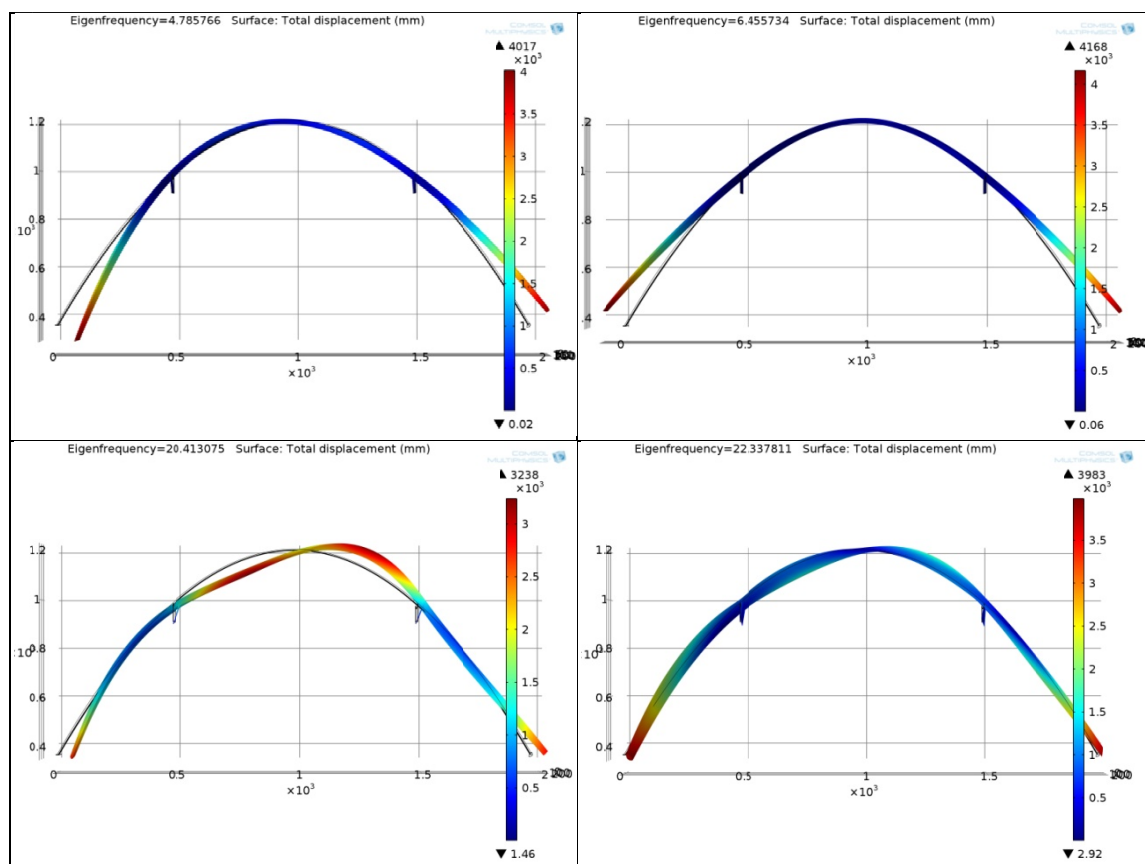


**Figure 3.8:** Mode shapes from FEM

### 3.5 Operational Modal Analysis

In the OMA test, the blade was placed outside in the field with the same boundary conditions and supports as in the EMA test. Vision sensors were simple paper markers with small black dots in the centre. They were placed at different positions on half of the turbine blade centroid projection line, and their 3D displacements were recorded



with a stereo vision system that was looking onto half of the blade while it was excited by the wind (6–8  $m/s$ ). We also try to excite the blade by random figure beats on the surface. The stereo system contains two Basler acA2040-180k cameras equipped with 60  $mm$  (focal length) Nikon lenses. The cameras take pictures at the frequency of 187 frames per second and the images are recorded on a computer hard drive. By processing the images taken from the excited blade in a particular time period, the displacement time series of the paper markers are extracted and used for OMA. The experimental setup is shown in Figure 3.9 and Figure 3.10.

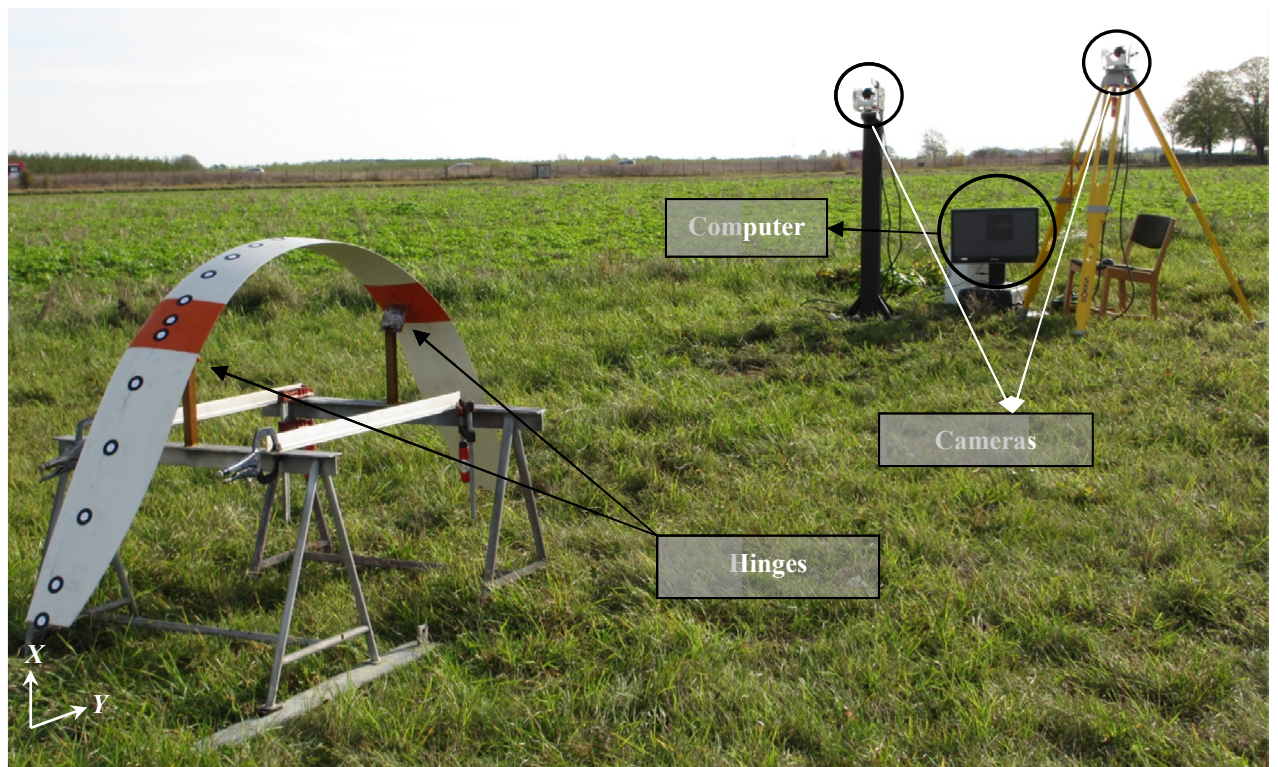


**Figure 3.9:** Experimental setup for OMA ( $Y$  axis is the same as EMA but  $X$  axis is  $Z$  axis of EMA)





**Figure 3.10:** Blade and hinges configuration

### 3.5.1 Camera calibration

The 3D reconstruction of a scene or the computation of the positions of objects in space need to link the 3D coordinate of the points in the world to their corresponding 2D coordinate in the image plane. Therefore, camera calibration solves the projection equations between known coordinates of a set of world points and their corresponding image points for the camera parameters.

Camera parameters are divided into extrinsic and intrinsic parameters. Extrinsic parameters define the location and orientation of the image reference frame with respect to a known world reference frame that contains the translation vector and rotation matrix. Intrinsic parameters characterize the optical, geometrical and digital characteristics of the camera. Intrinsic parameters are focal length,  $f$ , image centre in pixel coordinates  $(o_x, o_y)$ , the effective pixel size in the horizontal and vertical directions,  $(s_x, s_y)$  and, if required, radial distortion coefficient.

Figure 3.11 shows the world coordinate system  $(x^W, y^W, z^W)$ , camera reference frame  $(x^C, y^C, z^C)$  and image plane  $(x^I, y^I, z^I)$ .

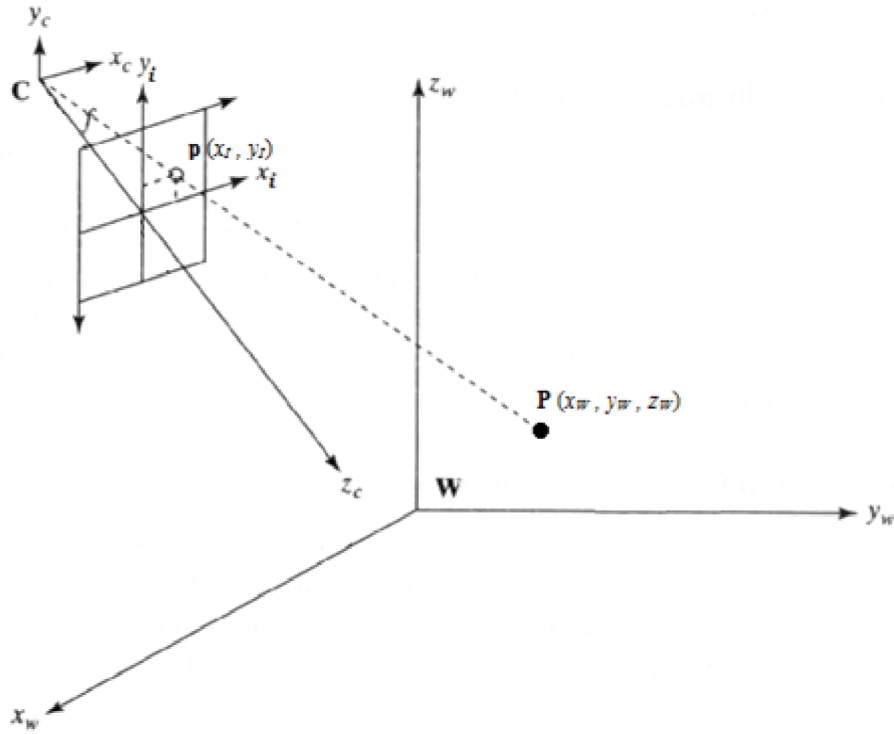


**Figure 3.11:** Different coordinate systems (C: Camera reference frame, i: Image coordinate, W: World coordinate) in image formation

The origin of the camera reference frame is the centre of projection, and z axis is the optical axis. The coordinates of a point  $P$  in world coordinate and camera reference frame are related with extrinsic parameters:

$$\begin{bmatrix} x^C \\ y^C \\ z^C \end{bmatrix} = R \begin{bmatrix} x^W \\ y^W \\ z^W \end{bmatrix} + T \quad (3.1)$$

where  $R$  is the rotational matrix and  $T$  is the translation matrix:

$$R = \begin{pmatrix} r_{11} & r_{12} & r_{13} \\ r_{21} & r_{22} & r_{23} \\ r_{31} & r_{32} & r_{33} \end{pmatrix}, \quad T = \begin{pmatrix} T_x \\ T_y \\ T_z \end{pmatrix} \quad (3.2)$$

Nikon modern lenses do not have distortion, then by neglecting the lens radial distortions, and referring to a pinhole camera model, the image reference frame coordinates and the image plane coordinates are connected by intrinsic parameters as follows:

$$\begin{aligned}
x^I &= -\frac{f}{s_x} \frac{x^C}{z^C} + o_x \\
y^I &= -\frac{f}{s_y} \frac{y^C}{z^C} + o_y
\end{aligned}
\tag{3.3}$$

The equations (3.1), (3.2) and (3.3) give [1]:

$$\begin{aligned}
x^I - o_x &= -\frac{f}{s_x} \left( \frac{r_{11}x^W + r_{12}y^W + r_{13}z^W + T_x}{r_{31}x^W + r_{32}y^W + r_{33}z^W + T_z} \right) \\
y^I - o_y &= -\frac{f}{s_y} \left( \frac{r_{21}x^W + r_{22}y^W + r_{23}z^W + T_x}{r_{31}x^W + r_{32}y^W + r_{33}z^W + T_z} \right)
\end{aligned}
\tag{3.4}$$

Thus, by having a set of points with known coordinates in the world frame and the image plane, it is possible to derive a set of equations, which will be solved for extrinsic and intrinsic parameters.

The first step before measuring is the calibration of the camera. In the current experiment, a calibration board (90 cm × 120 cm) was used, which contains 130 crosses with known coordinates. The calibration board is placed in front of the blade, as seen in Figure 3.12.

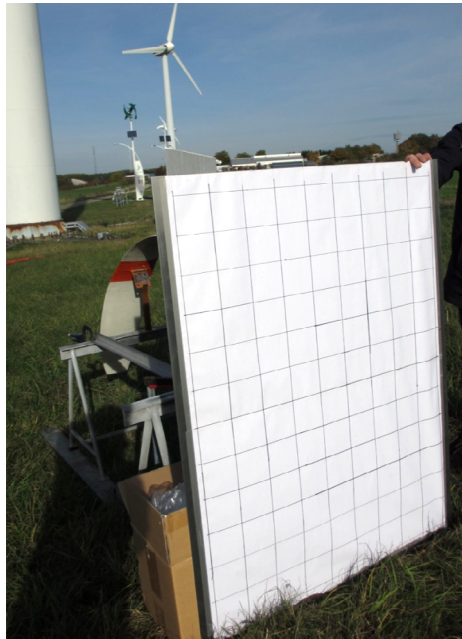


**Figure 3.12:** Calibration board

### 3.5.2 Image Processing

After calibrating the cameras, the images taken during the experiment are processed to get the corresponding displacement time series. As just a few points should be tracked in the images, the feature-based method was used to process the images and obtain the

displacement time series. The image processing algorithm starts with the identification of the approximate position of each marker in the images.

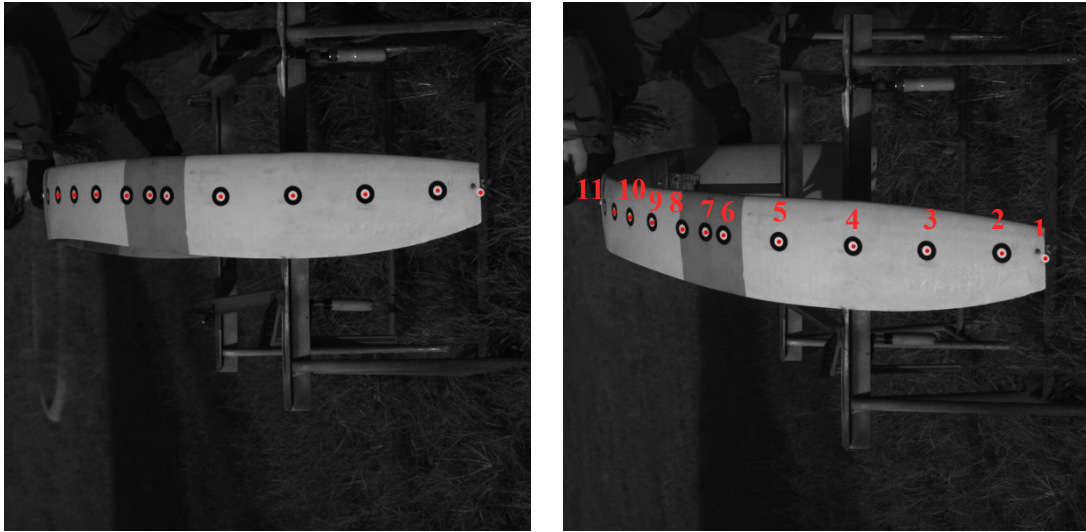


**Figure 3.13:** First estimation of the circular markers

As the entire structure is not expected to have large displacements during the measurement period, windows 1–11 are defined around the points in each image, and the markers are supposed to move within that window during the experiment time.

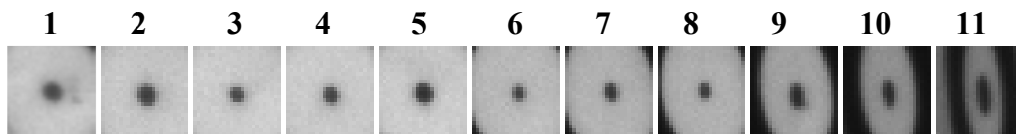


**Figure 3.14:** Image windows around the markers

Each of the image windows is binarized with a particular threshold depending on the mean intensity of the window, and then, the colours are made negative to get proper intensity concentration in the marker position. In the next step, the image windows are filtered for the expected marker features like size in pixel, marker location and marker's shape. Finally, the only remaining feature in the image window is the marker expressed in white colour and the background in black; the intensity centroid of the image window now gives the position of the marker centre without perspective correction (this topic will be discussed in section 4.4.1). The brief scheme of the image processing algorithm is shown in the following figure, more detailed explanation of the image processing will be found in the chapter 4.

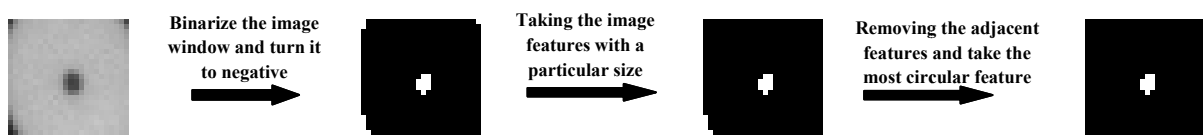


**Figure 3.15:** The summary of the image processing algorithm

The processing of the image sets illustrated a few hints to decrease the difficulties and errors:

- 1- Proper illumination of the setup is one of the important factors that will affect the image processing procedure. For easier and more robust image processing, it is better to have constant light intensity over time. Consequently, particular restrictions are not made in the code for each time step.
- 2- Having sufficient contrast between the marker and the background provides less error in finding the marker position. This can be achieved by precisely adjusting the light. Having a very strong or a weak light intensity will likely make errors on the marker boundaries in the pictures (the uncertainty will be discussed in the chapter 5).
- 3- If the entire structure and camera pods are sufficiently fixed, the same image windows can be used all over by the image processing algorithm; if they are not sufficiently fixed, a reference point has to be considered. Consequently, all the windows have to move with respect to the reference point displacements.
- 4- In the current experiment, the markers contained a small black dot in the centre of a larger white circle that was surrounded by a black ring and the central black dot was tracked in image processing. The black dot was not completely circular and its dimension was not well defined, and consequently, perspective correction was not done (section 4.4.1). In addition, the size of the dot was relatively small at some locations, which caused difficulties in image processing algorithm to distinguish the dot from the noise. Therefore, a better design of the marker can be a black circle with enough contrast with the background and a larger diameter in pixels compared with that in the current case. The new marker will make the image processing algorithm easier and more accurate.
- 5- Either very small or very big markers generate errors in the marker localization. As a rule of thumb in the experimental stereo vision society, the markers should represent between 10 and 20 pixels in an image.

### 3.5.3 SSI-COV analysis

After processing the image sets from several experiments, it was observed that the camera frequency had dropped after a particular time step. It is likely that the memory allocation problems obstructed the image acquisition with the maximum frame rate. To illustrate the problem, the deflection of the blade tip point is shown in Figure 3.16. The deflection of a point in the time step is:

$$d(i) = position(i+1) - position(i) \quad (3.5)$$

Figure 3.16 shows that the amplitude of the deflections has jumped suddenly after 1700 time steps (about 9.1 s) because of the image acquisition frequency drop. The rule-of-

thumb is to record at least  $\frac{1000}{n}$  s (where n is the lowest natural frequency of the structure) [2], which in this case is much longer than 1700 time steps.

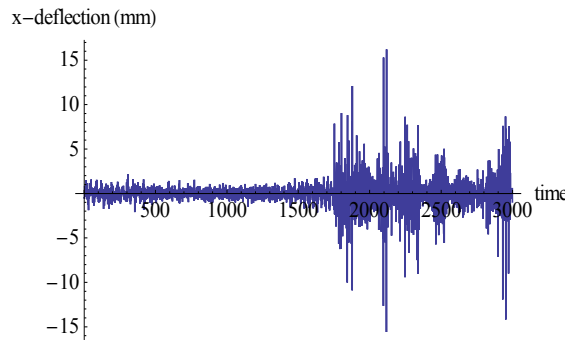
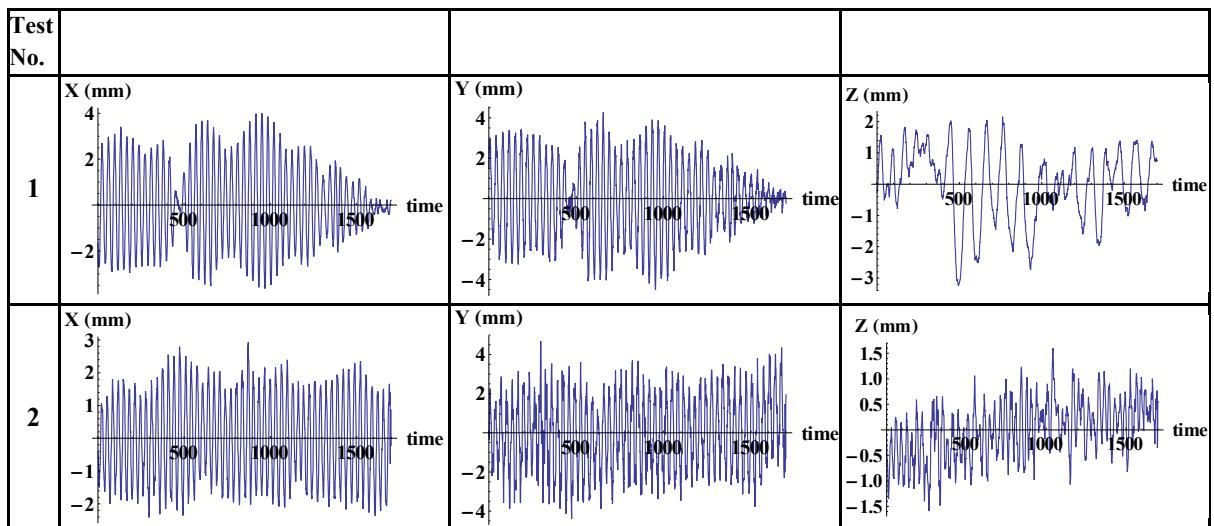


**Figure 3.16:** Tip point deflection time series (each of the intervals on the time axis is equal to 1 time step =  $\frac{1}{187}$  s)

Therefore, because of this limitation, only the first half of the time series can be used for the modal analysis. The experiment was conducted several times, and the time series from different experiments are involved in the modal analysis for extracting the maximum modal information of the blade.

SSI-COV provides the covariance matrix for the time series, which are normally noisy, and in each of them, a set of natural frequencies has been excited. By averaging the covariance matrices from different experiments, the derived covariance matrix with less noisy information will be prepared for the SSI-COV analysis.

By inspecting the peaks in the spectra of 10 sets of the displacement time series, three of them were chosen to cover all the first four frequencies, according to the simulation and EMA test.





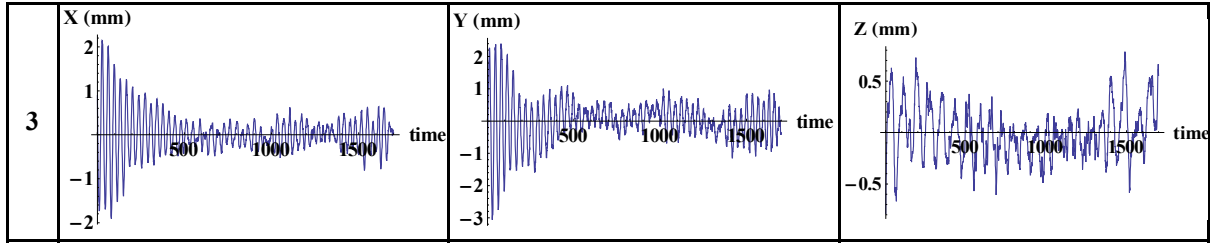


**Figure 3.17:** Displacement time series of the blade tip (each of the intervals on the time axis is equal to one time step =  $\frac{1}{187}$  s)

The block Toeplitz matrices,  $T_{1|i}$  and  $T_{2|i+1}$ , are calculated for each of the measurement sets using equations (2.36), (2.37) and (2.39) in chapter 2. Then,  $T_{1|i}$  and  $T_{2|i+1}$  are both averaged over three measurement sets to reduce the noise and include more information in the modal analysis. Averaged  $T_{1|i}$  is decomposed according to equation (2.38), and the state matrix  $A$  is estimated by using averaged  $T_{2|i+1}$  in equation (2.39). Finally, the modal properties are identified as explained in section 2.2.4.

## Stability Diagram

After the modal properties' identification, a number of eigenfrequencies are obtained for each model order, although not all of them are physical modes or real modes. Indeed, for the ideal case, the model order ( $n$ ) is simply the rank of the projection or Toeplitz matrix, where the diagonal elements of the singular matrix from SVD drops to a very small value. However, in the real experiment, there is no clear gap or drop between the singular values due to the measurement noise and modelling inaccuracies [3]. Therefore, the model order is usually over specified to include all the physical modes; however, it also introduces the spurious modes to the identified eigenmodes. These spurious modes can be noise modes or mathematical modes that are created due to the measurement noise, computational noise and modelling inaccuracies. For separating the physical modes from the spurious modes, all the identified modes are filtered for the physical modes properties [4]:

- 1- Structural modes are underdamped and their damping ratios are not more than a few percent.
- 2- Physical modes are in complex conjugate pair of eigenvalues.
- 3- Physical modes are repeated in all the model orders.

As has just been mentioned, the physical modes are present in all the model orders. However, if all the estimated eigenfrequencies for each of the model orders are plotted in a diagram, physical modes are aligned in the diagram and spurious modes are

scattered. This plot is called the ‘Stability diagram’. To check the repeatability of the physical modes, the modal assurance criterion (MAC) is a useful tool. As it has been described in chapter 2, the MAC number is a measure of agreement between two modes. The MAC number is calculated between each of the eigenmodes in a certain model order  $m$ , and all the eigenmodes belonging to the last proceeding model order  $m-1$ . If the maximum MAC number is less than the value given by the rejection level, the mode will not be physical and is removed from the stability diagram.

### 3.5.4 Results

Looking closely into the spectrum,  $S_{yy}$  (power spectral density: the Fourier transform of the auto-correlation) of the time series signal provides basic knowledge of the detected natural frequencies:

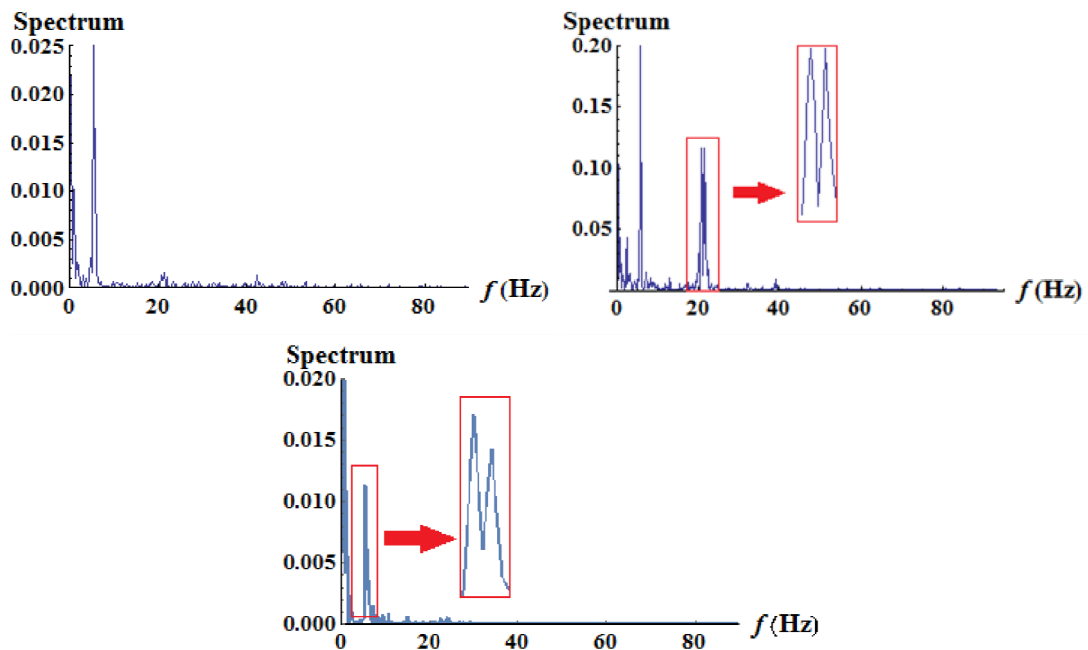


**Figure 3.18:**  $Y$ -Spectrum for three measurement sets

Spectrums are calculated with Bartlett’s method. In this method, the signal has been divided into several segments, and the power spectrum is averaged over the segments to reduce the noise [5]. As shown in Figure 3.17, the  $Y$  – displacement signals in the first and third measurements decay after a while, but there is no decay in the second measurement. This is why the spectrum of the second measurement has higher amplitude compared with that of the first and third measurements.

As is obvious from Figure 3.18, the first measurement indicates two peaks in the spectrum, with the lowest one of about 5.2 Hz and the second one of about 19.5 Hz. In the second measurement, there are three peaks in the spectrum, situated at about 5.8 Hz, 19 Hz and 21 Hz. However, the last two peaks are quite close. In the third measurement



spectrum, two close peaks are observed about 5.5 Hz. Thus, in each of the measurements, a set of the natural frequencies have been excited.

SSI-COV has been previously used for short time series like earthquakes and showed good results in the identification of modal properties [6,7]. Gathering covariance matrices in the block Toeplitz matrix helps cancel out the uncorrelated noise [8]. Furthermore, using covariance matrices in SSI-COV provides the possibility of involving different measurement sets in the modal identification, by an averaging approach. The averaged Toeplitz matrix is less noisy due to the averaging of the covariance matrices from different measurement sets and has information from all of them.

The averaged SSI-COV code was implemented in Mathematica and applied to the three mentioned time series. By having 11 markers on the centreline, where each of them are measuring displacement in the  $X$ ,  $Y$  and  $Z$  directions, the number of measurement channels for analysis will be  $n_c = 3 \times 11 = 33$ .

After modal identification, stability diagram (it is described in ‘Stability Diagram’ section) is plotted as follows.

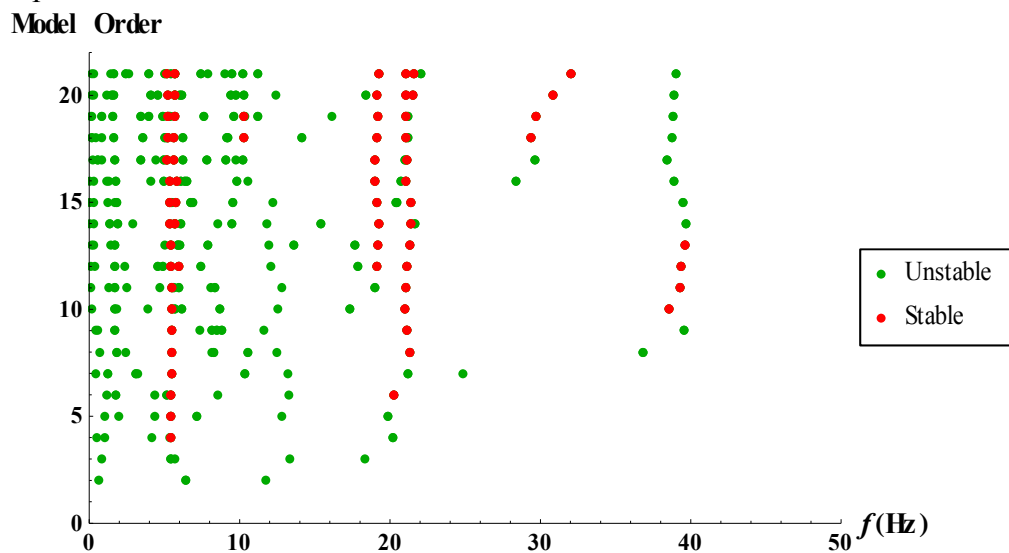


Figure 3.19: Stability diagram

The stable poles in the stability diagram have damping ratios less than 0.065 and MAC number more than 0.9. Considering the stable eigenfrequencies in the stability diagram, the natural frequencies and damping ratios are listed in the following table.

Table 3.3: natural frequencies and damping ratios

Mode No.	Frequency	$\sigma_f$	$\epsilon_f$	Damping ratio	$\sigma_\zeta$	$\epsilon_\zeta$
1	5.37	0.11	0.003	0.017	0.012	0.120
2	5.72	0.10	0.004	0.013	0.008	0.142
3	19.14	0.093	0.001	0.056	0.004	0.019
4	21.16	0.12	0.001	0.019	0.007	0.073

where  $\sigma$  is the standard deviation and  $\epsilon$  is a measure of uncertainty:

$$\epsilon_f = \frac{1}{\sqrt{N}} \frac{\sigma_f}{\bar{f}} \quad (3.6)$$

where  $\bar{f}$  is the mean value of  $f$  and  $N$  is the number of stable modes. As shown in Table 3.3, the uncertainty of estimated damping ratios and natural frequencies are higher for the two first modes than for the two last modes. On the other hand, there is the rigid body motion of the structure at very low frequencies of between 0 and 1 Hz, presumably induced by the blade rotation around  $X$  and  $Y$  axes, and it will lead to an increase in the uncertainties of lower modes.

As estimated in the numerical simulation, the 4<sup>th</sup> mode is a torsional mode. As described, this mode shape cannot be presented by only markers that are placed on the centreline. However, the frequency can be seen in the stability plot. The corresponding mode shapes (except the torsional mode) are shown in the following figure:

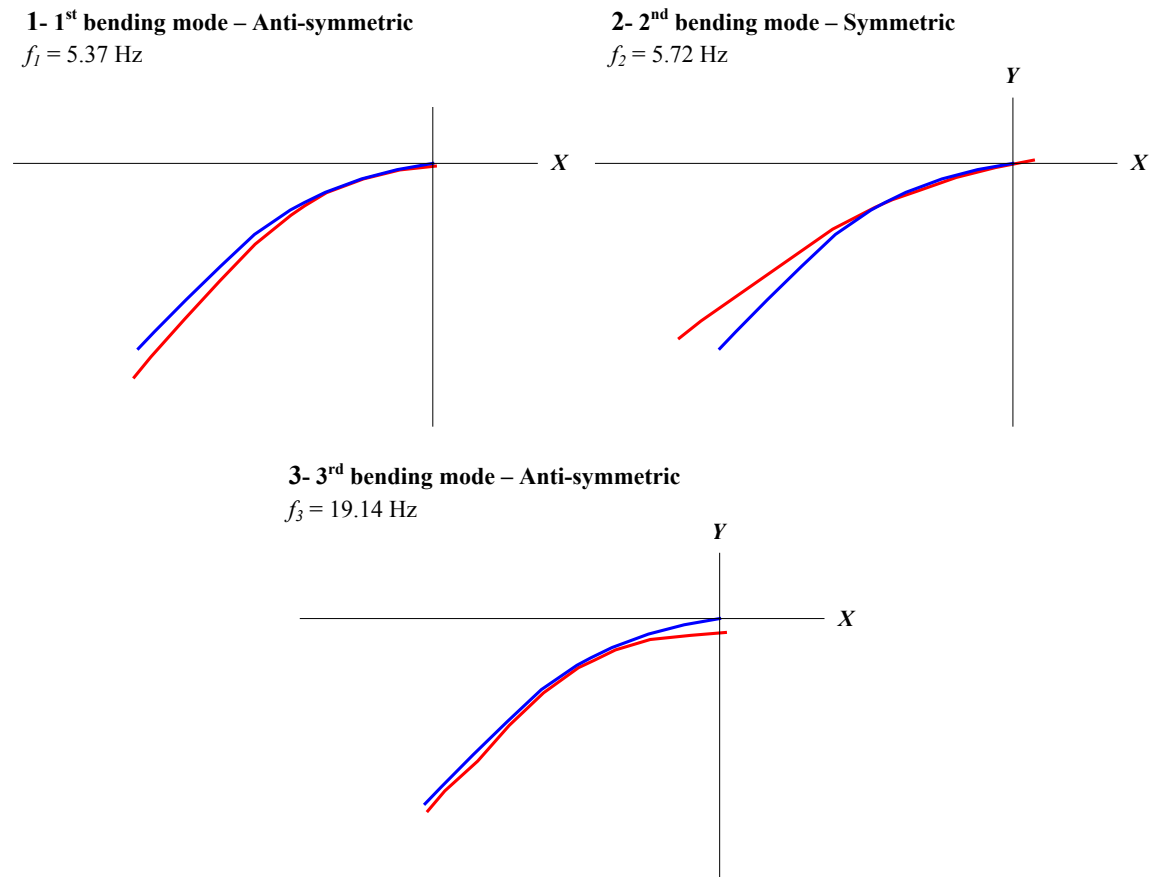


**Figure 3.20:** Mode shapes from OMA

## 3.6 Conclusions

In this chapter, the displacement measurement was conducted on a Troposkien blade by means of stereo vision technique and the modal properties were studied by OMA. The OMA results were compared with classical modal analysis (EMA and finite element simulation (FEM)). The first four natural frequencies from the simulation agreed fairly with the EMA results. The minor difference between the last two natural frequencies obtained from EMA and FEM might stem from considering the blade as an isotropic structure and simplifying the boundary conditions and supports, e.g. not including friction in the model.

In OMA, displacement time series were acquired using the stereo vision technique. The use of displacement rather than acceleration as the output has demonstrated easier, cheaper and direct procedures. It needs less preparation time, it does not suffer from noise due to the electronics and it does not add mass to the structure. The present stereo vision study was conducted in the open field and with existing markers. However, a few hints were obtained to provide more accurate displacement measurement via stereo vision, such as the proper illumination with constant light intensity over the time to avoid reflection and shadows on the surface. Some conclusive remarks on the marker shape and size were made, leading to a more convenient and simpler design.

In the current experiment, because of the hardware limitation, we were able to obtain only short displacement time series, which are not convenient for analysis with OMA. Within the short term measurement, all the blade natural frequencies might not be excited and all the modal properties will not show up. However involving different measurement sets in modal analysis, that in each of them a set of natural frequencies are excited, identifies the modal information of the blade. SSI-COV has been chosen to analyse the data. This method provides the possibility of averaging the covariance matrices belonging to the different measurement sets and cancelling out the uncorrelated noise in the covariance matrices. SSI-COV has been implemented to three of the 10 short displacement time series to cover the first four frequencies, according to the simulation and EMA test. By averaging the covariance matrices, the problems associated with the short time series are solved and the results almost agree with the numerical and other experimental results. In addition, the rigid body motion of the blade increased the uncertainty of the first natural frequencies and damping ratios.

## References

- [1] Trucco, E., Verri. A. (1998): *Introductory Techniques for 3-D Computer Vision*, Prentice Hall, New Jersey, United States.
- [2] Brincker, R., and Ventura, C. (2015): *Introduction to Operational Modal Analysis*, Wiley, United States.
- [3] Rainieri, C., and Fabbrocino, G. (2014): *Operational Modal Analysis of Civil Engineering Structures*, Springer, New York.
- [4] Andersen, P. (1997), *Identification of Civil Engineering Structures using Vector ARMA Models*, Ph.D. Thesis.
- [5] Vaseghi, S. V. (2008), *Advanced Digital Signal Processing and Noise Reduction*, Fourth Edition, John Wiley & Sons Ltd.
- [6] Siegert, D., et al. (2009). Variation of modal parameter estimates of a prestressed concrete bridge. *Proceedings of the IMAC-XXVII*.
- [7] Zhou, W., et al. (2010). Seismic Damage Assessment for a Residential Masonry Building Using Aftershock Monitoring of Wenchuan Earthquake, *Proceedings of 24th International Conference on Noise and Vibration Engineering (ISMA)*.
- [8] Bui, T. T., and De Reock, G. (2012). Vulnerability Assessment of Structures in a Low-To-Moderate Seismic Region based on Ambient Vibration Test Modal Data, *Proceedings of the Eleventh International Conference on Computational Structures Technology*.

## 4. VAWT experiment in the wind tunnel

### 4.1 Motivation

This chapter is the practical implementation of the basics derived in the chapters 1 and 2 about stereovision and operational modal analysis (OMA). The different methodologies for analysing vibrations limited to a parked vertical axis wind turbine are shown here. The experiment is designed to study the displacements in different parts of a 1-kW 3-bladed vertical axis wind turbine rotor during standstill in the wind tunnel of Politecnico Di Milano University<sup>1</sup>. A number of paper markers, which are black circles, were stuck on several places of the blades' centreline and the rotor shaft surface. Two Basler cameras (acA2040-180km) were installed at positions with almost no wind speed close to the open chamber of the high speed wind tunnel and with viewpoints towards the markers. The rotor is excited by high speed wind from the wind tunnel (25 m/s). By setting up appropriate light conditions and correct for perspective errors, the displacement time series have been obtained using a relatively robust image processing algorithm. The displacement time series are analysed with the data-driven stochastic subspace identification (DD-SSI) method, which uses the measurement data directly and has good convergence and less error compared with other methods. The SSI results are compared with the results derived from the frequency domain decomposition (FDD) method. Finally, a classical modal test is conducted to investigate the structural modes of the structure.

### 4.2 Experiment setup

The rotor diameter is 2  $m$ , and it was placed in the open chamber of the wind tunnel with section dimensions of  $4 \times 3.84 \text{ m}^2$ , as represented in Figure 4.1.

---

<sup>1</sup> <http://www.windtunnel.polimi.it/english/impianto/impianto.htm>

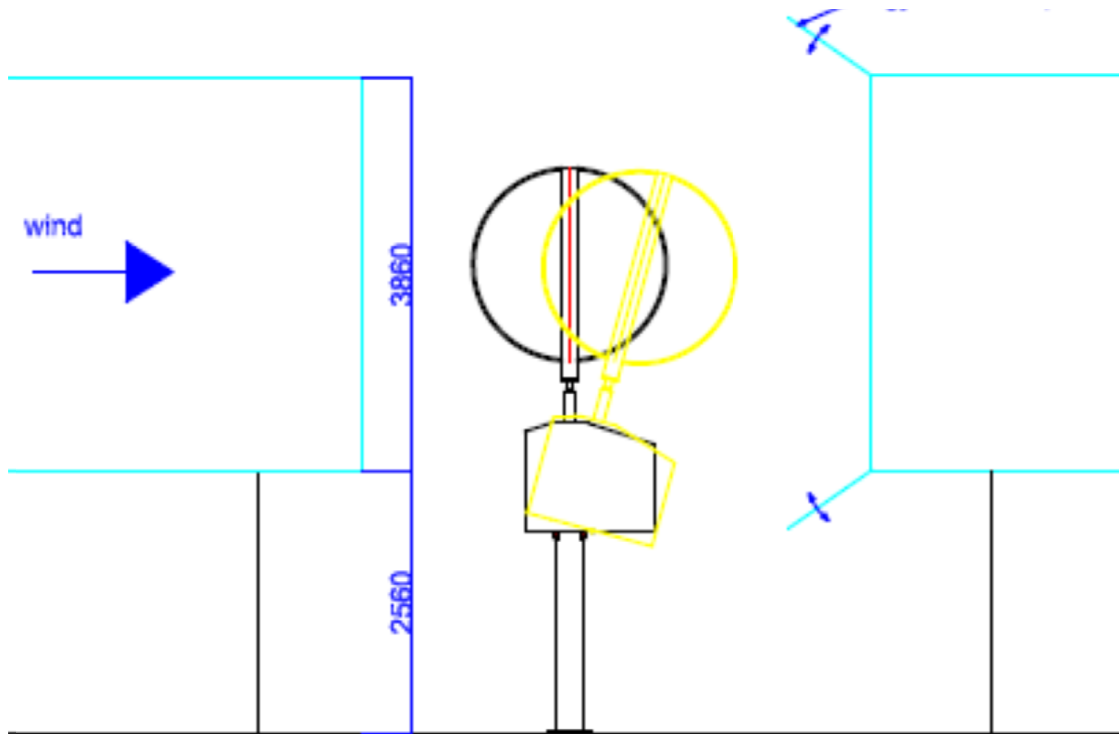


**Figure 4.1:** Turbine position in wind tunnel

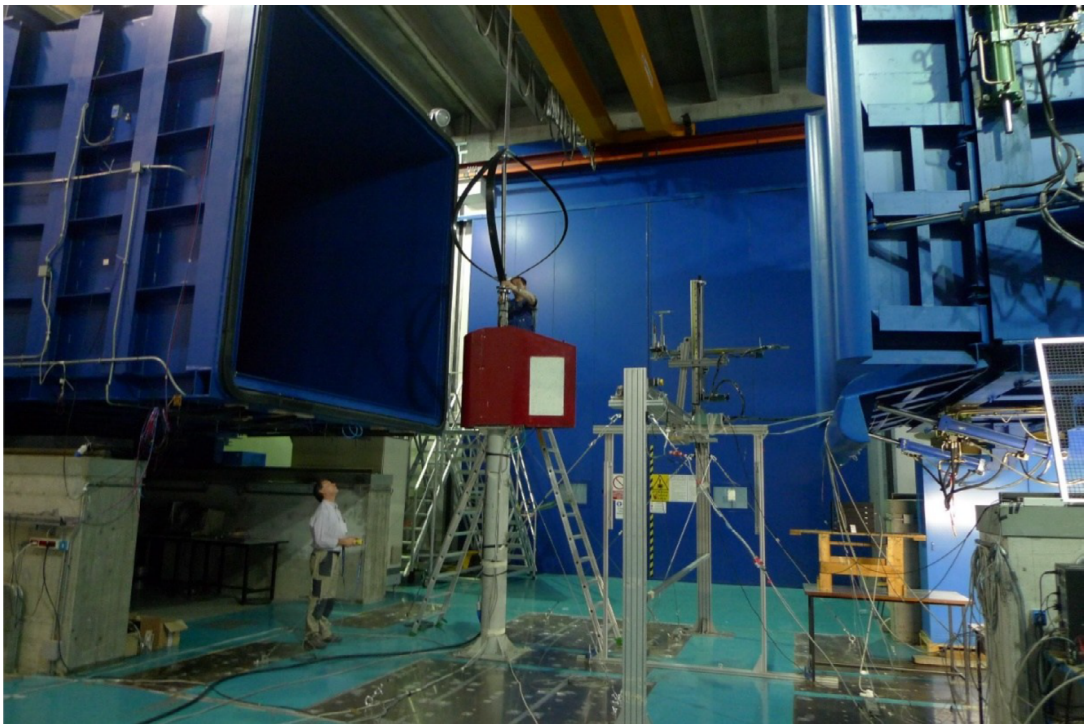


**Figure 4.2:** Experimental setup of the open chamber configuration of the Milan wind tunnel

Before placing the turbine in the wind tunnel, the markers had been attached to the suction and pressure side of the airfoil and on the rotor shaft surface centrelines (they are passing through the centre of masses of all the sections) with a distance of 10 cm between the markers. The marker diameter is 15 mm, which is chosen to occupy 10–20 pixels in the image according to the distance between camera and the VAWT. There are also a number of markers that are horizontally spaced to investigate the torsional behaviour of the blade. The markers on a blade together with the small calibration board are shown in Figure 4.3.

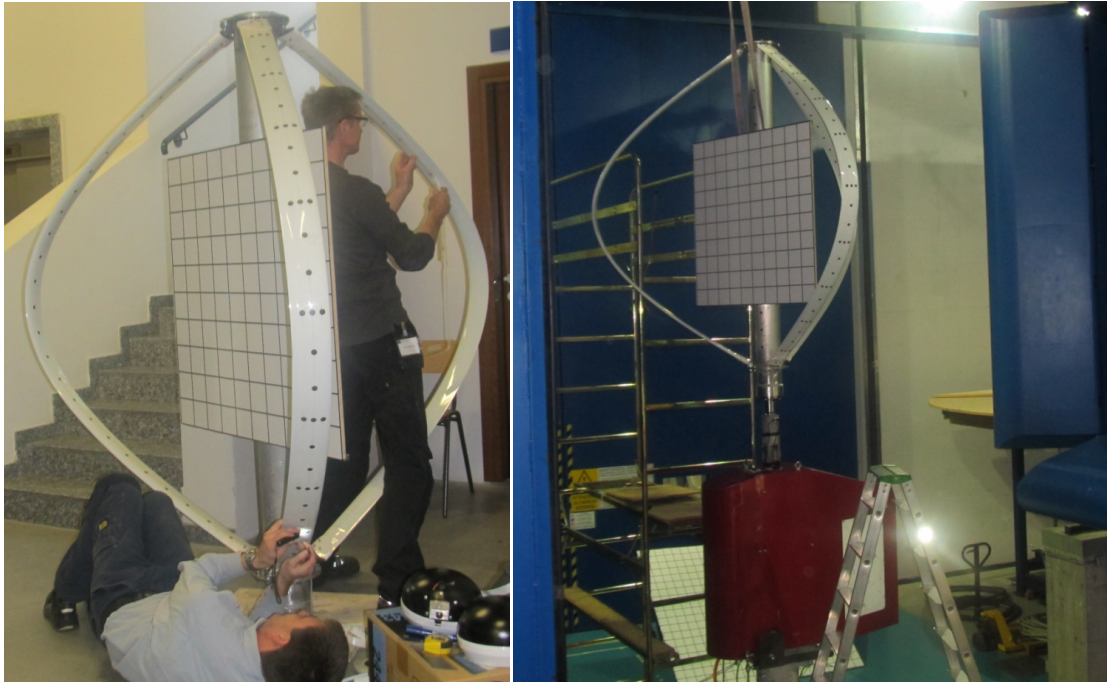


**Figure 4.3:** Attaching markers to the turbine<sup>1</sup>. The small calibration plate is also shown<sup>2</sup>

The cameras were mounted on two pods with a height of about 1.30 m, and they were put on a platform 3.3 m above the floor. In fact, the cameras will be viewing the same around the turbine centre point. The cameras were placed about 1.5–2 m apart and equipped with 40 mm (focal length) Nikon lenses. The distance between the cameras and rotor was about 7.5 m, which ensured that the rotor could be seen in the image plane, and markers would be representing between 10 and 18 pixels in different places on the rotor shaft and blades according to their positions.

<sup>1</sup> The black circles were printed on the long tapes with white background at defined distances, which makes the attaching process fast and easy.

<sup>2</sup> The small and large calibration board were tried to see which of them estimates the camera parameters more precisely, and the larger calibration board was chosen.





**Figure 4.4:** Camera locations

Because of the particular rotor geometry of the three bladed VAWT, all blades and rotor shaft cannot be simultaneously seen by two cameras. In the best case, two blades and the rotor shaft are visible in the stereo image planes. The cameras were installed in the structures attached to the pods with the flexibility of rotation to capture markers on two blades and the rotor shaft (Figure 4.5).



**Figure 4.5:** Camera housing

With regard to light problems encountered in the blade experiment, the light conditions were adjusted to be of constant intensity over time and to be evenly spread over the



volume of interest. In addition, the frame rate was relatively high and the exposure time was set to the possible smallest value for catching the small movements. Therefore, the time for capturing light was pretty short. Hence, a strong light with no reflections on the marker places is needed. To improve for light imperfections and prevent shadows, several spotlights were installed at different positions (Figure 4.6) to constantly light up different parts of the rotor.

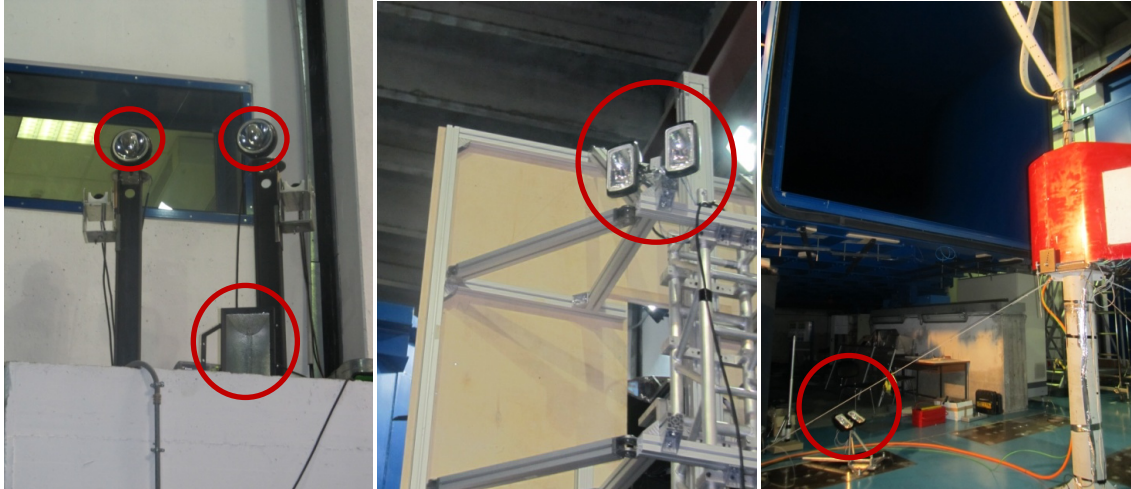


**Figure 4.6:** Spotlights at different positions

### 4.2.1 Data acquisition

The cameras were connected to a PC via 5-m-long cables. The cameras were programmed in LabView to simultaneously take pictures and store them on a high speed hard disk. All the variables such as exposure time, frame rate, image depth and area of interest (AOI) are controlled by the NI MAX software that is connected to NI frame grabbers (NI PCIe-1433). These frame grabbers are connected to the cameras to transfer the pictures in a digital format to the hard disk.

The computer had a 1 TB SSD RAID drive (speed of about 1 GB/s) to write the images taken during the experiment and two 3.63 TB drive (speed of about 200 MB/s) for data storage. The installed memory on the computer was 32 GB. These properties limit the time length of the acquired image series. For example, to represent a view of half the turbine, which contains two blades and rotor shaft, each picture will represent 2 MB in pixel size, and the longest image acquisition duration is about 32 s (6000 picture each camera).

## 4.3 Camera Calibration

As explained in the chapter 3, the cameras have to be calibrated before starting the actual measurement. For this purpose, the calibration board contains a  $2 m \times 2 m$  grid of

200 crosses printed and stuck on a wooden plate, as seen in Figure 4.7. Then, it will be fixed on the turbine rotor shaft.

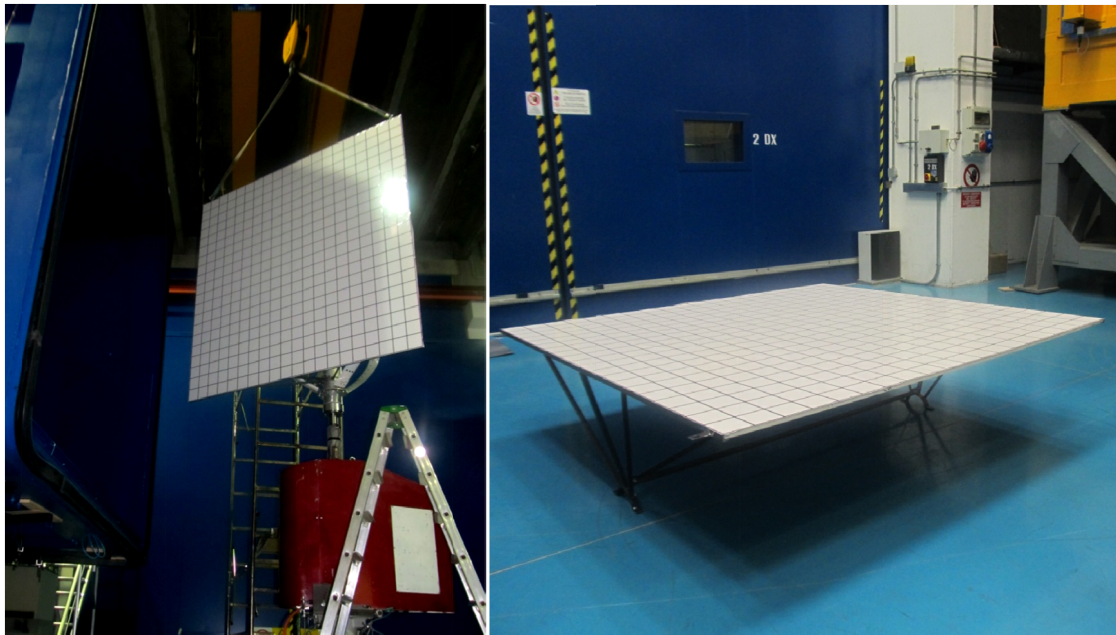


**Figure 4.7:** Calibration board

The calibration grid has been printed with the precision of better than 1/1200 dpi and fills the entire image area. The distance between the crosses is small in comparison to the image area to decrease the calibration uncertainties (the calibration uncertainties will be discussed in chapter 5).

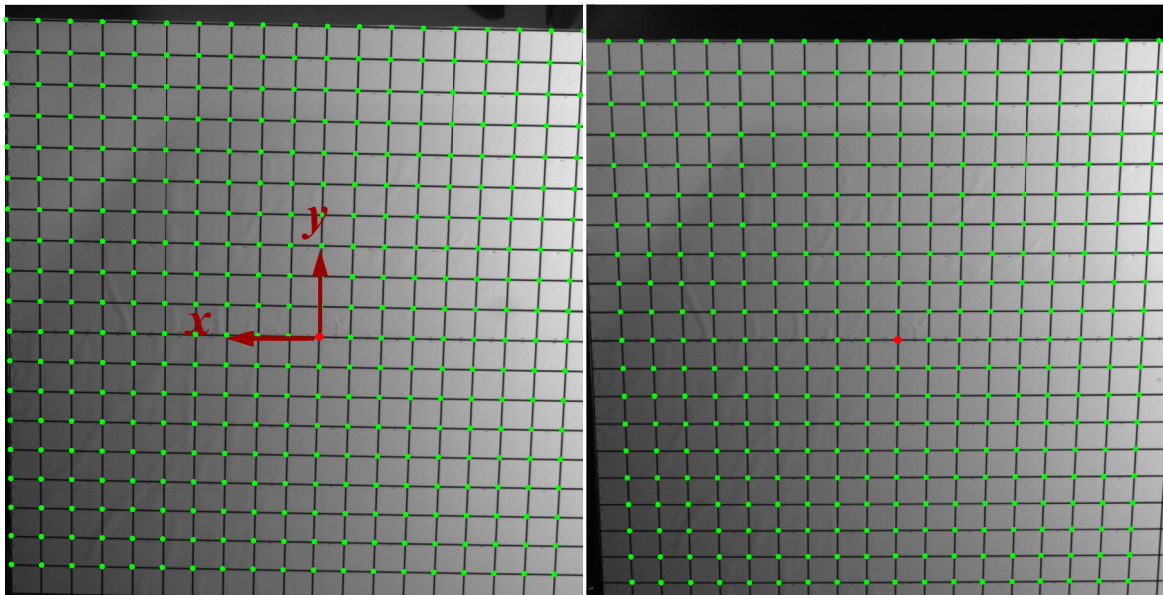


**Figure 4.8:** Left and Right calibration board image. Green points are the grid points and red point is the origin of the world coordinate system

In the calibration process, as has been mentioned in the chapter 4, the coordinates of the grid points are determined in both image coordinate and world coordinate. Then, the calibration matrix is found to take all the image points to the real world coordinate system.

## 4.4 Image Processing

As mentioned before, due to the limited number of viewpoints offered by only two cameras and hardware limitations, only a fraction of the wind turbine (rotor shaft and the two blades) is captured in the images for 32 s, as seen in Figure 4.9:

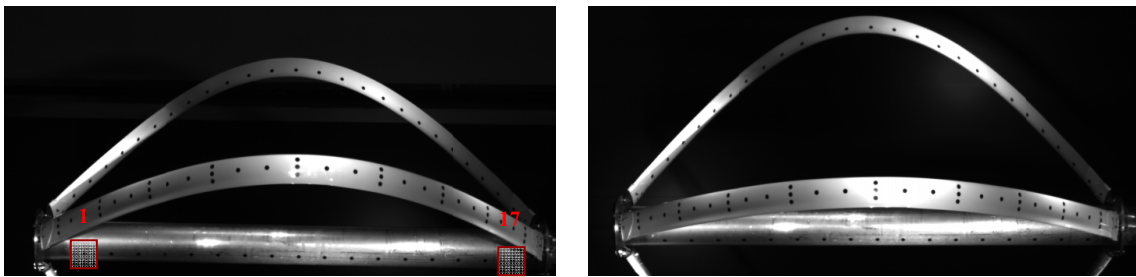


**Figure 4.9:** Left and right images at time  $t = 0$  .

To derive displacement time series from the stereo vision camera system, the following image processing algorithm was implemented in several steps:

- 1- Dividing each image into sub windows where each window contains a paper marker. The window size on each of the turbine components (rotor shaft and blades) depends on the way that the markers are arranged on different parts of the rotor (rotor components), the component geometry in the image and the expected movement of that component. Figure 4.10 shows the windows on the rotor shaft.

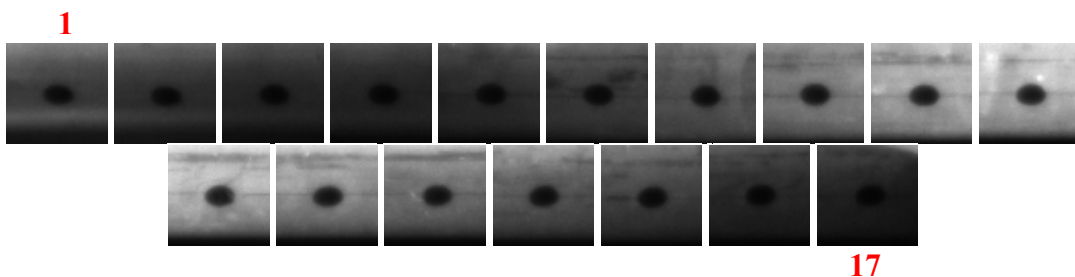


**Figure 4.10:** Image windows on the rotor shaft

- 2- Binarizing the windows with a certain threshold. This threshold is equal to the mean intensity of the image window multiplied by a coefficient. This coefficient, which is less than 1, depends on the image window contrast and obtains higher values for less contrast. On the other hand, each pixel in a grayscale image has an intensity value between 0 (black colour) and 1 (black

colour) and binarizing the image with a particular threshold means replacing all the intensity values above the threshold with 1 and others with 0.

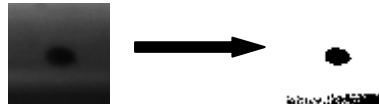


**Figure 4.11:** Binarizing the image window

- 3- Making the image negative (interchange the pixel intensities from black to white and vice versa) to get more intensity concentration at the marker's position and edge constraint.

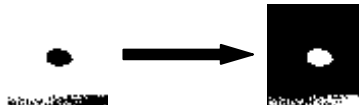


**Figure 4.12:** Negative image window

- 4- Pick up the features in the image window with a particular size:  $a_1 \leq N \leq a_2$  ( $N$  = number of pixels,  $a_1$  = minimum size of the considered feature in pixels,  $a_2$  = maximum size of the considered feature in pixels)

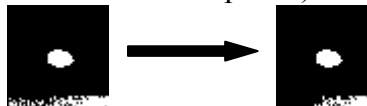


**Figure 4.13:** Sizing boundaries

- 5- Removing features that are adjacent to the border and take the most circular feature.

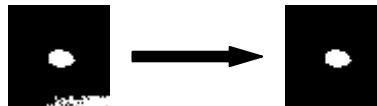


**Figure 4.14:** Removing features attached to the boundary and take the final circular feature

- 6- The centre of the circular feature from the last step of the image processing will be estimated as the intensity centroid of the image window. Due to the perspective projection, the image of the circular marker is distorted in the image plane and the centre of the circular feature is not the same as the image of the centre of the circular marker [1]. The image of a circle is usually deviated to an ellipse in the image plane depending on the angle and distance between the object and the image plane; thus, the centre of the circular feature as the centre of the marker is biased and should be corrected.

### 4.4.1 Perspective correction

When the objects in the real world are projected on the image plane, the perspective projection does not preserve the original shape of the object if it is not in the parallel plane with the image plane [1]. For instance, a circle in the real world will change to an ellipse after projection into the image plane. The centre of the ellipse, which can be estimated as the ellipse centroid, is not coincident with the image of the circle centre, and this error should be corrected. This problem has been addressed in detail in [1] and will be discussed briefly in this section.

The rays coming from the circular object  $\Gamma_1$  on the plane  $\Pi_1$  and going to the camera centre of projection  $O$  make a skewed cone that intersects the image plane  $\Pi_2$  in an ellipse  $\Gamma_2$ .

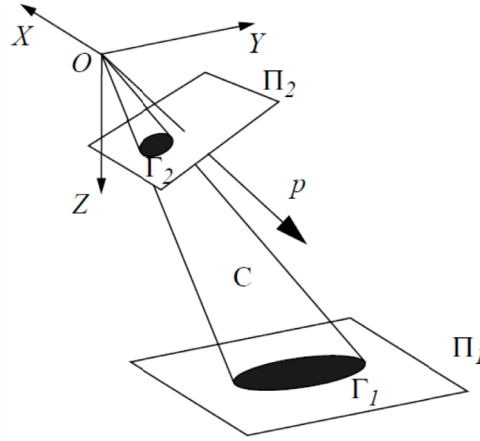


**Figure 4.15:** Projection of a circle on the image plane.  $\Omega_1(X, Y, Z)$  is the coordinate system of the circle plane centred in the camera projection centre, and  $\Omega_2(x, y, z)$  is the coordinate system of the camera reference frame such that  $x$  and  $y$  are parallel to the image coordinate system and  $z$  is orthogonal to image plane  $\Pi_2$ .

The equation of cone  $C$  is:

$$(X - \alpha Z)^2 + (Y - \beta Z)^2 = \gamma^2 Z^2 \tag{4.1}$$

where  $\alpha$  and  $\beta$  are the cone skewness in  $X$  and  $Y$  directions, and if  $d$  is the distance between the object and  $O$ , the circle equation will be:

$$(X - \alpha d)^2 + (Y - \beta d)^2 = \gamma^2 d^2 \tag{4.2}$$

As the centre of both coordinate systems are the same, the transformation between  $\Omega_1$  and  $\Omega_2$  is only a rotation:

$$\begin{pmatrix} X \\ Y \\ Z \end{pmatrix} = \underbrace{\begin{pmatrix} b_{11} & b_{12} & b_{13} \\ b_{21} & b_{22} & b_{23} \\ b_{31} & b_{32} & b_{33} \end{pmatrix}}_{BB} \begin{pmatrix} x \\ y \\ z \end{pmatrix} \quad (4.3)$$

Now, if the equation (4.1) is written in  $\Omega_2$  coordinates using equation (4.3), the intersection of the cone equation in  $\Omega_2$  and  $\Gamma_2$  is:

$$\begin{aligned} & (n^2 + k^2 - r^2)x^2 + 2(kl + np - rs)xy + (l^2 + p^2 - s^2)y^2 \\ & + 2(km + nq - rt)x + 2(lm + pq - st)y + m^2 + q^2 - t^2 = 0 \end{aligned} \quad (4.4)$$

where

$$\begin{aligned} r &= \gamma b_{13} & k &= b_{11} - tb_{31} & n &= b_{21} - tb_{31} \\ s &= \gamma b_{32} & l &= b_{12} - tb_{32} & p &= b_{22} - tb_{32} \\ t &= \gamma b_{33}f & m &= (b_{13} - tb_{33})f & q &= (b_{23} - tb_{33})f \end{aligned}$$

Equation (4.4) is a quadratic curve like circle, ellipse and parabola. In the current case, it is an ellipse with a centre of  $(u_c, v_c)$  :

$$\begin{aligned} u_c &= \frac{(kp - nl)(lq - pm) - (ks - lr)(tl - ms) - (ns - pr)(tp - qs)}{(kp - nl)^2 - (ks - lr)^2 - (ns - pr)^2} \\ v_c &= \frac{(kp - nl)(mn - kq) - (ks - lr)(mr - kt) - (ns - pr)(qr - nt)}{(kp - nl)^2 - (ks - lr)^2 - (ns - pr)^2} \end{aligned} \quad (4.5)$$

To find the image of the circle centre, the radial of the circle is assumed to be zero,  $\gamma = 0$ . Then,  $r, s$  and  $t$  become zero and the projection of the circle centre will be:

$$\begin{aligned} u_c &= \frac{(lq - pm)}{(kp - nl)} \\ v_c &= \frac{(mn - kq)}{(kp - nl)} \end{aligned} \quad (4.6)$$

The last step of the image processing algorithm has estimated the ellipse centre. To find the location of the circle centre, the ellipse centre should be corrected by adding the following values to the coordinates [2]:



$$\begin{aligned} e_x &= u_c - u_0 \\ e_y &= v_c - v_0 \end{aligned} \quad (4.7)$$

For calculating the centre of the circular markers in the current case, the plane of each of the markers should be estimated. The markers on the rotor shaft are on the same plane as the calibration plane; thus, the rotation matrix  $BB$  is the same as the rotation matrix  $R$  obtained from the calibration. The rotation matrix  $BB$  for the markers on the blade should be estimated using the relative positions of the blades relative to the calibration plane. Each of the blades has rotated around the  $x$  and  $y$  axes in respect to the calibration plane with a particular angle. The angle around the  $x$  axis is defined as the angle between the normal vector to the calibration plane and the surface passing through all the markers on the blade. In addition, the plane of each marker is rotated around the  $y$  axis with respect to the blade curvature and estimated using the blade slope at that point. Finally, the rotation matrix  $BB$  is obtained for each of the markers by subtracting the resultant angles from the calibration angles.

After having the position of the marker centre in the entire image frame of the left and right camera, the line passing through each of the camera centres and the real marker centre is obtained. Using stereo triangulation (chapter 1), the 3D coordinate of the marker centre in time is calculated.

Finally, for each point, three time series in three coordinates are obtained, as shown in Figure 4.16.

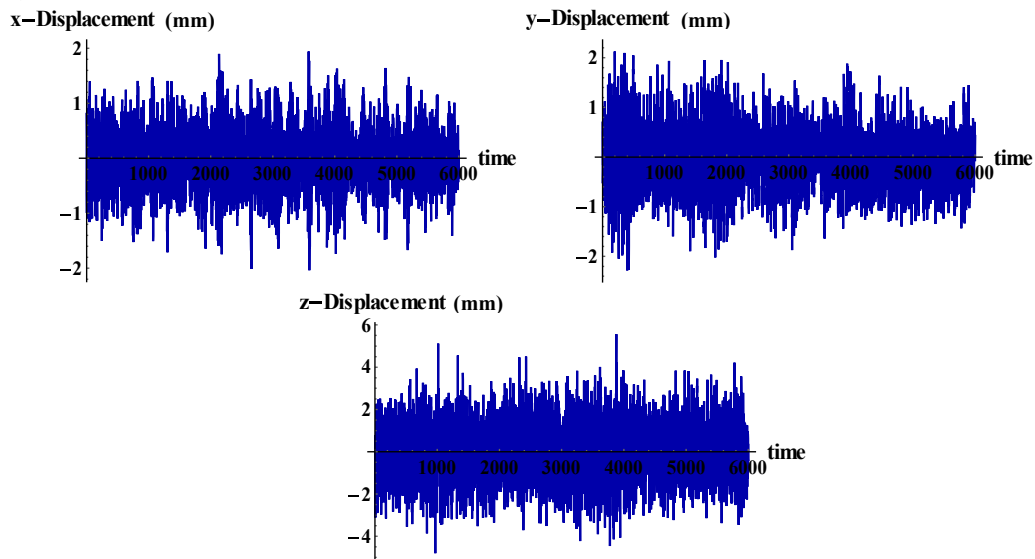


**Figure 4.16:** Displacement time series for one of the rotor shaft points in  $x$ ,  $y$  and  $z$  directions: each of the intervals on the time axis is equal to 1 time step  $= \frac{1}{187}$  s, the displacement is presented in mm.

## 4.5 DD-SSI analysis

DD-SSI can efficiently identify the modal properties of the linear multivariate structures. After the publishing of the DD-SSI algorithm in the book by van Overschee and De Moor in 1996 [3], it has been accepted as a strong and efficient tool for output only modal analysis. In this method, the accurate state space models for multivariate linear systems are made directly from the measured data with easy parameterization and good convergence, and no need to solve the highly nonlinear optimizations problem associated with the auto-regressive moving average method (ARMA) [4].

In DD-SSI, the projection matrix is calculated using the Hankel matrix of the measurement data. The projection and covariance matrices are closely related, but in the covariance matrix, the error and noise may be squared up by the covariance estimation [5]. For calculating the projection matrix, efficient methods have been established using numerically robust squared root algorithms like QR-factorization [6]. Therefore, theoretically, the numerical behaviour of DD-SSI is better than that of COV-SSI [7].

The DD-SSI code is written according to the algorithm introduced by Overschee and De Moor in 1996. This code will be validated in the following sections using a solved analytical example of a simple beam from Rao Book [8] (Analytical validation) and a realistic beam with an airfoil profile that has random input and more complications (Numerical validation).

### 4.5.1 Analytical validation of the DD-SSI code

In this section, the displacement response of a uniform simply supported copper beam subjected to a step-function force  $F_0$  at  $x = \xi$  and corresponding boundary conditions is found in 21 places on the beam as 21 time series.

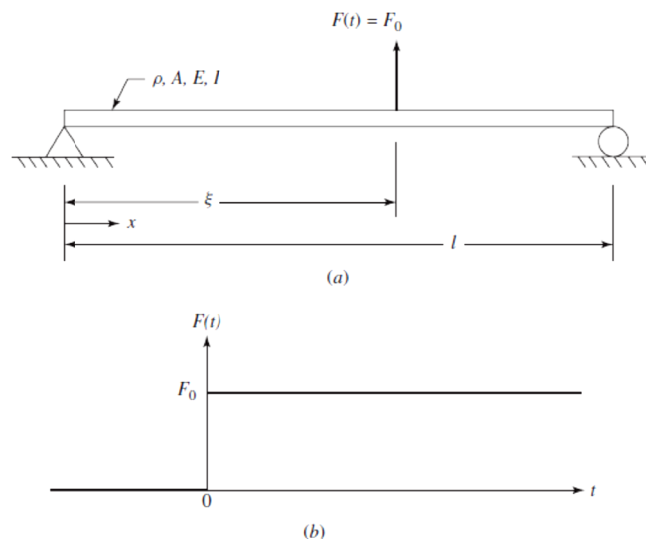


**Figure 4.17:** Copper beam subjected to a step-function force [8]



The natural frequencies and mode shapes are [8]:

$$\omega_i = \frac{i^2 \pi^2}{l^2} \sqrt{\frac{EI}{\rho A}}$$

$$W_i(x) = \sqrt{\frac{2}{\rho A l}} \sin \frac{i\pi x}{l}$$
(4.8)

For  $F_0 = 20N$  and  $E = 120 GPa$ , beam section of  $4cm \times 1.5cm$ , length of  $l = 65cm$  and  $\xi = 0.9l$ , the response of the beam is given by [8]:

$$w(x, t) = \frac{2F_0 l^3}{\pi^4 EI} \sum_{i=1}^{\infty} \frac{1}{i^4} \sin \frac{i\pi x}{l} \sin \frac{i\pi \xi}{l} (1 - \cos \omega_i t)$$
(4.9)

where  $i$  is the mode number. The transverse displacement time series are calculated in 21 points of the beam as the response to  $F_0$  acts at  $\xi$ . These points are placed with intervals of  $\frac{l}{20}$  in 10 s with time steps of 1 ms. The output signal has been generated using the first 20 natural frequencies:

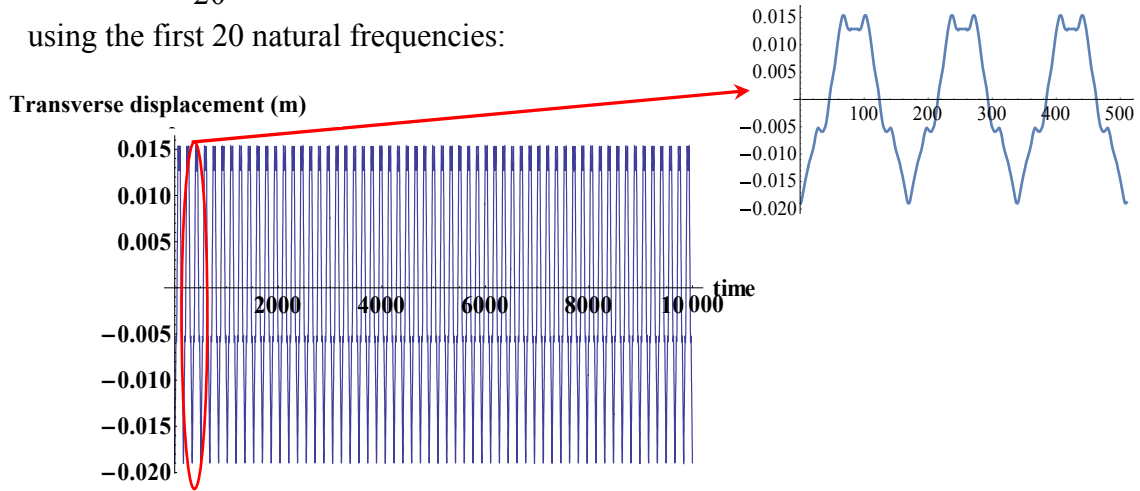


**Figure 4.18:** Transverse displacement of a point on the beam at  $x = \frac{17}{20}l$  subtracted by its mean value (each of the intervals on the time axis is equal to 1 time step =  $\frac{1}{1000}$  s)

The beam response in 21 points as 21 time series is the input for the DD-SSI code; thus, the number of channels is  $n_c = 21$ . After modal identification the stability diagram is plotted as shown in Figure 4.19.

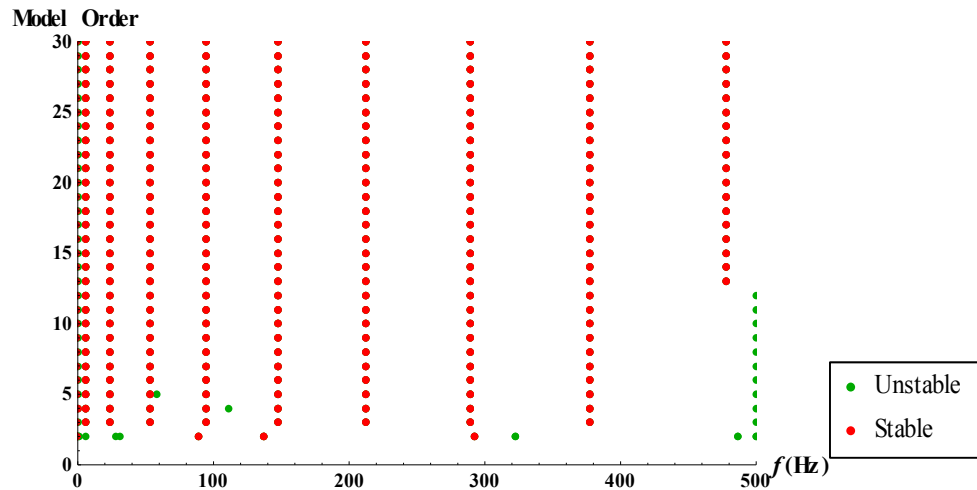


**Figure 4.19:** Stability diagram of the beam response to the step function force

As shown in the following table, the natural frequencies and mode shapes from analytical solution and the DD-SSI algorithm are identical.

**Table 4.1:** natural frequencies and mode shapes from analytical solution and DD-SSI

Analytical natural frequency (Hz)	DD-SSI natural frequency (Hz)	Mode shape form Analytical Approach and DD-SSI
5.90	5.90	
23.60	23.60	
53.10	53.10	
94.41	94.41	
147.51	147.51	
212.42	212.42	
289.12	289.12	
377.63	377.63	
477.94	477.94	

## 4.5.2 Numerical validation of the DD-SSI code

In this section, a 2-*m*-long cantilever beam with an airfoil profile made from Aluminium is modelled using HAWC2. HAWC2 is an aeroelastic code developed at Risø DTU since 2003. In the structural part of this code, each structure is divided into multiple bodies and each body is simulated using the finite element method (FEM) based on the Timoshenko beam theory [9]. The HAWC2 code enables the calculation of the response of the structure in the time domain using the Newmark algorithm. Newmark is an integration procedure that uses the state vector in the previous time as well as the load vector in the previous and current times to build up the state vector in the current time. Detailed information about this algorithm can be found in [10].

The beam is modelled as a one body structure subjected to a random force distribution all over the beam to satisfy the requirement for an operational modal test. The response of the beam in the time domain is simulated with time intervals of 0.0005 *s* (5 *ms*) for 10 *s*, as shown in Figure 4.20.

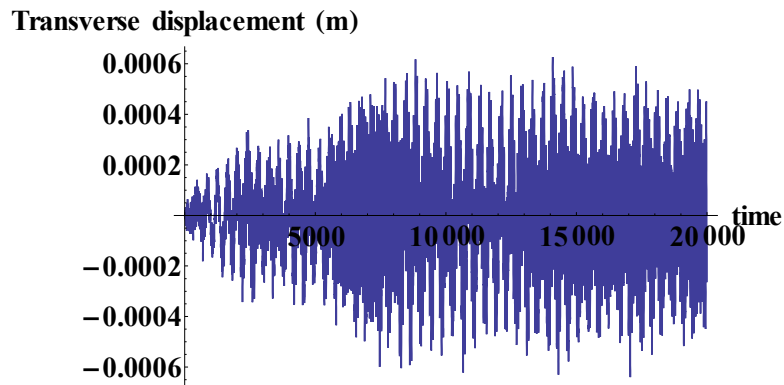


**Figure 4.20:** Transverse displacement of the tip point of the beam subtracted by its mean value (each of the intervals on the time axis is equal to 1 time step = 0.0005 *s*)

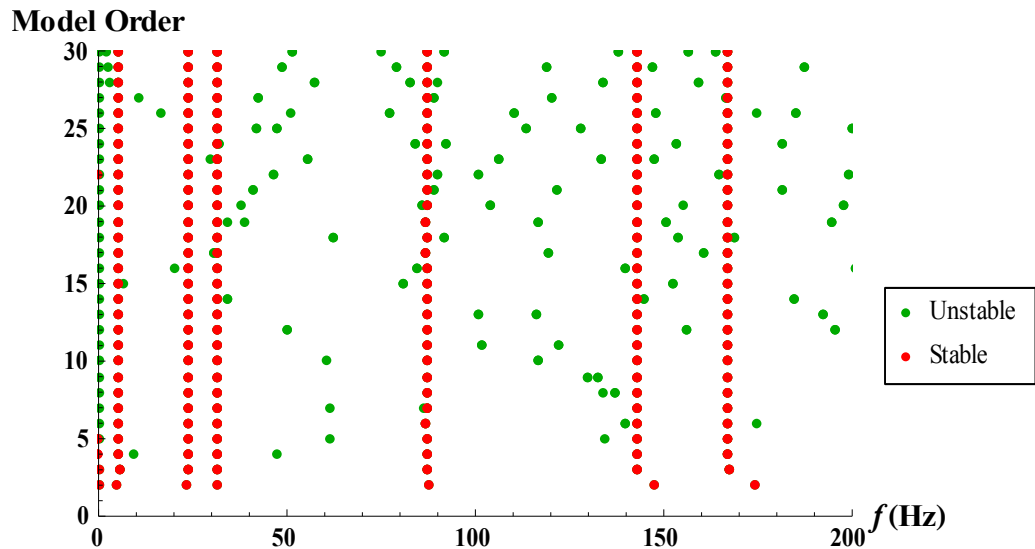
The time series of displacement of 11 points on the blade in three directions will be the input of the DD-SSI. Thus,  $n_c = 3 \times 11 = 33$ .

Regarding the HAWC2 manual [9], the Newmark algorithm is used to produce the response time series. The error of the predicted frequency from the simulated time series is:

$$\frac{\Delta f}{f} = -\frac{1}{12}(\omega h)^2 \quad (4.10)$$

where  $\omega$  is the predicted frequency in *rad*/sec and  $h$  is the sampling time interval. According to this error, the estimated frequencies from the time series are reliable until

$\frac{1}{10}$  sampling frequency. Therefore, the stability diagram is plotted for a frequency range of 0–200 Hz, which is shown in Figure 4.21.

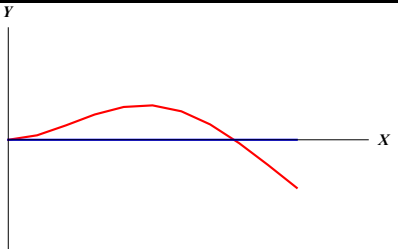
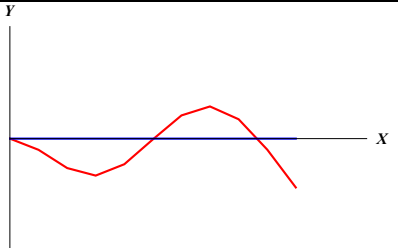
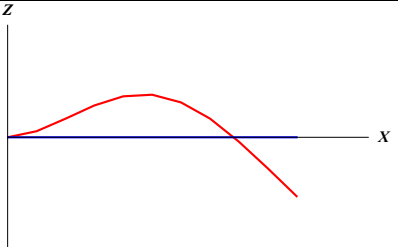
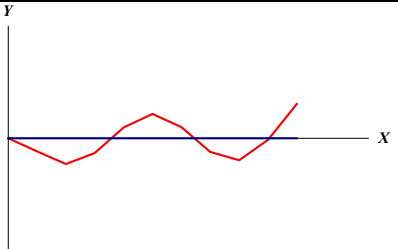


**Figure 4.21:** Stability diagram of the simulated cantilever beam response to the random loading

In the modelling of the beam, no damping is considered. Then, the unstable poles in the stability plots have non-negligible damping ratio or MAC number less than 0.8. After correcting the natural frequencies from DD-SSI using equation (4.10), they are compared with the frequencies from the FEM.

**Table 4.2:** Natural frequencies and mode shapes from FEM and DD-SSI

FEM natural frequency (Hz)	DD-SSI natural frequency (Hz)	Mode shape form DD-SSI
5.00	4.99	
23.68	23.66	

31.30	31.29	
87.53	87.52	
145.61	145.42	
171.33	170.91	

As is obvious from Table 4.2, the natural frequencies from the numerical solution and DD-SSI agree very well. The mode shapes are identical for both DD-SSI and FEM.

### 4.5.3 DD-SSI results

As has been mentioned before, because of the hardware and software limitations, the rotor shaft and two blades can be monitored for 32 s (6000 time steps). Hence, the number of channels will be  $n_c = 67 \times 3 = 201$  (without considering horizontally spaced markers<sup>1</sup>). The number of columns in the Hankel matrix  $j = N - 2i + 1$  should be larger than the number of rows  $2n_c i$  [3]. By having 201 measurement channels, the maximum model order reaches to 14, which is a rather small value for modal identification. On the other hand the large number of measurement channels decreases the performance of the

<sup>1</sup> SSI analysis is also conducted with horizontally spaced markers to investigate the torsional behaviour; however, no torsional mode was detected. Therefore, they are removed from the next analysis.

DD-SSI. Therefore, the measurement points are picked every second to reduce  $n_c$  to  $3 \times 35 = 105$ .

Each block in the Hankel matrix is a vector containing the measurement of 105 channels in a particular time step of  $k$  :

$$y_k = \begin{pmatrix} x_{11} \\ x_{21} \\ \vdots \\ x_{n_c k} \\ y_{11} \\ y_{21} \\ \vdots \\ y_{n_c k} \\ z_{11} \\ z_{21} \\ \vdots \\ z_{n_c k} \end{pmatrix}$$

Where where  $x_{n_c k}$ ,  $y_{n_c k}$  and  $z_{n_c k}$  are the displacements of point  $n_c$  in  $x$ ,  $y$  and  $z$  coordinates, respectively, and  $y_k$  is the block of measured data in time step of  $k$ . The displacement is the position of the point subtracted from the mean value of the position during the measurement period.

After gathering all the measurement data in the Hankel matrix, DD-SSI is implemented for model order until 28 and the modal parameters are identified for all the model orders. The stability plot is shown in Figure 4.22.

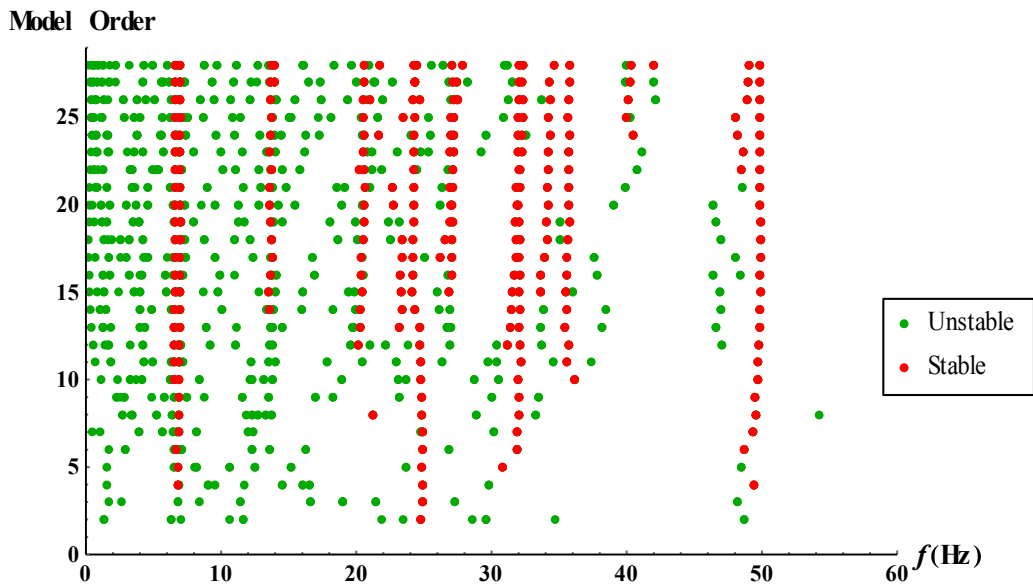


**Figure 4.22:** Stability plot of the parked VAWT rotor response to the wind loading

The stable poles in the stability plot have damping ratios higher than 0.04 and MAC number higher than 0.8. The mode shapes show that some green lines in the stability diagram (we call them frequency lines hereafter in this text), which contain stable poles, are not structural modes. On the other hand some of the frequencies are related to the effect of the guy wires (which connect the structure under the rotor to the floor) and the flow around the VAWT. The structural modes and the additional effects of the guy wire interactions as well as the frequencies induced by the flow are discussed in the following sections.

## 4.6 Structural modes

### 4.6.1 HAWC2 simulation

As it has been mentioned, one of the blades has not been captured with the two cameras in the images; hence, its behaviour cannot be directly seen in the images, although the influence with the two other blades is present. In addition, all the frequency lines in the stability diagram are not related to the structural modes, and they need to be characterized and separated from the structural modes. Therefore, a HAWC2 simulation is conducted to predict the structural modes without considering aerodynamics. Vita has modelled a two bladed offshore VAWT via HAWC2 [11]. He used a multibody formulation in HAWC2 to simulate the VAWT as a composition of several bodies, where each body was modelled with the Timoshenko beam formulation. For more detailed information about the VAWT model refer to [11].

In the current study, Vita's model [11] has been updated for the 3-bladed onshore VAWT. Since there was no exact information available about the red box connected to the rotor and the shaft under it<sup>1</sup>, the entire structure under the rotor is simplified as a long shaft connecting the rotor to the floor. The structural mode shapes are predicted using eigensolver with no damping included.

**Table 4.3:** VAWT rotor natural frequencies obtained by the HAWC2 simulation

Mode No.	Frequency (Hz)
1	6.86
2	6.86
3	23.09
4	23.09
5	23.11
6	31.60
7	33.33
8	50.99

<sup>1</sup> Due to time constraints with the Milan wind tunnel, we could not provide the stiffness and damping data of the support and rotor system via a decay test

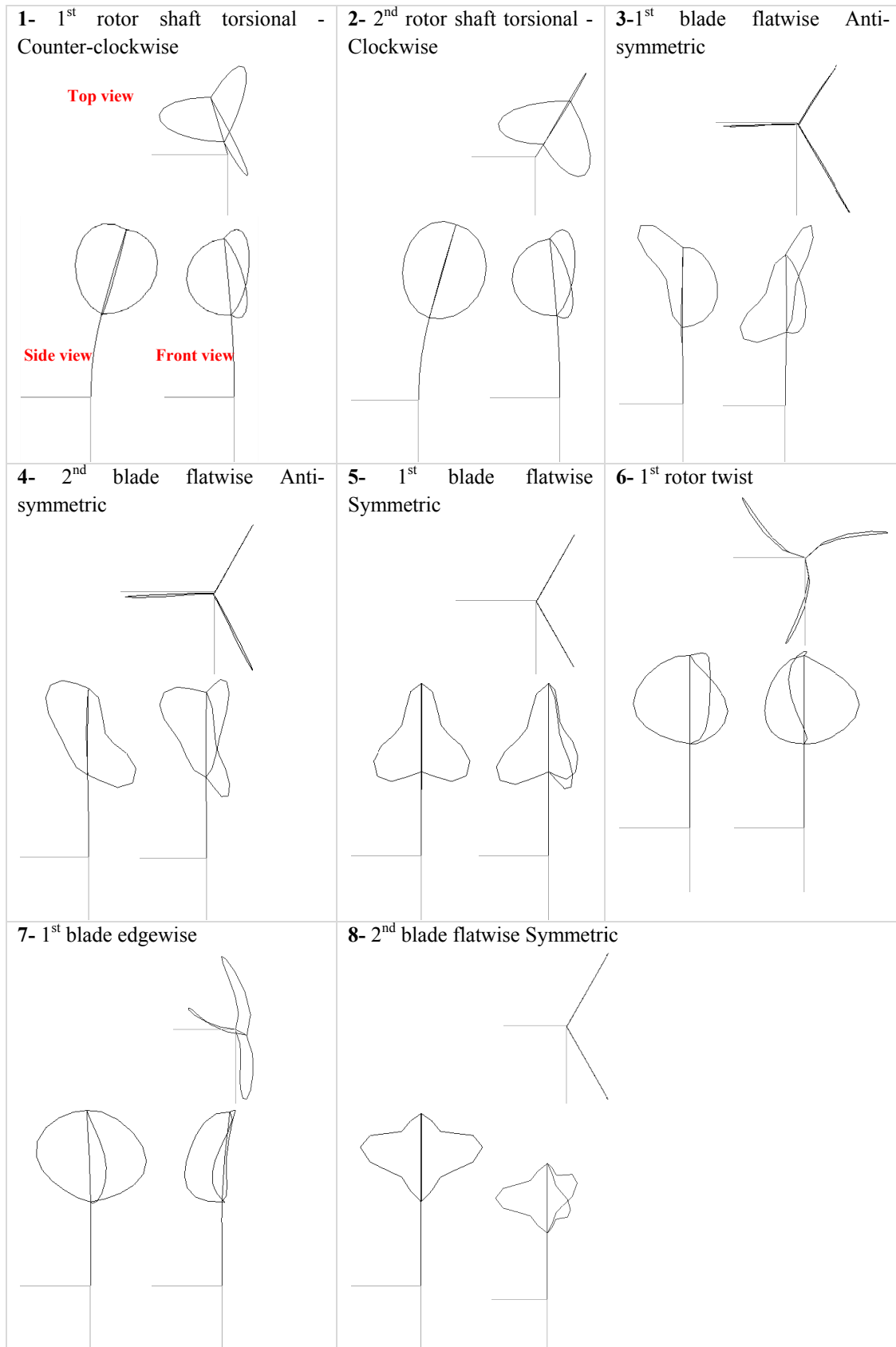


**Figure 4.23:** VAWT rotor mode shaped obtained by HAWC2 simulations



The natural frequencies and mode shapes in the wind tunnel experiment are expected to be different from the simulation results because of the aerodynamics and simplifications in the simulation. These differences will be explained in the next section.

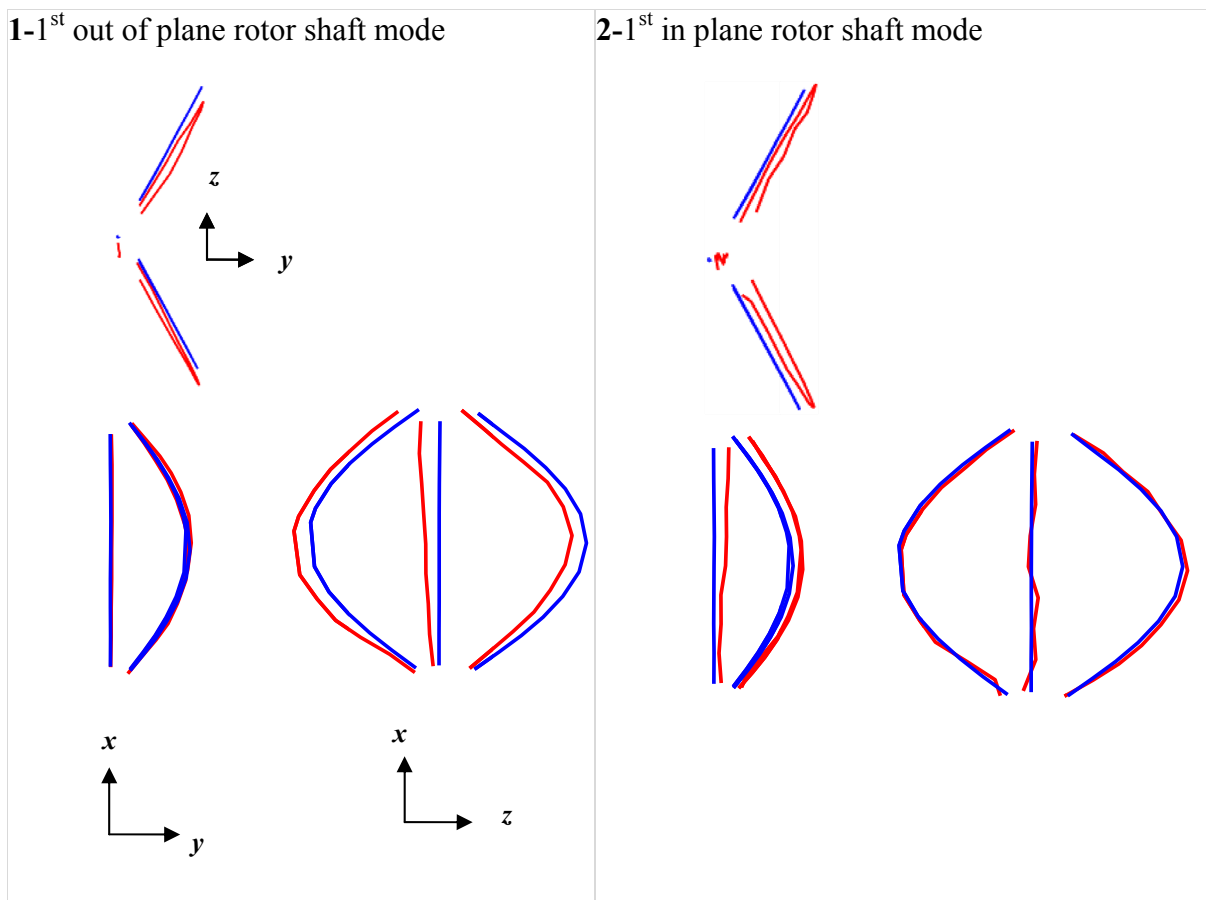
## 4.6.2 Wind tunnel experiment

The modal parameters of the structural modes derived via DD-SSI are summarized in the following table.

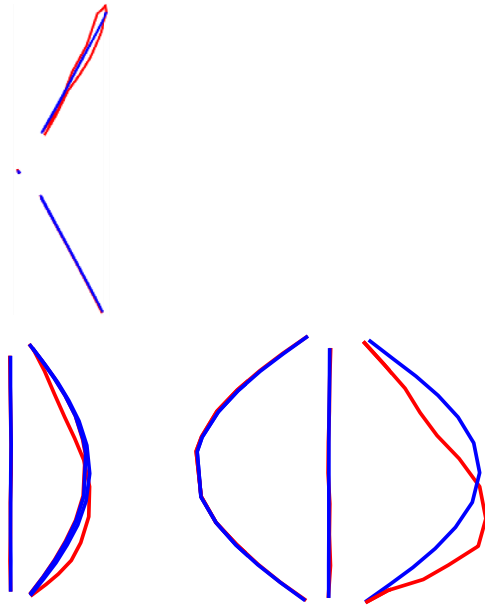
**Table 4.4:** Natural frequencies and damping ratios of structural modes from DD-SSI

Mode No.	Frequency	$\sigma_f$	$\epsilon_f$	Damping ratio	$\sigma_\zeta$	$\epsilon_\zeta$
1	6.55	0.037	0.0009	0.012	0.012	0.158
2	6.93	0.032	0.0007	0.010	0.003	0.049
3	24.49	0.300	0.0017	0.012	0.003	0.040
4	27.16	0.172	0.0017	0.018	0.008	0.128
5	32.04	0.281	0.002	0.009	0.003	0.082
6	31.83	0.304	0.002	0.014	0.008	0.142
7	49.72	0.271	0.0007	0.015	0.009	0.083

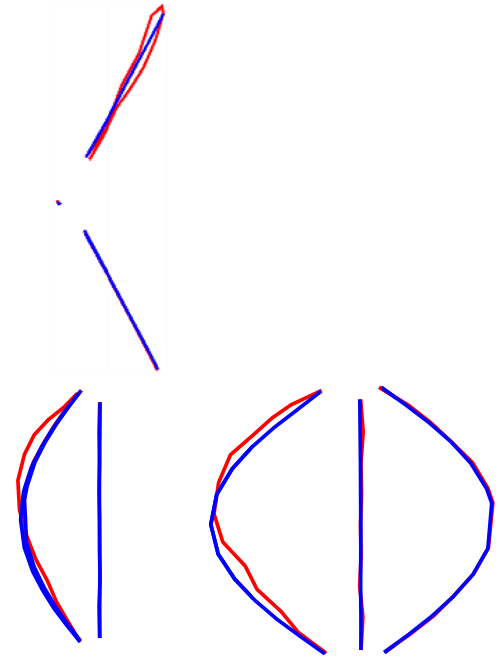
The following figure shows the corresponding mode shapes:



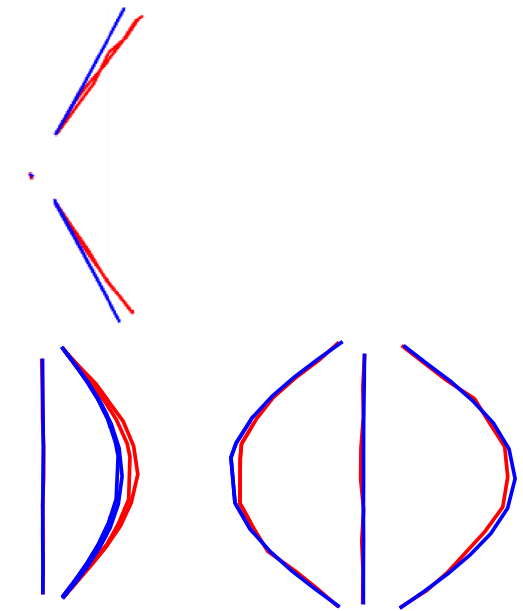
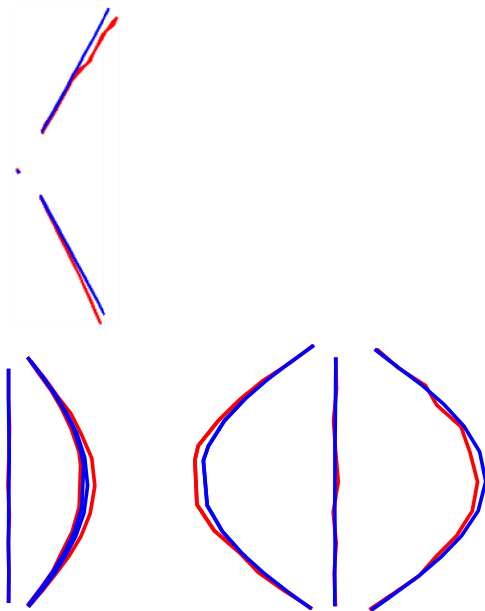
3-1<sup>st</sup> blade flatwise mode (with a small edgewise motion)



4-2<sup>nd</sup> blade flatwise mode (with a small edgewise motion)



5-1<sup>st</sup> purely edgewise blade mode rotor twist 6-2<sup>nd</sup> purely edgewise blade mode



7-3<sup>rd</sup> blade flatwise mode (with a small edgewise motion)

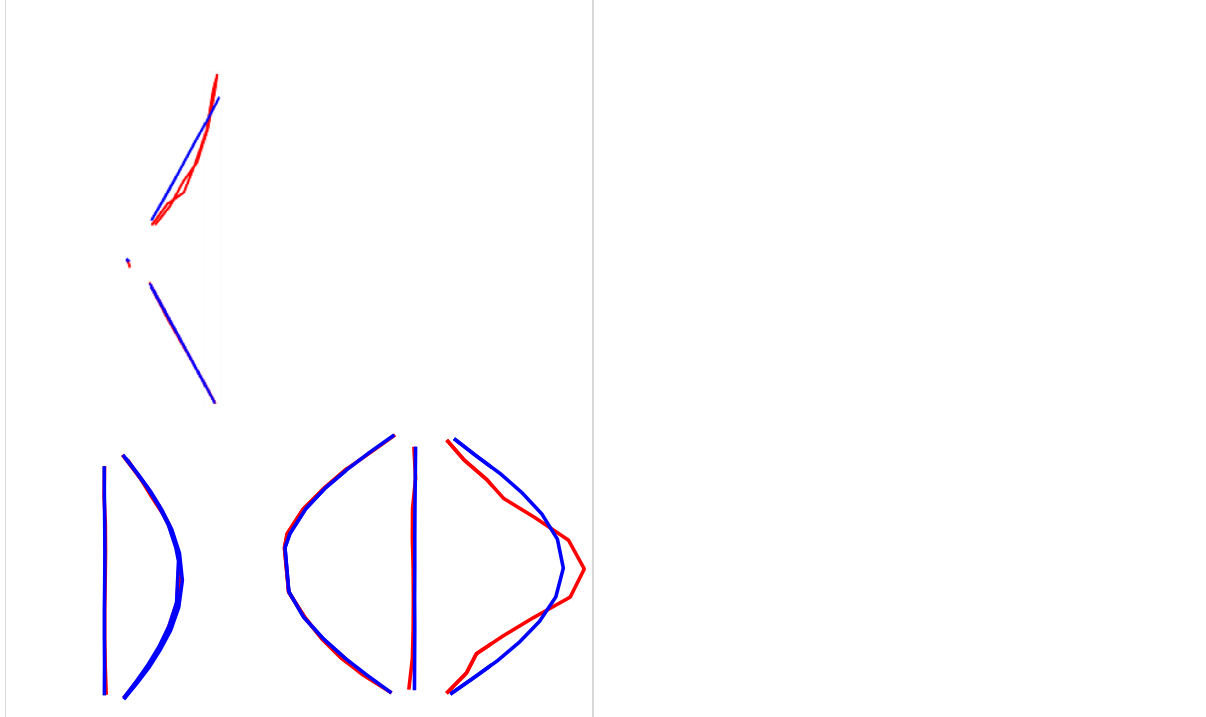


**Figure 4.24:** Structural mode shapes of VAWT rotor in wind tunnel (**Blue:** initial rotor shape, **Red:** rotor mode shape)

As is obvious from Figure 4.24, the first natural frequency is the first rotor shaft mode. In this mode, the rotor shaft is moving in depth ( $z$  direction). As the turbine has three blades, the in plane mode is when the rotor moves in the calibration plane and out of plane mode is when the rotor moves out of the calibration board. In the first frequency, the rotor shaft moves out of the calibration plane. In the next rotor shaft mode, the rotor shaft moves in the main wind direction ( $y$  direction) and in the calibration plane. The rotor shaft natural frequencies, obtained from the experiment, are close to the simulation results. However, the mode shapes are different because of the aerodynamic effect induced by the wind direction, since the wind induces forces to the turbine structure in parallel and perpendicular to the wind direction; this leads to rotor shaft modes in those two directions.

The third and fourth modes are the blade modes. As the third blade has not been captured in the images, the mode shapes that the two other blades are involved in look identical. These modes contain a larger flatwise and a smaller edgewise motion of one of the blades captured in the images and the other blade in the image does not move. Since each of the three turbine blades experiences different angles of attack, the blades must experience different wind loadings and, consequently, different aerodynamic damping; hence, the blades exhibit different modal behaviour.

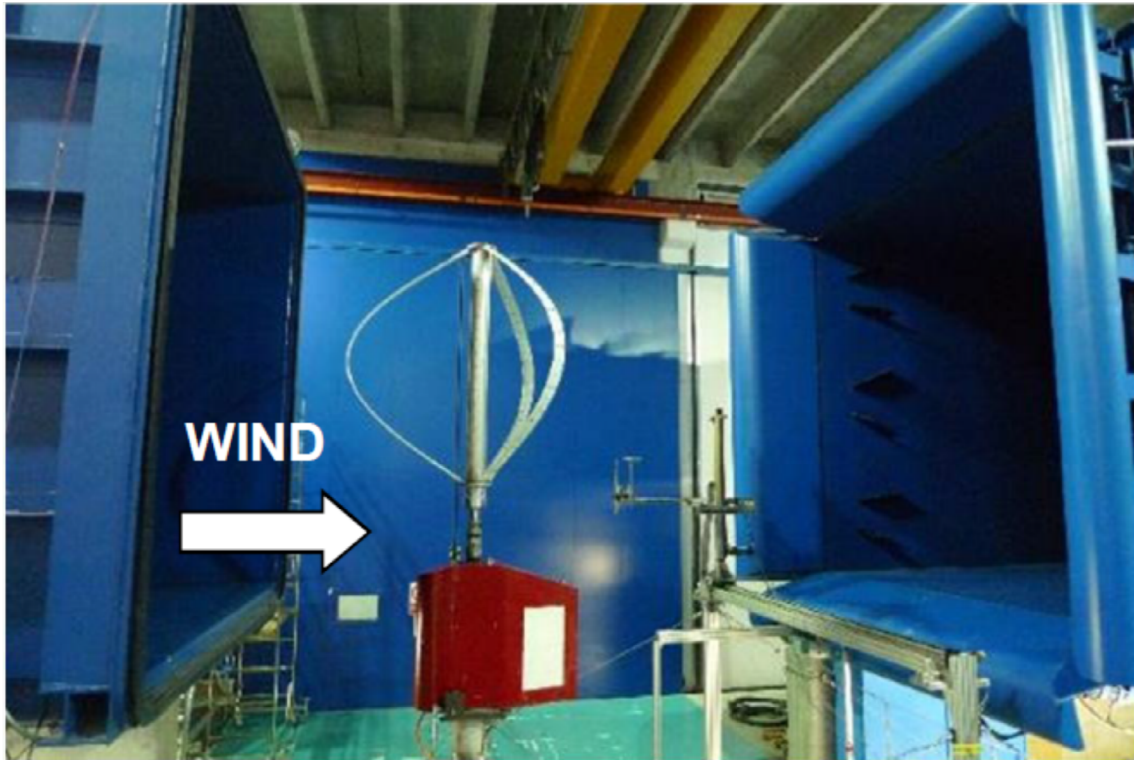


**Figure 4.25:** The blades experience different angle of attacks with respect to the wind direction

In the simulated blade flatwise modes, all the three blades with identical loading, material properties and the boundary conditions contribute and make three flatwise modes; however, in the wind tunnel experiment, one of the blades does not move in the modes with the strong flatwise motion. Therefore, there are two blade flatwise modes. To investigate the difference between the simulated and experimental blade flatwise modes, the aerodynamic loading on each of the blades is studied according to their angles of attack.

The blade airfoil is DU06-W-200, which is an asymmetric improved version of NACA 0018 with better performance [12].

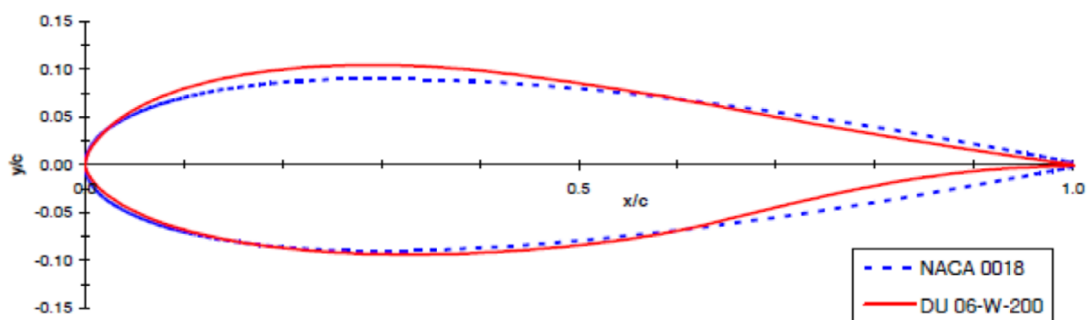


**Figure 4.26:** Shape of DU06-W-200 and NACA 0018[12]

The drag and lift coefficient are estimated over larger angles of attack using the following equations:

$$\begin{aligned} C_l(\alpha) &= k_1 \sin 2\alpha \\ C_d(\alpha) &= C_{d0} + k_2 \sin^2 \alpha \end{aligned} \quad (4.11)$$

where  $k_1 = 1$ ,  $k_2 = 0.75$  and  $C_{d0} = 0.015$ . Using equation (4.11)  $C_l$  and  $C_d$  can be plotted versus the angle of attack.

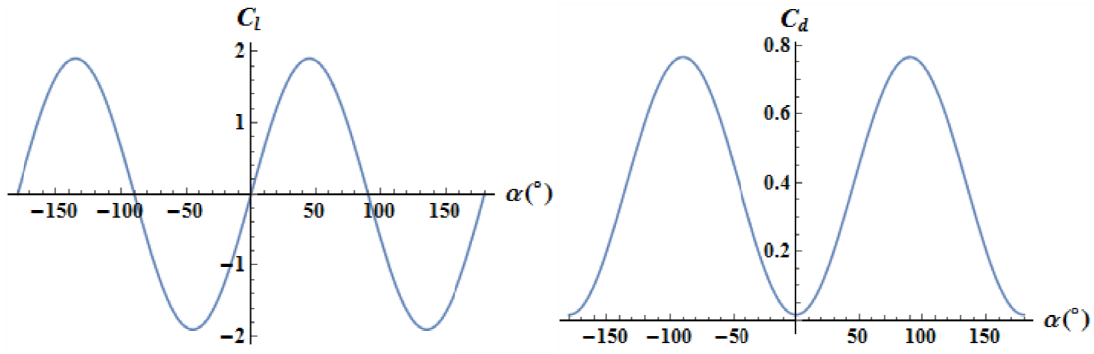


**Figure 4.27:** Approximated DU06-W-200 lift and drag coefficient over angles of attack  $-180^\circ$  to  $+180^\circ$

The blades configuration in the wind tunnel, angles of attack and lift and drag forces are presented in Figure 4.28 and Table 4.5.

<sup>1</sup> The linear part of  $C_l$  with slope  $dC_l/d\alpha \approx \pi\alpha$  is not considered here.

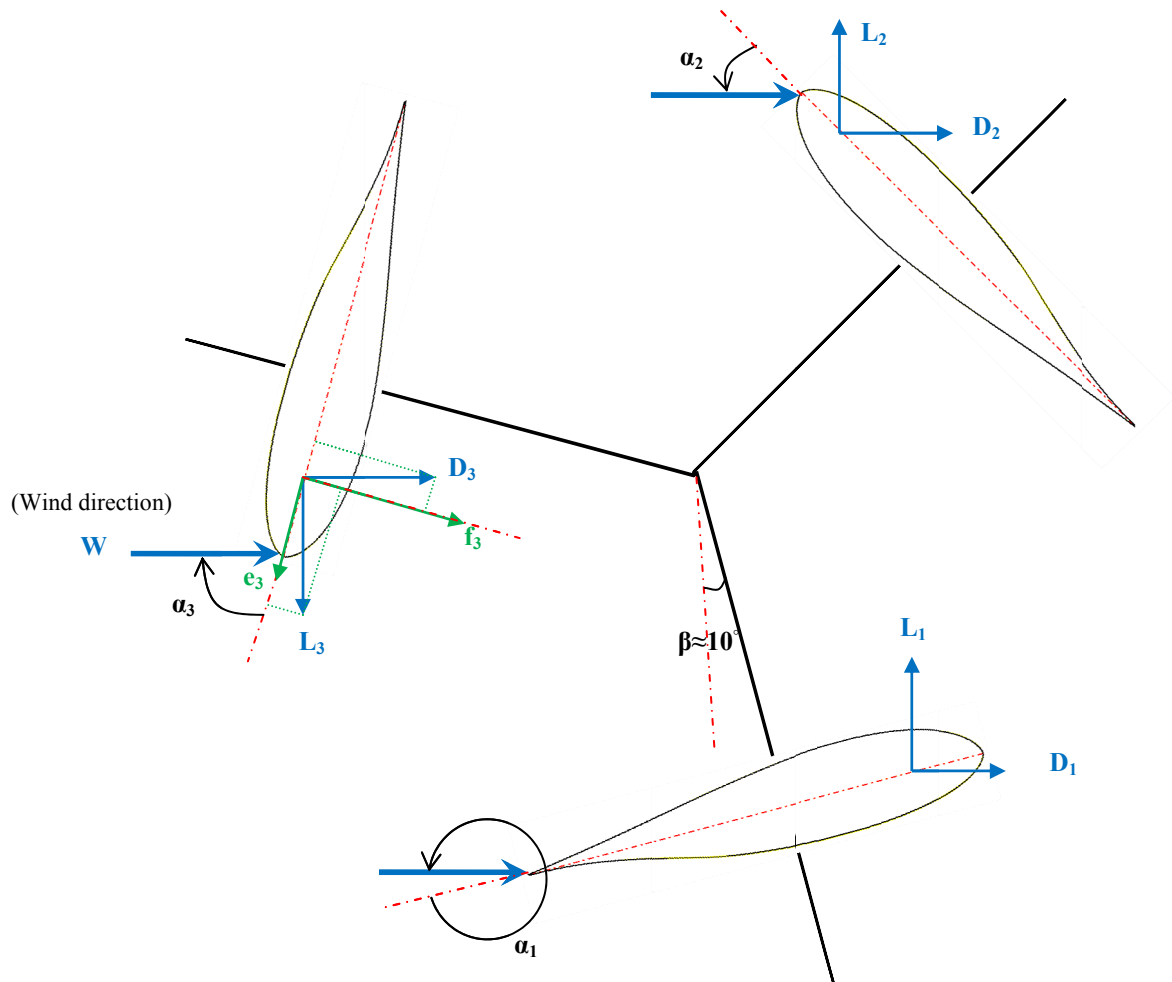


**Figure 4.28:** A representative section of the rotor blades configuration in the wind tunnel (lift and drag forces are just indicating the direction but not magnitude)

**Table 4.5:** Aerodynamic force on the blades during experiment

	Angle of attack	Lift force [N]	Drag force [N]	$f(\text{flatwise force})/e(\text{edgewise force})$
<b>Blade 1#</b>	$\alpha_1 = -170^\circ$	$L_1 = 149.26$	$D_1 = 8.64$	$f_1/e_1 = 4.23$
<b>Blade 2#</b>	$\alpha_2 = -50^\circ$	$L_2 = 429.77$	$D_2 = 104.53$	$f_2/e_2 = 1.35$
<b>Blade 3#</b>	$\alpha_3 = 80^\circ$	$L_3 = 280.52$	$D_3 = 155.56$	$f_3/e_3 = 1.15$

According to Figure 4.28 and Table 4.5, flatwise force over edgewise force ratio is much larger for the first blade than for the two other blades, i.e. the flatwise force for the first blade is four time larger than the edgewise force. The flatwise force is applied on the airfoil suction surface, which is assumed to lead to larger contribution of the aerodynamic damping in the flatwise modes of the first blade. The result indicates that the first blade is highly damped in flatwise motions due to the aerodynamic loads.

The difference between the third and the fourth modes is explained by the influence of the third blade having a similar shape with the second blade, in the sense of symmetric or anti-symmetric behaviour.

The fifth mode is a rotor twist such that the third blade is expected to have a similar behaviour to the others. The next mode is also the edgewise blade mode.

In the last identified structural mode, the second blade has more flatwise and less edgewise motion, which is more likely accompanied with a symmetric or anti-symmetric motion of the third blade. The first blade does not move in this mode as well because of the aerodynamic damping involved in the flatwise modes for the first blade.

As it was discussed in this section, because there were only two cameras, one of the blades was not captured in the pictures, and we had to guess its dynamic behaviour by studying the aerodynamics. However, the use of more cameras would reveal the dynamic interactions between the blades and rotor shaft with no assumption and predictions.

## 4.7 Guy wire effects

There are a number of frequency lines in the stability plot (Figure 4.22) that satisfy the requirement regarding MAC number and damping ratio of the stable modes, but there is no identified mode shape corresponding to them. On the other hand, some of the stable frequencies do not introduce a structural mode shape. The interesting point about these modes is that the frequencies are harmonics of the first frequency within 3.5%.

**Table 4.6:** Natural frequencies and damping ratios of guy wire modes from DD-SSI

Mode No.	Frequency (Hz)	$\sigma_f$	$\epsilon_f$	Damping ratio	$\sigma_\zeta$	$\epsilon_\zeta$
1	$f_1 = 6.95$	0.067	0.002	0.028	0.005	0.047
2	$2 \times f_1 \approx 13.64$	0.061	0.0008	0.018	0.007	0.072
3	$3 \times f_1 \approx 20.47$	0.133	0.001	0.018	0.006	0.054
4	$4 \times f_1 \approx 26.85$	0.287	0.003	0.028	0.009	0.110
5	$5 \times f_1 \approx 34.13$	0.269	0.001	0.016	0.005	0.060

To know what the source of these frequencies is, it is good to have a closer look on the turbine fixtures (Figure 4.29).



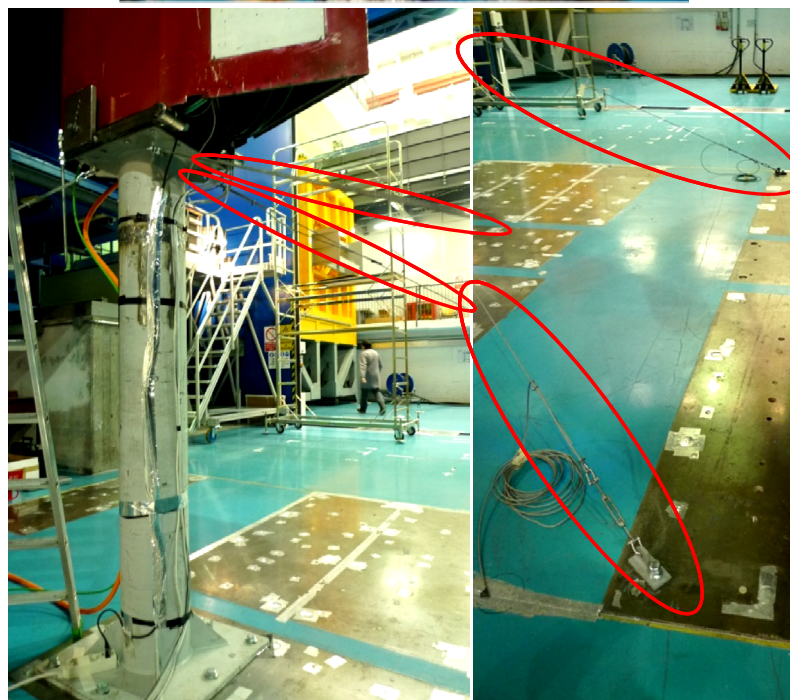


**Figure 4.29:** Guy wires connecting the shaft under the rotor to the ground

It can be seen in Figure 4.29 that four guy wires connect the shaft under the rotor to the floor to support the structure. The use of guy wires to support the structures has two main consequences. One of them consequences is the dynamic interference of the



structure with the cables [13]. The natural frequencies of the guy wires, which are excited by turbine movements, are:

$$f_n = \frac{n}{2L} \sqrt{\frac{T}{\rho A}} \quad (4.12)$$

where  $n$  is the mode number,  $L$  is the wire length,  $A$  is the cable cross sectional area,  $T$  is the guy wire tension and  $\rho$  is the density of the guy wire.

The guy wires in this experiment are from stainless steel with a length of 3400 mm and a diameter of 5 mm. Unfortunately, a fixed time allowance in the wind tunnel restrained us from performing the particular exercise of measuring the tension in the cable before and after the experiment (footnote 1 page 76). Accordingly, the guy wire frequencies and the interference with the other parts cannot be directly estimated from equation (4.12). However, equation (4.12) indicates that the guy wire eigenfrequencies are the multiple of the first frequencies; thus, it could be concluded that the mentioned frequencies in Table 4.6 are induced by the guy wires to the rotor structure.

An interesting point about the current guy wire modes is the modal damping ratios. The damping ratio of the cables is expected to be low (less than 0.002) [13], but the modal damping ratios obtained in the current experiment are about 10 time larger than this value. To investigate this case, the guy wire tension  $T$ , which is an important factor in the damping of the cables, is calculated using equation (4.12) and by knowing the cable properties and natural frequencies,  $T = 351 \text{ N}$ . This value is relatively low compared with that in other references [13-15]. According to [14], a decrease in the wire tension induces an increase in damping. Therefore, the high modal damping ratios of the cables obtained in wind tunnel experiment can be caused by the low tension in the guy wires.

## 4.8 Induced vortex shedding frequency

When the flow around a body is separated due to the viscosity and high Reynolds number, the low pressures vortices start to shed either past or through the side of the body. This vortex shedding oscillation occurs in a particular frequency that is introduced in the form of a dimensionless variable called Strouhal number ( $St$ ), which depends on the Reynolds number:

$$St = \frac{fD}{U_\infty} \quad (4.13)$$

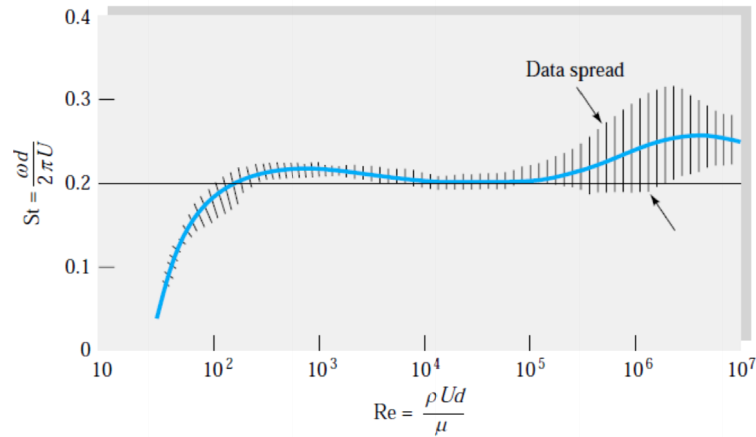


**Figure 4.30:** Experimental Strouhal number for a cylinder versus Reynolds number [16]

where  $D$  is the body diameter and  $U_\infty$  is the free stream velocity. Vortex shedding can induce both in line and cross flow vibration into the body in that specified frequency. The stability plot in Figure 4.22 shows a frequency line at 35.6 Hz and the corresponding mode shape is a cross flow motion, as shown in the Figure 4.31:

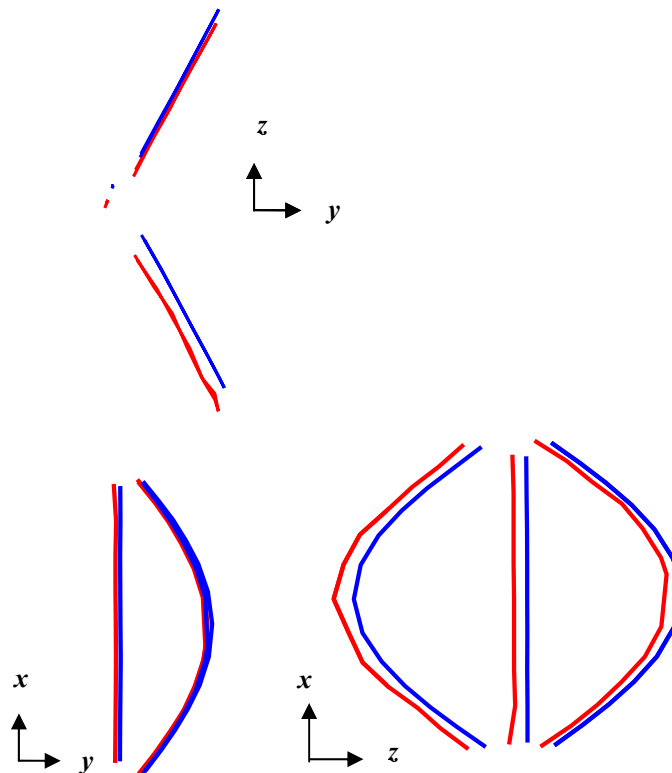


**Figure 4.31:** Cross flow motion of the rotor at 35.68 Hz

To investigate the physical reason of this frequency, the vortex shedding frequency past the rotor needs to be estimated. To simplify the vortex structure around the turbine, it is

assumed that the vortex shed past the rotor shaft as a long cylinder. Thus, the frequency induced by the vortex shedding can be estimated using equation (4.13) and by looking up the Strouhal number for the flow Reynolds number. The rotor shaft diameter is 150 mm, the mean value of the wind speed in the wind tunnel is 25 m/s and the tunnel flow temperature during the experiment is 25°C–27°C; thus,  $Re = 2.299 \times 10^5$ . According to Figure 4.30, the St number is about 0.2 for this flow and the vortex shedding frequency using equation (4.13) is 33.33 Hz. This number is within 7% of the frequency for the cross flow motion in the stability plot. The vortex shedding past a rotor is more complex than the vortex shedding past a cylinder, and the vortex shedding structure and frequency also affect the blade a lot. Therefore, assuming that the vortex shedding over the rotor as the vortex structure past a cylinder, makes this difference between the calculated vortex shedding frequency and what experiment shows in the stability plot.

## 4.9 Modal Identification using FDD

FDD starts with the estimation of the power spectral density (PSD) matrix at each particular frequency [6]. The PSD matrix for each frequency comprises the spectral density function between all the measurement channels:

$$\hat{G}_{yy}(j\omega_i) = \begin{pmatrix} \hat{G}_{y_1y_1}(j\omega_i) & \hat{G}_{y_1y_2}(j\omega_i) & \cdots & \hat{G}_{y_1y_{n_c}}(j\omega_i) \\ \hat{G}_{y_2y_1}(j\omega_i) & \hat{G}_{y_2y_2}(j\omega_i) & \cdots & \hat{G}_{y_2y_{n_c}}(j\omega_i) \\ \vdots & \vdots & \cdots & \vdots \\ \hat{G}_{y_{n_c}y_1}(j\omega_i) & \hat{G}_{y_{n_c}y_2}(j\omega_i) & \cdots & \hat{G}_{y_{n_c}y_{n_c}}(j\omega_i) \end{pmatrix} \quad (4.14)$$

where  $n_c$  is the number of channels and  $y_i, i = 1, 2, \dots, n_c$  is the measurement data. PSD functions are calculated using Bartlett's method. In this method, the signal has been divided into several segments and the power spectra of the segments are averaged to reduce the noise [7]. The power spectrum of each segment with length of  $N$  and sampled with  $f$  Hertz is calculated using discrete Fourier transform (DFT):

$$G_{y_iy_j}(j\omega) = \frac{|DFT(segment)|}{N \times f} \quad (4.15)$$

After establishing the PSD matrix, it should be decomposed by the SVD method in each frequency according to equation (2.51) in 'Introduction to Operational Modal Analysis' chapter. In the singular value plot, the entire set of singular values for all the channels are plotted versus frequency and the frequency resolution depends on the number of segments. For fewer segments, the frequency resolution is higher. Then, the natural

frequencies, mode shapes and damping ratios are determined by the peaks represented in the singular value plot (the detailed procedure has been described in section 2.3.1). As mentioned before, the rotor shaft and the two blades are monitored. On each blade there are 25 monitored points and 17 points are measured on the rotor shaft. The displacement is measured in 3 axes,  $x$ ,  $y$  and  $z$ , in each point. Therefore, there are 201 measurement channels in total. However, to compare the FDD results with the DD-SSI, the measurement points are picked every second like with the DD-SSI analysis and  $n_c = 3 \times 35 = 105$ .

The singular value plot with 800 segments is shown in the Figure 4.32.

### Singular value

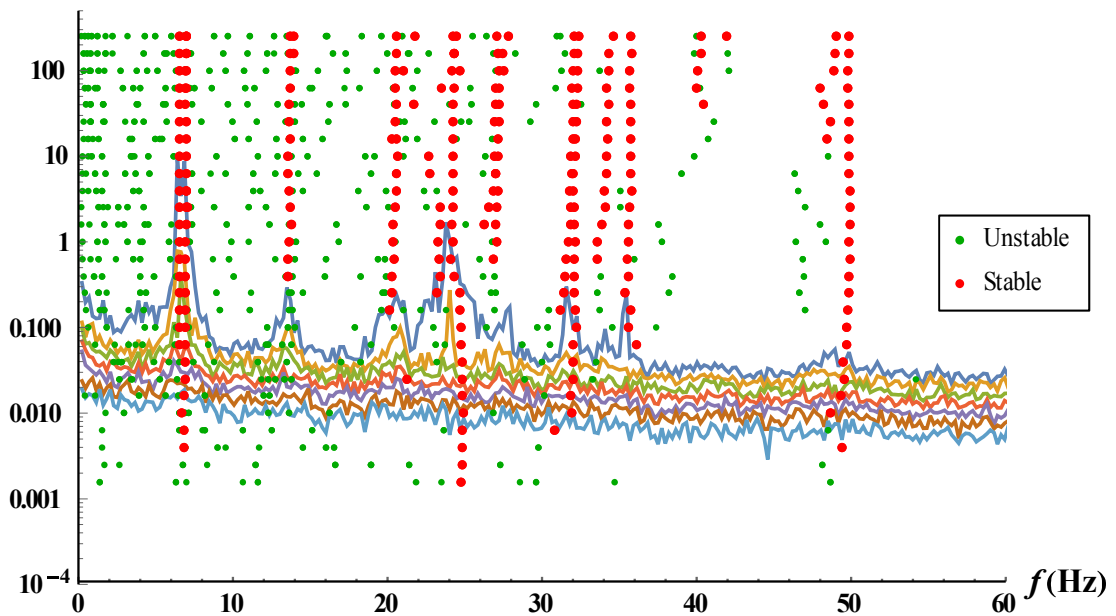


Figure 4.32: Singular value plot

As shown in Figure 4.32, the peaks of the singular value plot agree with the frequencies obtained from DD-SSI. In the close modes, e.g. the first and second rotor shaft modes, FDD has worked as well as DD-SSI, but in very closely spaced modes like the second blade flatwise mode and the fourth wire mode, the results of FDD are weaker than those of DD-SSI. In addition, in the last blade mode (about 50 Hz), which has less energy compared with the other modes, the peak in the singular value plot is not sharp and clear enough, and it cannot be well picked, but the DD-SSI algorithm caught this mode very well.

## 4.10 Classical modal experiment on the VAWT rotor

After finishing the wind tunnel experiment in Italy, the rotor was disassembled and shipped to Denmark. In Risø, DTU, the VAWT was investigated further on structural dynamics to investigate the structural modes of the turbine using the following setup and testing constraints. The turbine base was fixed to the floor with bolts and the acceleration responses of the rotor were measured with the classical B&K pulse equipment at a number of points. The boundary conditions and constraints are different in this experiment compared with those in the wind tunnel experiment; the blades are detached from the rotor shaft and assembled again. Thus, the blades are likely not as tight as during the wind tunnel experiment; the rotor shaft is bolted to the floor, which is different from the rotor foundation and fixations with wires and a longer shaft under the rotor in the tunnel. Therefore, because of the mentioned differences, some differences are expected in the structural modes, especially in the rotor shaft modes.

Modal analysis was conducted with the PULSE LabShop software. The acceleration signals were measured using three accelerometers in four measurement sets. In the first measurement (blade measurement 1#, Figure 4.33-left), the accelerometers (accelerometers 1, 2 and 3, Figure 4.33-right) are placed at three points on the middle of the blade in flatwise and edgewise directions. These points, which are positioned from the leading edge (LE) to the trailing edge (TE), move in the modes that have symmetric motion with respect to the blade midpoint. Figure 4.33-right shows the direction and position of the accelerometers on the blade. In the second measurement (blade measurement 2#, Figure 4.33-left), the accelerometers are placed at the points that also move with the modes with anti-symmetric motion with respect to the blade midpoint.

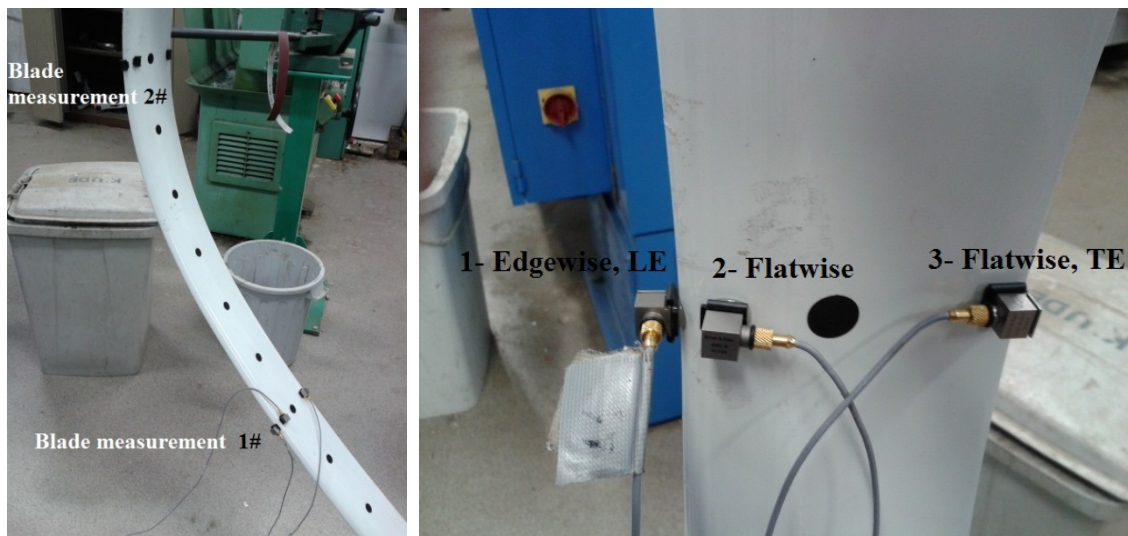


**Figure 4.33:** The setup of the accelerometers on the blade in the classical modal experiment

In the two next measurements, accelerometers are placed perpendicular and tangential relative to the surface on the rotor shaft (Figure 4.34).

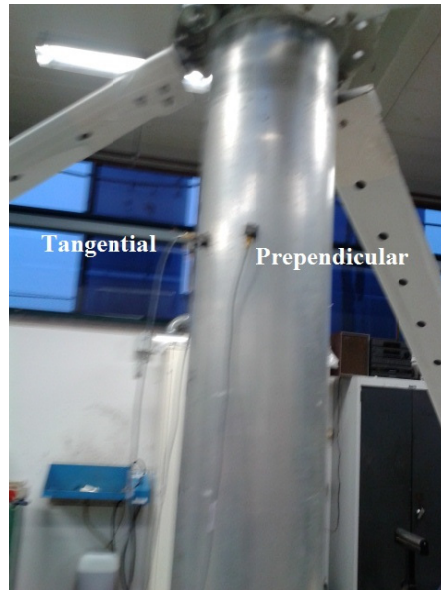


**Figure 4.34:** The way of positioning the accelerometers on the rotor shaft in the two last experiments

In these two last measurements, the hammer hits the blade and rotor shaft. FRFs obtained from four measurements are shown in Figure 4.35.

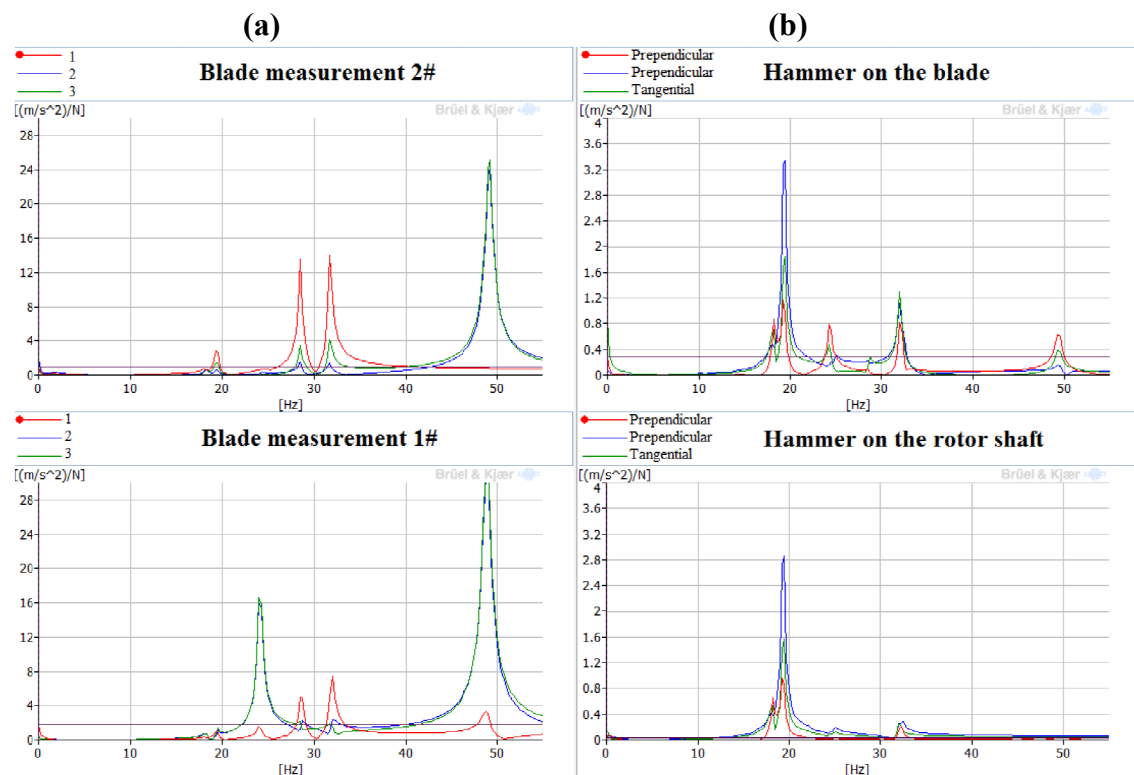


**Figure 4.35:** FRFs from PULSE measurements on the (a): blade and (b): rotor shaft

According to the FRFs, in this experiment, the blade response to the hammer excitation is stronger than the rotor shaft response despite the wind tunnel experiment (by comparison of the power spectrums in two experiments). This can be because of the difference between the rotor base configurations in the two experiments. In the PULSE experiment, the rotor shaft was bolted on the ground, and in the wind tunnel experiment, the rotor shaft was connected to another shaft supported by four guy wires that made it more flexible. This difference also leads to the observation that the first rotor shaft modes occur in the lower frequencies in the wind tunnel experiment compared with those in the PULSE experiment.

The first blade mode is at  $25.25\text{ Hz}$ , the anti-symmetric mode (with respect to the blade midpoint) with a stronger flatwise and a weaker edgewise component. This mode is present in the wind tunnel experiment at  $24.5\text{ Hz}$  in both flatwise and edgewise directions, since the blades in this experiment are attached tighter and are more dampened in the edgewise direction compared with that in the wind tunnel experiment.

The two next blade modes are symmetric modes at  $28.5$  and  $32\text{ Hz}$  with stronger edgewise motion. By looking at the rotor shaft FRFs of Figure 4.35, it is seen that the symmetric mode at  $32\text{ Hz}$  influences the rotor shaft as well, and then, it will be the rotor twist, which also twists the rotor shaft. Despite the wind tunnel experiment, the rotor twist mode is after the other edgewise mode that shows the difference of the blade joints and rotor shaft foundation in the two experiments.

Last blade mode in  $49.25\text{ Hz}$  shows a symmetric behaviour in the edgewise direction. The flatwise motion of this mode is weaker because of the tight joints of the blades.

## 4.11 Conclusion

The displacements of the blades and the rotor shaft of a 3-bladed VAWT rotor in the wind tunnel have been measured with a two camera stereo vision technique, and the modal properties of the rotor were estimated by means of OMA using DD-SSI and FDD. The physical modes in the SSI stability plot include the structural modes, wire modes and induced vortex shedding frequency. To support the identification of the rotor structural modes in the stability plot, the VAWT rotor in the wind tunnel was simulated using HAWC2. This simulation has been conducted without considering aerodynamics to predict the structural modes of the rotor, and the differences between experimental and simulation results are explained by the aerodynamic effects in the wind tunnel. The singular value plot is also obtained via FDD for comparison with the SSI results. The peaks in the singular value plot confirmed the modes estimated by SSI; however, for very closely spaced modes, the performance of DD-SSI is better than that of FDD. Finally, the classical modal experiment was conducted to verify the structural modes that were obtained from OMA. As it was not possible to do this experiment with the same condition as the operational test, there are some differences between the detected

natural frequencies due to the different rotor boundary conditions, but in total the structural modes are compatible with OMA.

Because of only having two cameras for sensing the dynamics of the rotor, only a part of the rotor was captured in the images, and due to the limited computer memory and hard disk speed, the relatively short displacement time series were acquired in this experiment. This leads to the difficulties in studying the overall modal behaviour of the rotor. The stereo vision system including the cameras and the computer system can be improved by increasing the number of cameras and upgrading the data acquisition system. With this extension of the hardware setup, the VAWT rotor structure can be studied in both parked states and during operation. In addition, some extra strain gauges can be installed on the rotor, the foundation structure and the guy wires to validate the stereo vision measurements.



## References

- [1] Trucco, E., Verri, A. (1997): A Four-step Camera Calibration Procedure with Implicit Image Correction, pp. 1106-1112, Proceedings of IEEE Computer Society Conference on Computer Vision and Pattern Recognition, San Juan, United States.
- [2] Leo, G. D., Liguori, C., and Paolillo, A. (2011): Covariance Propagation for the Uncertainty Estimation in Stereo Vision, pp. 1664-1673, IEEE Transactions on Instrumentation and Measurement 60(5).
- [3] Overschee, P. V., De Moor, B. (1996): Subspace Identification for Linear Systems, Kluwer Academic Publishers.
- [4] Kirkegaard, P. H., and Andersen, P. (1997): State Space Identification of Civil Engineering structures from Output Measurements, Proceedings of the 15th International Modal Analysis Conference, Orlando, Florida.
- [5] Golub, G. H., Van Loan, C. F. (1996): Matrix Computations, Third edition, The John Hopkins University Press.
- [6] Bincker, R., Zhang, L., and Andersen (1999): Modal Identification from Ambient Response using Frequency Domain Decomposition, pp. 625-630, MAC 18: Proceedings of the International Modal Analysis Conference (IMAC), San Antonio, Texas, USA.
- [7] Vaseghi, S. V. (2008): Advanced Digital Signal Processing and Noise Reduction, John Wiley and Sons, Ltd, Publication.
- [8] Rao, S. S. (2007): Vibration of Continuous systems, John Wiley & Sons, Inc.
- [9] Larsen, T. J., Hansen, A. M. (2014): How 2 HAWC2, the user's manual, Risø-R-1597(ver. 4-5).
- [10] Krenck, S. (1999): Dynamic Analysis of Structure: Numerical Time Inegration, Course of Non-Linear Analysis of Frame structures, Esbjerg, Denmark.
- [11] Vita, L. (2011): PhD Thesis: Offshore Vertical Axis Wind Turbine with Floating and Rotating Foundation, Risø DTU, Roskilde, Denmark.
- [12] Claessens, M. C. (2006): Master of Science Thesis: Design and Testing of Airfoils for Application in Small Vertical Axis Wind Turbines. Delft University of Technology, Faculty of Aerospace Engineering
- [13] Carne, T. G. (1980): Guy Cable Design and Damping for Vertical Axis Wind Turbines, Report, Sandia National Laboratories, Albuquerque, NM, USA.
- [14] Yamaguchi, H., Adhikari, R. (1995): Energy-Based Evaluation of Modal Damping In Structural Cables With And Without Damping Treatment, pp. 71-83, Journal of Sound and Vibration 181(1).
- [15] Barbieri, N., Souza Jr., O. H. and Barbieri, R. (2004): Dynamical analysis of transmission line cables. Part 2—damping estimation, pp. 671-681, Mechanical Systems and Signal Processing 18.
- [16] White, F. M. (1991): Viscous Fluid Flow, Second Edition, McGraw-Hill, Inc.

## 5. Uncertainty Analysis in Stereo reconstruction

### 5.1 Introduction

The measurement uncertainty characterizes the scatter of the measured value. The result of a measurement is an estimate of the real value due to the uncertainty arising from the random effects and corrections originating from imperfections that give rise to an error [1]. Uncertainty analysis for a stereo vision system determines the precision of the measured displacements in three dimensions.

The uncertainty of the 3D displacement measurement via stereo vision has been evaluated in a few studies and a few methods have been presented [2,3,4]. For example in [2], different sources of errors such as correlation window size, focus, maximum disparity and stereo baseline are investigated for a specific stereo vision case, and finally, they have been combined to estimate the total error of stereo vision. The method used in this chapter follows a more generalized method that is presented in [5]. This method uses the law of propagation of error to evaluate the uncertainty propagates through the linear camera model. The uncertainty in stereo reconstruction propagates in two cases: camera calibration and 3D reconstruction of the point from 2D projections in image pairs [5]. In this chapter, the uncertainty propagation is analytically evaluated through a linear camera model of a stereo vision system, and it will be implemented and analysed for the two stereo reconstruction cases used in this study. There may be systematic errors like camera vibrations in the stereo vision measurement that are not discussed in this chapter.

### 5.2 Propagation of uncertainty

A multivariate and explicit measurement is modelled as a function of several uncertain inputs:

$$y = g(x_1, \dots, x_j, \dots, x_q) \quad (5.1)$$

The variation of  $y$  can be calculated through the first order Taylor expansion [6]:

$$\delta y = \left( \frac{\partial g}{\partial x_1} \right) \delta x_1 + \dots + \left( \frac{\partial g}{\partial x_j} \right) \delta x_j + \dots + \left( \frac{\partial g}{\partial x_q} \right) \delta x_q \quad (5.2)$$

For series of  $n$  measurements, a system of  $n$  equations is obtained:

$$\begin{aligned}
\delta y_1 &= \left( \frac{\partial g}{\partial x_1} \right) \delta x_{11} + \dots + \left( \frac{\partial g}{\partial x_j} \right) \delta x_{1j} + \dots + \left( \frac{\partial g}{\partial x_q} \right) \delta x_{1q} \\
&\dots \\
\delta y_i &= \left( \frac{\partial g}{\partial x_1} \right) \delta x_{i1} + \dots + \left( \frac{\partial g}{\partial x_j} \right) \delta x_{ij} + \dots + \left( \frac{\partial g}{\partial x_q} \right) \delta x_{iq} \\
&\dots \\
\delta y_n &= \left( \frac{\partial g}{\partial x_1} \right) \delta x_{n1} + \dots + \left( \frac{\partial g}{\partial x_j} \right) \delta x_{nj} + \dots + \left( \frac{\partial g}{\partial x_q} \right) \delta x_{nq}
\end{aligned} \tag{5.3}$$

where ‘i’ indicates the i<sup>th</sup> set of measurements. If  $c_j = \left( \frac{\partial g}{\partial x_j} \right)$  is the partial derivation of the function g, the matrix representation of the equation (5.3) is:

$$\begin{Bmatrix} \delta y_1 \\ \cdot \\ \delta y_i \\ \cdot \\ \delta y_n \end{Bmatrix} = \begin{bmatrix} \delta x_{11} & \cdot & \delta x_{1j} & \cdot & \delta x_{1q} \\ \cdot & \cdot & \cdot & \cdot & \cdot \\ \delta x_{i1} & \cdot & \delta x_{ij} & \cdot & \delta x_{iq} \\ \cdot & \cdot & \cdot & \cdot & \cdot \\ \delta x_{n1} & \cdot & \delta x_{nj} & \cdot & \delta x_{nq} \end{bmatrix} \begin{Bmatrix} c_1 \\ \cdot \\ c_i \\ \cdot \\ c_n \end{Bmatrix} \text{ or } \{ \delta y_i \} = [ \delta x_{ij} ] \{ c_j \} \tag{5.4}$$

By knowing the variance of the measurement,

$$s^2(y) = \frac{\sum_{i=1}^n (\delta y_i)^2}{n-1} = \frac{\{ \delta y_i \} \{ \delta y_i \}^T}{n-1} = \{ c_j \} \frac{[ \delta x_{ij} ] [ \delta x_{ij} ]^T}{n-1} \{ c_j \}^T \tag{5.5}$$

The output uncertainty is [7]:

$$u_g^2 = J_x \Lambda_x J_x^T \tag{5.6}$$

where  $\Lambda_x$  is the input covariance matrix and  $J_x$  is the input Jacobian matrix (matrix of partial derivations).

In implicit and multivariate input–output measurements, there is no rapid and direct function connecting inputs and outputs. The model of these systems is an equation relating x and y [7]:

$$g(x, y) = 0 \tag{5.7}$$

The measurement result is given by solving equation (5.7). In these cases, the output and input covariance matrices are related as follows:

$$J_y \Lambda_y J_y^T = J_x \Lambda_x J_x^T \quad (5.8)$$

## 5.3 Uncertainty propagation in the stereo vision reconstruction

Uncertainty propagates from two sources in stereo vision:

- 1- The calibration of the cameras that depends on different parameters like the printing precision of the calibration board, the precision of picking the pixel coordinates of the calibration board points in the images and the calibration algorithm and formulation.
- 2- 3D reconstruction of the points in the real world from image projections [5].

### 5.3.1 Uncertainty propagation in camera calibration

In camera calibration, the camera parameters of a camera model are estimated using equation (4) in chapter 4. In these equations, the calibration board points coordinates in the image plane,  $P_{ui}^I = (x_{ui}^I, y_{ui}^I)$ , and in the real world,  $P_{wi}^W = (x_{wi}^W, y_{wi}^W, z_{wi}^W)$ , are known for  $i=1, \dots, N$ , where N is the grid points number. Therefore, the camera parameters are obtained by solving 2N equations [5]:

$$\begin{aligned} f_x(\alpha, P_w^W, P_u^I) &= 0 \\ f_y(\alpha, P_w^W, P_u^I) &= 0 \end{aligned} \quad (5.9)$$

where  $\alpha = [\alpha_1, \alpha_2, \dots, \alpha_{10}]^T = [\omega, \varphi, \kappa, T_x, T_y, T_z, -\frac{f}{s_x}, -\frac{f}{s_y}, o_x, o_y]$  is the camera parameters (calibration output).  $\omega, \varphi$  and  $\kappa$  are the rotational angles around  $x, y$  and  $z$ , respectively.

In a compact form, the calibration problem is formulated as [5]:

$$F(\alpha, l) = 0 \quad (5.10)$$

where  $l^T = [(l_1)^T, \dots, (l_1)^T]$ ,  $(l_i)^T = [(P_i^W)^T, (P_i^I)^T]$ .

While  $\Lambda_l$  and  $\Lambda_\alpha$  are the covariance matrices of the input  $l$  and the covariance matrices of output  $\alpha$ , respectively, according to equation (5.8):

$$J_\alpha \Lambda_\alpha J_\alpha^T = J_l \Lambda_l J_l^T \quad (5.11)$$

where  $\Lambda_l = \text{diag}\{\Lambda_{l1}, \dots, \Lambda_{lN}\}$ ,  $\Lambda_{li} = \text{diag}\{u^2(x_{wi}^W), u^2(y_{wi}^W), u^2(z_{wi}^W), u^2(x_{ui}^I), u^2(y_{ui}^I)\}$ ,  $J_l$  is the Jacobian matrix of derivatives of F with respect to  $l$ ,  $J_l = \text{diag}\{J_{l1}, \dots, J_{lN}\}$

$$J_{li} = \begin{bmatrix} \frac{\partial f_x(\alpha, P_{wi}^W, P_{ui}^I)}{\partial x_w^W} & \frac{\partial f_x(\alpha, P_{wi}^W, P_{ui}^I)}{\partial y_w^W} & \frac{\partial f_x(\alpha, P_{wi}^W, P_{ui}^I)}{\partial z_w^W} & \frac{\partial f_x(\alpha, P_{wi}^W, P_{ui}^I)}{\partial x_u^I} & \frac{\partial f_x(\alpha, P_{wi}^W, P_{ui}^I)}{\partial y_u^I} \\ \frac{\partial f_y(\alpha, P_{wi}^W, P_{ui}^I)}{\partial x_w^W} & \frac{\partial f_y(\alpha, P_{wi}^W, P_{ui}^I)}{\partial y_w^W} & \frac{\partial f_y(\alpha, P_{wi}^W, P_{ui}^I)}{\partial z_w^W} & \frac{\partial f_y(\alpha, P_{wi}^W, P_{ui}^I)}{\partial x_u^I} & \frac{\partial f_y(\alpha, P_{wi}^W, P_{ui}^I)}{\partial y_u^I} \end{bmatrix} \quad (5.12)$$

and  $J_\alpha$  is the Jacobian matrix of derivatives of F with respect to  $\alpha$ :

$$J_\alpha = \begin{bmatrix} J_{\alpha 1} \\ J_{\alpha 2} \\ \vdots \\ J_{\alpha N} \end{bmatrix}, \quad (5.13)$$

$$J_{li} = \begin{bmatrix} \frac{\partial f_x(\alpha, P_{wi}^W, P_{ui}^I)}{\partial \alpha_1} & \dots & \frac{\partial f_x(\alpha, P_{wi}^W, P_{ui}^I)}{\partial \alpha_7} \\ \frac{\partial f_y(\alpha, P_{wi}^W, P_{ui}^I)}{\partial \alpha_1} & \dots & \frac{\partial f_y(\alpha, P_{wi}^W, P_{ui}^I)}{\partial \alpha_7} \end{bmatrix}$$

Finally, from equation (5.11):

$$\Lambda_\alpha = J_\alpha^- (J_l \Lambda_l J_l^T) (J_\alpha^T)^- \quad (5.14)$$

### 5.3.2 Uncertainty Propagation in stereo reconstruction

As it has been explained in chapter 1, for reconstructing a 3D point of  $P^W = [x^W, y^W, z^W]$ , the lines passing through the centre of projections to the images of the points,  $P_1^{I1} = [x_1^{I1}, y_1^{I1}]$  and  $P_2^{I2} = [x_2^{I2}, y_2^{I2}]$ , intersect. Hence, a set of equations should be solved to intersect line of sights [5]:

$$G(P^W, \nu) = 0 \quad (5.15)$$

where  $\nu^T = [(P_1^{I_1})^T, (P_2^{I_2})^T, (\alpha_1)^T, (\alpha_2)^T]$  and  $\alpha_i = [\alpha_1^{(i)}, \alpha_2^{(i)}, \dots, \alpha_7^{(i)}]^T$  is the vector parameter of camera  $i$ ,  $i = 1, 2$ .

In relation to equation (5.11), the covariance matrices of inputs and outputs in equation (5.15) are related by following equation:

$$J \Lambda J^T = J_\nu \Lambda_\nu J_\nu^T \quad (5.16)$$

where

$$J = \begin{bmatrix} \frac{\partial f_x(\alpha_1, P^W, P_1^{I_1})}{\partial x_w^W} & \frac{\partial f_x(\alpha_1, P^W, P_1^{I_1})}{\partial y_w^W} & \frac{\partial f_x(\alpha_1, P^W, P_1^{I_1})}{\partial z_w^W} \\ \frac{\partial f_y(\alpha_1, P^W, P_1^{I_1})}{\partial x_w^W} & \frac{\partial f_y(\alpha_1, P^W, P_1^{I_1})}{\partial y_w^W} & \frac{\partial f_y(\alpha_1, P^W, P_1^{I_1})}{\partial z_w^W} \\ \frac{\partial f_x(\alpha_2, P^W, P_2^{I_2})}{\partial x_w^W} & \frac{\partial f_x(\alpha_2, P^W, P_2^{I_2})}{\partial y_w^W} & \frac{\partial f_x(\alpha_2, P^W, P_2^{I_2})}{\partial z_w^W} \\ \frac{\partial f_y(\alpha_2, P^W, P_2^{I_2})}{\partial x_w^W} & \frac{\partial f_y(\alpha_2, P^W, P_2^{I_2})}{\partial y_w^W} & \frac{\partial f_y(\alpha_2, P^W, P_2^{I_2})}{\partial z_w^W} \end{bmatrix},$$

$$J_\nu = \begin{bmatrix} J_{\nu 1} & 0 & J_{\alpha 1} & 0 \\ 0 & J_{\nu 2} & 0 & J_{\alpha 2} \end{bmatrix},$$

$$J_{\nu i} = \begin{bmatrix} \frac{\partial f_x(\alpha_i, P^W, P_i^{I_i})}{\partial x_u^I} & \frac{\partial f_x(\alpha_i, P^W, P_i^{I_i})}{\partial y_u^I} \\ \frac{\partial f_y(\alpha_i, P^W, P_i^{I_i})}{\partial x_u^I} & \frac{\partial f_y(\alpha_i, P^W, P_i^{I_i})}{\partial y_u^I} \end{bmatrix},$$

$$J_{\alpha i} = \begin{bmatrix} \frac{\partial f_x(\alpha_i, P^W, P_i^{I_i})}{\partial \alpha_1^{(i)}} & \dots & \frac{\partial f_x(\alpha_i, P^W, P_i^{I_i})}{\partial \alpha_7^{(i)}} \\ \frac{\partial f_y(\alpha_i, P^W, P_i^{I_i})}{\partial \alpha_1^{(i)}} & \dots & \frac{\partial f_y(\alpha_i, P^W, P_i^{I_i})}{\partial \alpha_7^{(i)}} \end{bmatrix}$$

$\Lambda_\nu = \text{diag}\{\Lambda_{\nu 1}, \Lambda_{\nu 2}, \Lambda_{\alpha 1}, \Lambda_{\alpha 2}\}$  and  $\Lambda_{\nu i} = \text{diag}\{u^2(x_i^{I_i}), u^2(y_i^{I_i})\}$ ,  $i = 1, 2$ .

$u(P_i^{I_i})$  is the uncertainty of image point coordinates. Finally, the covariance of the output is:

$$\Lambda = J^- (J_\nu \Lambda_\nu J_\nu^T) (J^T)^- \quad (5.17)$$

## 5.4 Uncertainty analysis for the blade experiment

In this section, the uncertainty of the displacement measurements of the blade experiment in the field (chapter 3) is estimated. Three sets of displacement measurements are analysed in this experiment, and the uncertainty is estimated for all of them.

In the first step, the uncertainty that propagates through the camera calibration is calculated using the method mentioned in section 5.3.1. In this procedure, the uncertainty of the input quantities should be known [8]:

- 1- Uncertainty of the calibration grid points coordinates in  $mm$ ,  $u(x_{wi}^W)$ ,  $u(y_{wi}^W)$  and  $u(z_{wi}^W)$ .
- 2- Uncertainty of the grid point localization in pixels,  $u(x_{ui}^I)$  and  $u(y_{ui}^I)$ .

A calibration grid has been drawn using a regular ruler with the smallest intervals of 1 mm and a fine permanent marker with tip size of 0.6 mm. For the uncertainty estimation of the grid point coordinates, it is assumed that the maximum deviation of each of the grid line is equal to the marker tip size. Hence, the standard deviation is obtained using the normal distribution:

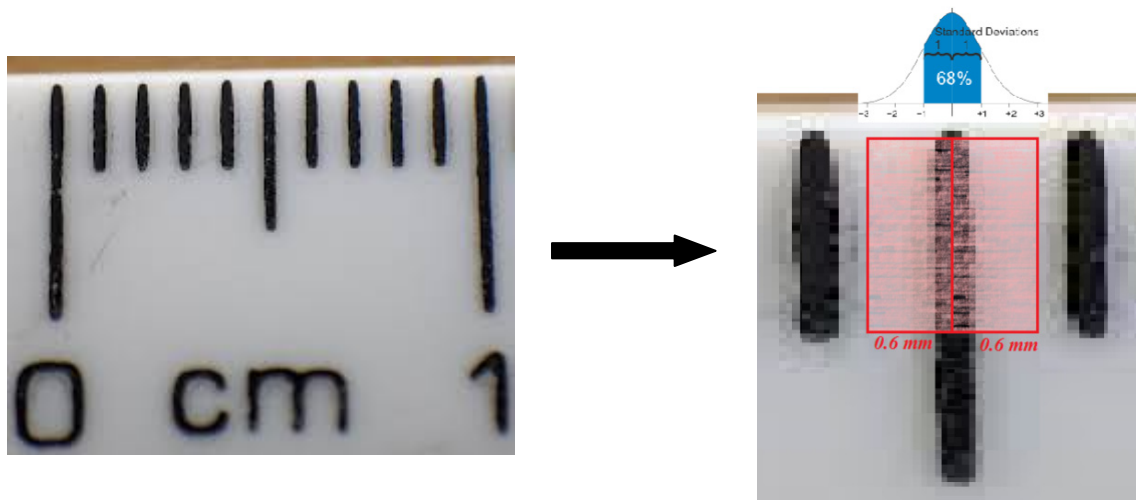


**Figure 5.1:** Uncertainty estimation of the grid point coordinates

$$\sigma = 0.34 \times 0.6 = 0.204 \text{ mm}$$

As each of the grid points is made by crossing two of the grid lines, the total uncertainty of the point coordinates is equal to:

$$\sqrt{\sigma^2 + \sigma^2} = \sigma\sqrt{2} = 0.288 \text{ mm}$$

There are also other sources, such as the ruler alignment, which affect the coordinates' uncertainty. In addition, the calibration grid is plotted on a paper and is stuck on the calibration board; hence, the air bubbles between the paper and the plate increase the uncertainty. By considering these issues on the total grid, a bigger uncertainty is estimated:  $u(x_{wi}^W), u(y_{wi}^W) = 0.35mm$ .

The points of the calibration grid are manually picked in the images. Therefore, the procedure is picking a particular point several times (e.g. 20) and the uncertainty is estimated as the standard deviation of all the values. Finally,  $u(x_{ui}^I), u(y_{ui}^I) = 0.1$  pixel.

In the uncertainty analysis of the calibration process, the rotational angles,  $\omega$ ,  $\varphi$  and  $\kappa$ , are a part of the output quantities. Hence, the rotational matrix components should be replaced in equation (3.4) according to the angles:

$$R = \begin{pmatrix} r_{11} & r_{12} & r_{13} \\ r_{21} & r_{22} & r_{23} \\ r_{31} & r_{32} & r_{33} \end{pmatrix} = \begin{pmatrix} \cos \varphi \cos \kappa & \cos \omega \sin \kappa + \sin \omega \sin \varphi \cos \kappa & \sin \omega \sin \kappa - \cos \omega \sin \varphi \cos \kappa \\ -\cos \varphi \sin \kappa & \cos \omega \cos \kappa - \sin \omega \sin \varphi \sin \kappa & \sin \omega \cos \kappa + \cos \omega \sin \varphi \sin \kappa \\ \sin \varphi & -\sin \omega \cos \varphi & \cos \omega \cos \varphi \end{pmatrix} \quad (5.18)$$

In the current calibration case, the calibration board is 2D; hence, the third dimension is considered to be constant for all the grid points, and hence, there is no uncertainty associated with it. In addition, the effective pixel size in the horizontal and vertical directions ( $s_x, s_y$ ) are identical in the camera; hence, the output quantities is reduced to

$$\alpha = [\alpha_1, \alpha_2, \dots, \alpha_9]^T = [\omega, \varphi, \kappa, T_x, T_y, T_z, -\frac{f}{s_x}, o_x, o_y]$$

After calculating the rotational angles, the calibration output covariance matrix for the left and right cameras is obtained using the proposed method in section 5.3.1 as part of the inputs for uncertainty propagation estimation in 3D reconstruction.

In 3D reconstruction of a point via stereo vision, the pixel coordinates of the point are found in the image planes of the both cameras. Hence, one of the important uncertainty sources is the pixel localization of the points in the images ( $u^2(x_i^I)$  and  $u^2(y_i^I)$ ). This uncertainty depends on the image acquisition system and the feature extraction algorithm from the image. The uncertainty from the image acquisition system, which is because of the factors like the lens distortion, sensor thermal noise and the sensor intensity quantization, will propagate through the algorithm for extracting the pixel coordinates from the image [8]. Thus, the uncertainty of the pixel coordinates depends on a variety of factors, and its analytical estimation is a complicated issue. In an easier approach, this uncertainty can be estimated by an experimental approach, i.e. by taking a picture of the same objects several times and extracting the position of the identical features with the identical algorithm, the standard deviations of the pixel coordinates is considered as the uncertainty.



In the blade experiment, the experimental approach was used to calculate the standard deviation of the pixel coordinate of the image points. Twenty pictures were taken from the blade while it was at standstill. The standard deviation of the extracted pixel coordinates of the marker points by the image processing algorithm is  $u(x_i^{I_i}) = 0.04$  pixel and  $u(y_i^{I_i}) = 0.05$  pixel in the image processing algorithm of the blade experiment; there is no perspective correction on the ellipse centroid to get the real image of the circle centre, due to the lack of knowledge about the markers radius. Therefore, 0.5 pixel is added to the pixel coordinate uncertainty to include the bias error of the elliptical correction:

$$u(x_i^{I_i}) = \sqrt{0.04^2 + 0.5^2} \approx 0.501 \text{ pixel}$$

$$u(y_i^{I_i}) = \sqrt{0.05^2 + 0.5^2} \approx 0.502 \text{ pixel}$$

The baseline length in the stereo vision setup and the depth of the object with respect to the camera positions are two important factors that affect the uncertainty propagation in the stereo vision process. As a thumb rule, the uncertainty in a particular depth increases as the baseline length decreases, as shown in Figure 5.2. However, by increasing the baseline length, the common field of views reduces for the camera pairs. In addition, the corresponding areas and points look more different in the image planes of the cameras. Therefore, the correspondence problem will be more difficult when a longer baseline length is used [9]. Thus, choosing the length of the baseline is a critical issue, which depends of the experimental conditions.

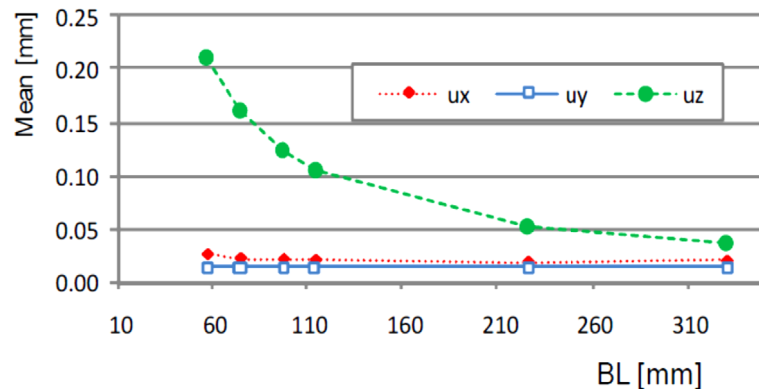


**Figure 5.2:** Mean value of the uncertainty for different baseline (BL) values [9]

In the blade experiment, three measurement sets have been used in the modal analysis of the blade. The uncertainty of the markers on the blade is presented in Table 5.1. The stereo vision setup is approximately the same in the first and second measurements (the baseline length is about  $2m$  and the distance between the calibration board and the

cameras is about  $6m$  ). Thus, the mean uncertainties of the first and third measurements in time are listed in the following table.

**Table 5.1:** Mean uncertainties of the first and third measurements

Mean point Coordinate No.1	Mean $u(x^w)$ (mm)	Mean $u(y^w)$ (mm)	Mean $u(z^w)$ (mm)	Mean point Coordinate No.2	Mean $u(x^w)$ (mm)	Mean $u(y^w)$ (mm)	Mean $u(z^w)$ (mm)
x=-523.061 y=18.918 z=7.771	0.508	0.238	1.507	x=-486.050 y=-80.201 z=-118.452	0.219	0.277	1.120
x=-440.249 y=25.256 z=63.690	0.575	0.260	1.794	x=-406.396 y=-93.789 z=-71.596	0.202	0.247	0.940
x=-300.063 y=21.634 z=161.414	0.703	0.309	2.345	x=-263.150 y=-111.014 z=11.686	0.198	0.219	0.672
x=-156.843 y=22.870 z=260.843	0.833	0.368	2.974	x=-115.968 y=-123.852 z=96.880	0.217	0.230	0.540
x=-11.088 y=24.489 z=356.229	0.952	0.432	3.644	x=33.993 y=-136.243 z=177.828	0.259	0.271	0.612
x=96.248 y=30.520 z=451.032	1.047	0.488	4.213	x=147.195 y=-142.605 z=262.700	0.328	0.333	0.793
x=129.874 y=34.270 z=491.327	1.081	0.508	4.418	x=183.820 y=-143.872 z=300.160	0.366	0.363	0.875
x=173.545 y=35.495 z=549.937	1.130	0.536	4.689	x=231.920 y=-149.043 z=354.865	0.430	0.408	0.992
x=227.999 y=42.034 z=646.599	1.206	0.578	5.088	x=294.596 y=-152.79 z=447.439	0.548	0.489	1.185
x=265.266 y=46.042 z=742.607	1.278	0.616	5.419	x=340.597 y=-158.243 z=541.259	0.679	0.573	1.378
x=288.572 y=50.179 z=839.921	1.348	0.652	5.705	x=373.271 y=-163.095 z=638.189	0.818	0.663	1.589

In the first measurement, the mean value of the averaged uncertainty of all the points in the  $x$ ,  $y$  and  $z$  directions is 0.969, 0.453 and 3.800  $mm$ . The minimum and maximum values are also 0.508, 0.238 and 1.507  $mm$  and 1.348, 0.652 and 5.705  $mm$ , respectively. Furthermore, the mean, minimum and maximum values for the third measurement are 0.387, 0.370 and 0.972  $mm$ , 0.197, 0.219 and 0.540  $mm$  and 0.818, 0.663 and 1.589  $mm$ , respectively.

In the third measurement, the distance between the cameras and the calibration board is about  $5m$  and the distance between the cameras was about  $4m$ . A number of conclusions can be made from inspecting Table 5.1:

- 1- The uncertainty in all directions increases with depth ( $z$ ).
- 2- The uncertainty in the depth direction ( $u(z^W)$ ) is always much higher than that in other directions, and the ratio between  $u(z^W)$  and  $u(x^W)$  or  $u(y^W)$  increases with depth.
- 3- The uncertainties reduce in the third measurement due to the increased baseline length and decreased distance between the cameras and the blade.

## 5.5 Uncertainty analysis for the VAWT experiment in the wind tunnel

In this section, the uncertainty of the displacement measurements in chapter 4 is evaluated using the method proposed in the beginning of this chapter. A number of points have been considered in the experiment to decrease the output uncertainty:

- 1- The calibration grid was printed by a printer with a resolution of  $\frac{1}{1200} dpi$  (dots per inch) and stuck on a wooden board to avoid air bubbles to develop under the grid points and to decrease the input uncertainty of the calibration process.
- 2- Circular markers were printed in paper and stuck on the blades and rotor shaft.
- 3- The perspective correction was conducted to get the centre of the circular markers out of their elliptical projection. It reduces the input uncertainty in the triangulation uncertainty propagation.
- 4- The baseline length was a challenging issue in this experiment. Two main challenges limited the increase of the baseline length:
  - The vertical axis wind turbine blades are curved and are not coplanar; hence, the baseline length can increase until all the corresponding points are seen in both cameras.
  - The dimensions of the platform where the cameras are placed limit the camera movements.
- 5- The lens with the smaller focal length ( $40 mm$ ) was mounted on the camera to allow for a decreased distance between the turbine and the cameras.

For calculating the calibration uncertainty, the uncertainty of the calibration grid point coordinates is determined by assuming a rectangular distribution for the printer resolution. On the other hand, for digital indicating devices, the resolution uncertainty is

half of the least significant digit with an assumed rectangular probability distribution, as illustrated in Figure 5.3.

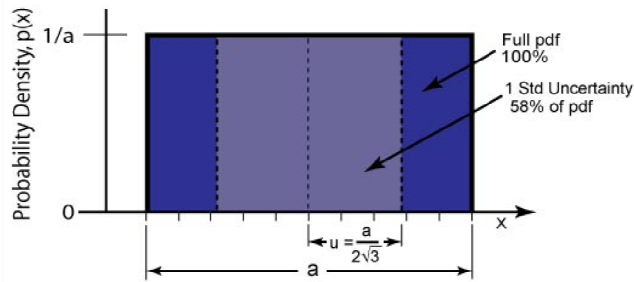


**Figure 5.3:** Rectangular probability distribution

The standard uncertainty for a uniform or rectangular distribution is:

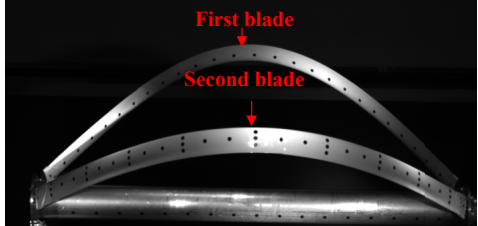
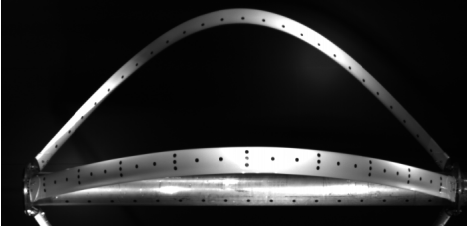
$$u = \frac{a}{2\sqrt{3}} \quad (5.19)$$

where  $a$  is the least significant digit of the device. Therefore, the uncertainty of the calibration grid points is  $u(x_{wi}^w), u(y_{wi}^w) = \frac{1}{2 \times 1200 \times \sqrt{3}} \text{ inch}$ .

The calibration grid points are picked manually in the image; thus, the uncertainty of the pixel localization is estimated with the same procedure as the blade experiment, and the result is  $u(x_{ui}^l), u(y_{ui}^l) = 0.5 \text{ pixel}$ .

As it has been mentioned in the previous section, estimating the uncertainty of the point's localization in the images for the 3D reconstruction process is complicated and depends on many different factors. Hence, 20 images were taken from the standstill VAWT in no wind condition, and the algorithm was used to extract the pixel positions of the markers on the rotor shaft and the blades. Then, the standard deviation of the pixel coordinates on each point is calculated. For each part (rotor shaft, first and second blade), the mean value of the standard deviation of the pixel coordinates is considered as the input uncertainty of the 3D reconstruction.

**Table 5.2:** Uncertainty of image point coordinates in pixels

	<b>Left image</b>	<b>Right image</b>
		
<b>Rotor shaft</b>	$u(x_i^{l_i}) = 0.08, u(y_i^{l_i}) = 0.06$	$u(x_i^{l_i}) = 0.06, u(y_i^{l_i}) = 0.05$
<b>First blade</b>	$u(x_i^{l_i}) = 0.06, u(y_i^{l_i}) = 0.07$	$u(x_i^{l_i}) = 0.06, u(y_i^{l_i}) = 0.07$
<b>Second blade</b>	$u(x_i^{l_i}) = 0.04, u(y_i^{l_i}) = 0.06$	$u(x_i^{l_i}) = 0.05, u(y_i^{l_i}) = 0.07$

There are 67 markers on the rotor shaft and the two blades in total. The uncertainty of each of the point coordinates is averaged in the measurement time. The mean uncertainty value for each part is presented in the following table.

**Table 5.3:** Displacement uncertainty in the VAWT experiment

	Mean $u(x^W)$ (mm)	Mean $u(y^W)$ (mm)	Mean $u(z^W)$ (mm)
<b>Rotor shaft</b>	0.119	0.378	1.164
<b>First blade</b>	0.236	0.747	2.973
<b>Second blade</b>	0.0813	0.243	0.778

Finally, the average of the mean uncertainty for all of the components is 0.145, 0.456 and 1.636 mm in  $x$ ,  $y$ , and  $z$  directions, respectively.

## 5.6 Conclusion

In this chapter, the uncertainty propagation was analytically evaluated through a linear camera model of a stereo vision system and it was implemented in two stereo vision cases: the displacement measurements on a turbine blade and on a rotor VAWT via the stereo vision technique. The uncertainty analysis on the blade experiment illustrated few factors like precision of the calibration grid, perspective correction for the circular markers, the baseline length and the distance between the cameras and object to be measured, which affects the uncertainty in the displacement measurement. Therefore, we recommend that these issues should be considered for future experiments on the VAWT rotor to decrease uncertainty. However, in the second experiment, the calibration grid and the circular markers are printed with much higher precision than that in the first experiment and the distance between the cameras and the rotor was chosen to be as small as possible. However, there were some limitations in increasing the baseline length, such as having limited space to move the cameras and having common fields of view of the cameras, but it was set to be as large as possible. The uncertainty in the VAWT rotor experiment is decreased by considering the previously mentioned points.

## References

- [1] DS/ENV 13005 (1999): Dansk Standard: Guide to the expression n of uncertainty in measurement.
- [2] Kim, W. S., et al. (2005): Performance Analysis and Validation of a Stereo Vision System, IEEE Conference on Systems, Man and Cybernetics.
- [3] Farenzena, M., Fusiello, A. (2005): Rigorous Computing in Computer Vision, Vision, Video and Graphics, Edinburgh, UK.
- [4] Chen, J., Ding, Z., and Yuan, F. (2008): Theoretical Uncertainty Evaluation of Stereo Reconstruction, the 2<sup>nd</sup> International Conference on Bioinformatics and Biomedical Engineering, 16-18 May 2008, pp.2387-2381.
- [5] Haralick, R.M. (1994): Propagating Covariance in Computer Vision, Proceedings of the 12<sup>th</sup> IAPR International Conference on Pattern Recognition, vol.1, 9-13 October 1994, pp.493-498.
- [6] Barbato, G., Germak, A., and Genta, G. (2013): Measurements for Decision Making, Società Editrice Esculapio.
- [7] Cox, M. G., and Harris, P. M. (2006): Software Support for Metrology Best Practice Guide No. 6-Uncertainty Evaluation, NPL Report DEM-ES-011, National Physics Laboratory.
- [8] Leo, G. D., Liguori, C., and Paolillo, A. (2011): Covariance Propagation for the Uncertainty Estimation in Stereo Vision, pp. 1664-1673, IEEE Transactions on Instrumentation and Measurement 60(5).
- [9] Leo, G. D., Liguori, C., and Paolillo, A. (2010): Propagation of Uncertainty through Stereo Triangulation, Instrumentation and Measurement Technology Conference (I2MTC), 2010 IEEE

## 6. Background-oriented schlieren study of the turbine tip vortex

### 6.1 Motivation

The wake propagation downstream of a wind turbine needs to be studied for the wind farm design. The tip vortices are an important part of the wakes that play an important role in turbine aerodynamics. In addition, they lead to the turbine noise and aerodynamic interactions [1]. These issues make tip vortices' study very important.

In the current study, the background-oriented schlieren (BOS) method is used to investigate tip vortices that are shed from a horizontal axis wind turbine blade. The BOS method uses the refractive index change due the density gradient in the medium to study the flow field [2]. This method has been previously used for tip vortices' investigation, but in most cases, the investigation was conducted on the high speed flows ( $Ma > 0.4$ ) with higher density gradients [2, 3, 4, 5] compared with that of the current case, where  $Ma = 0.19$ . According to  $\frac{\Delta\rho}{\rho} \approx \frac{1}{2}Ma^2$ ,  $Ma \ll 1$ , the density

gradient and the resulting angular light beam deflection in our experiment are smaller than the cases mentioned. For arranging a BOS setup that can detect these small deflections, we need to estimate the density gradient and the light beam deflection as well as a proper experiment design to make it visible in the BOS pictures. In the following, the density gradient and the deflection are estimated by corresponding equations. After trying different setups for the experiment, an LED array was used as the background in the BOS experiment and the test setup was designed to have the largest possible refractive index change due to the tip vortices. The experiment was conducted in a windy and stably stratified weather, and the distance between the LEDs was measured at 187 frames per second rate using image processing techniques. The changes in the distances between the LEDs due to the tip vortex have been modelled, and the vortex radius was extracted by comparing the model with experimental data.

### 6.2 Introduction to the Background-oriented Schlieren method

For many years, optical flow visualization techniques have been used to measure density variations in fluids. These methods, like Schlieren photography,

shadowgraphy or laser speckle density photography are based on the refractive index variations due to the density changes. In the standard Schlieren photography, the parallel light beam from the single source passes through the Schlieren object (fluid containing density variations). The refractive index changes distort the parallel light beam, and a system comprising multiple lenses and a cut-off plane is required to build the distorted image of the light source into the recording plane [6]. Another optical density visualization technique is laser speckle density photography that uses laser beams. In this method, an expanded parallel laser beam traverses the flow with a density gradient and the refracted beam is scattered by a ground glass<sup>1</sup> [7]. The scattering makes a laser speckle pattern, which is photographed.

These optical methods need delicate, complicated and expensive optical equipments; thus, they cannot be usually used for large fields of view and are performed mostly in a laboratory or wind tunnel [2]. In contrast to these methods, the BOS method does not need sophisticated optical facilities and provides good qualitative and quantitative information about the density variations [8].

BOS was first introduced by Meier (1999) and Richard et al. (2000) [8]. Dalziel et al. (2000) also presented it under a different title of ‘Synthetic Schlieren’ [9]. This technique uses the refractive index changes due to the density variations to obtain the density distribution in a flow field. BOS has a simple setup that can be applied to different types of the flow fields [2]. In BOS, a camera is focused on a pattern in the background and the flow field with density gradient is located between the camera and the background. The reference image is recorded without the flow field, and the other pictures that are taken within the experiment show a displacement with respect to the reference image due to the refractive index changes [10]. BOS uses the relation between the density gradient and the refractive index variation to build up the density distribution in a compressible flow field.

BOS has successfully been used to study density distribution in supersonic flows with high Mach numbers like shockwaves [11] and supersonic jets [8]. The density gradient increases with Mach number value [2]; thus, BOS works very well in these kinds of flows with high Mach number.

Temperature change is another factor that easily affects the density distribution. The investigation of flames and plumes around burners by means of BOS proves the ability of this technique to study the density distribution in these flows [8, 12]. See Figure 6.1.

---

<sup>1</sup> Ground glass is a glass whose surface has been ground in order to obtain a flat but rough (matte) finish.



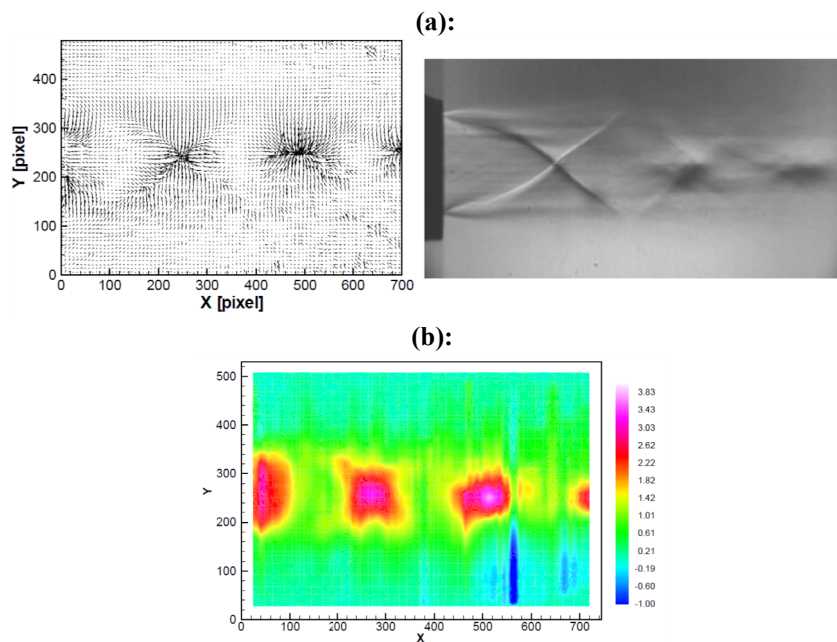


**Figure 6.1:**(a): Left: displacement data proportional to density gradient in x and y directions in a supersonic jet, right: Schlieren picture; (flow from left to right) (b): density distribution of the same jet extracted via BOS [8]

Study of the wakes and tip vortices has been one of the most important interests from the beginning of BOS in 1999. The tip vortices shed from the blade tips in helicopters are critical issues because of their contribution to the blade noise and vibrations, and BOS has shown good capabilities in studying helicopter blade's tip vortices. The helicopter blade tip vortex formation and detailed structure has been studied with promising spatial resolution via BOS in a hovering flight [2,3]. This proves the feasibility of BOS for large scale aerodynamics with considerable decrease of the experiment preparation time.

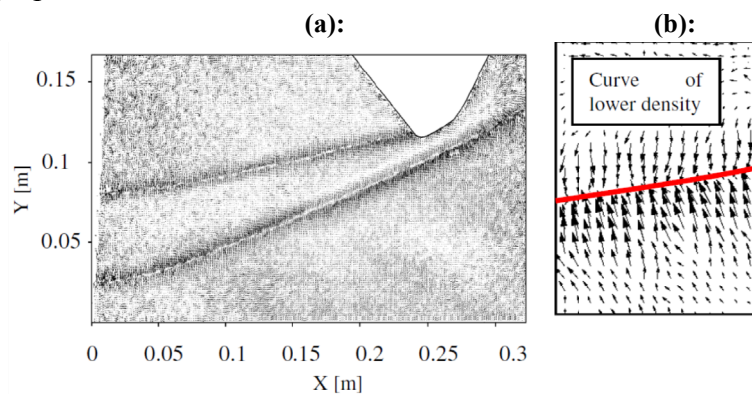


**Figure 6.2:** (a): Displacement vectors field of the tip vortices shed from a helicopter blade for Mach number of  $Ma = 0.46$ ; (b): Close-up view of the structure of the vortex [3]

In Figure 6.2, the displacement in the image of the background due to the density gradient in the vortex core has been extracted by means of the BOS method. Figure 6.2 shows two vortex lines, one of them is produced only by the blade tip and the second one belongs to the other blade that has already passed through the imaging area.

BOS has previously showed good capabilities in qualitative and quantitative investigation of compressible tip vortices and wakes either in wind tunnel [4] or full scale experiments [3]. The vortex line and its evolution in time can be visualized in the BOS results, and other quantitative information such as vortex core size and density distribution can be calculated with good resolution [3,4].

In the next sections, in the first step, the density distribution in a tip vortex is formulated using the 2D Rankine vortex model and an isentropic flow assumption. The refractive index, which is connected to the density by the Gladstone–Dale equation, is formulated as well. In the next step, the equations for the angular beam deflection and image displacement due to the refractive index change (which is obtained in the previous section) are introduced for axisymmetric density distributions. Furthermore, the circulation in the tip vortex is estimated using the actuator disk theory and a few assumptions about vortex size and wind speed; the model for the current tip vortex is then obtained.

In the next sections, several experiments are designed according to the predicted image displacement due to the tip vortex and the model variables are adjusted to fit the experiment results.

### 6.3 Density distribution through the tip vortices

The radial equilibrium component of 2D Navier–Stokes equation in cylindrical coordinate system is:

$$\rho \left( \frac{\partial v_r}{\partial t} + v_r \frac{\partial v_r}{\partial r} + \frac{v_\theta}{r} \frac{\partial v_r}{\partial \theta} - \frac{v_\theta^2}{r} \right) = -\frac{\partial p}{\partial r} + \rho g_r + \mu \left[ \frac{1}{r} \frac{\partial}{\partial r} \left( r \frac{\partial v_r}{\partial r} \right) - \frac{v_r}{r^2} + \frac{1}{r^2} \frac{\partial^2 v_r}{\partial \theta^2} - \frac{2}{r^2} \frac{\partial v_\theta}{\partial \theta} \right] \quad (6.1)$$

where  $p$  is the pressure,  $\rho$  is the density and  $v_r$  and  $v_\theta$  are the radial and tangential velocities, respectively. By assuming inviscid flow ( $\mu=0$ ) and stationary 2D vortex with no radial velocity ( $v_r=0$ ), equation (6.1) reduces to [5]:

$$\frac{\partial p}{\partial r} = \rho \frac{v_\theta^2}{r} \quad (6.2)$$

Considerable heat exchange is not expected through the tip vortex, then the flow is assumed to be isentropic and the pressure is related to the density by the following equation:

$$\left(\frac{p}{p_\infty}\right) = \left(\frac{\rho}{\rho_\infty}\right)^\gamma \quad (6.3)$$

where  $\gamma$  is the specific heat ratio, and  $p_\infty$  and  $\rho_\infty$  are free stream pressure and density, respectively.

The tip vortices of the wind turbine blades are frequently modelled as the Rankine vortex [13-15]. The Rankine vortex is the simplest vortex model that comprises a forced vortex in the central core surrounded by a free vortex in the outer part [16]. The tangential component of the velocity in Rankine vortex is:

$$v_\theta(r) = \begin{cases} \frac{\Gamma_\infty r}{2\pi r_c^2}, & 0 \leq r \leq r_c \\ \frac{\Gamma_\infty}{2\pi r}, & r \geq r_c \end{cases} \quad (6.4)$$

where  $\Gamma_\infty$  is the vortex circulation and  $r_c$  is the vortex core radius. By taking the derivative from both sides of equation (6.3) with respect to  $r$ , the density gradient is formulated as follows:

$$\frac{\partial \rho}{\partial r} = \frac{\rho_\infty^\gamma}{\gamma p_\infty} \frac{\partial p}{\partial r} \rho^{1-\gamma} \quad (6.5)$$

If  $\frac{\partial p}{\partial r}$  in equation (6.5) is replaced according to equation (6.2), the density gradient becomes:

$$\frac{\partial \rho}{\partial r} = \frac{\rho_\infty^\gamma}{r\gamma p_\infty} (v_\theta)^2 \rho^{2-\gamma} \quad (6.6)$$

where  $r_c$  is the vortex core radius.

Finally, if  $v_\theta$  in equation (6.6) is replaced according to equation (6.4), the final equation for the density gradient is obtained as:

$$\frac{\partial \rho}{\partial r} = \begin{cases} \frac{r \rho_{\infty}^{\gamma}}{p_{\infty} \gamma} \left( \frac{\Gamma_{\infty}}{2\pi r_c^2} \right)^2 \rho^{2-\gamma}, & 0 \leq r \leq r_c \\ \frac{\rho_{\infty}^{\gamma}}{p_{\infty} \gamma r^3} \left( \frac{\Gamma_{\infty}}{2\pi} \right)^2 \rho^{2-\gamma}, & r \geq r_c \end{cases} \quad (6.7)$$

## 6.4 Angular deflection and displacement due to the density gradient

In a BOS experiment, a pattern is placed behind the medium with density gradient; hence, the refractive index change leads to some displacements of the pattern image. The angular deflection due to the axisymmetric refractive index gradient is obtained by equation (6.8). The axis of symmetry is perpendicular to the light rays [17].

$$\varepsilon(y) = 2y \int_y^{\infty} \frac{d\delta}{dr} \frac{dr}{(r^2 - y^2)^{1/2}} \quad (6.8)$$

where  $\delta = n - 1$  and  $n$  is the refractive index that is related to the density by Gladstone–Dale equation:

$$\frac{n-1}{\rho} = G(\lambda) \quad (6.9)$$

where  $G(\lambda)$  depends on the medium property and weakly on the wavelength of light [17]. For air,  $G$  is equal to constant value of  $k = 2.3 \times 10^{-4}$ . Hence, equation (6.8) turns into:

$$\varepsilon(y) = 2ky \int_y^{\infty} \frac{d\rho}{dr} \frac{dr}{(r^2 - y^2)^{1/2}} \quad (6.10)$$

For small angle deflections,  $\varepsilon$  can be easily related to displacement in the pattern image ( $\Delta y$ ) and in the pattern itself ( $\Delta y'$ ) by the following equations [11]:

$$\varepsilon = \frac{\Delta y Z_B}{Z_D Z_i} \quad (6.11)$$

$$\varepsilon = \frac{\Delta y'}{Z_D} \quad (6.12)$$

where  $Z_B$ ,  $Z_D$  and  $Z_i$  are the distances between the background and the camera, between the density gradient field and background and between the image and the lens, respectively. These geometrical parameters are shown in the BOS setup in Figure 6.3.

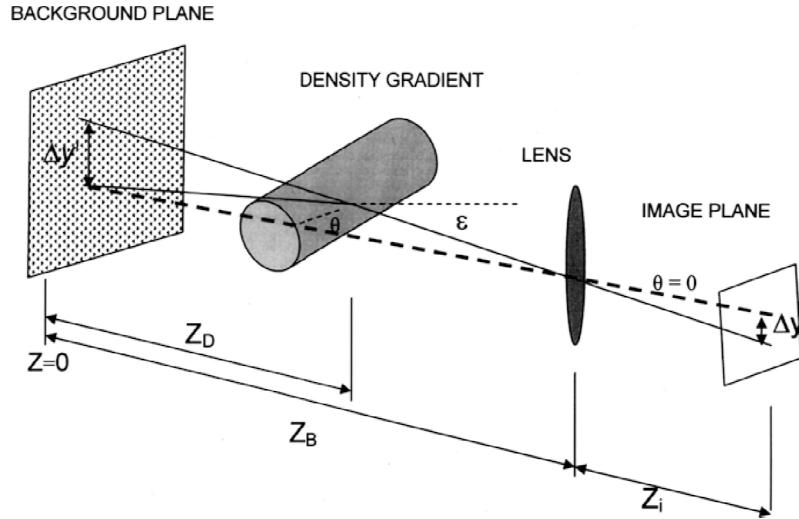


**Figure 6.3:** BOS setup [11]

For large  $Z_B$  values,  $Z_i$  can be replaced by  $f$  and equation (6.11) will be:

$$\varepsilon = \frac{\Delta y Z_B}{Z_D f} \quad (6.13)$$

where  $\Delta y$  is the displacement due to the density on the camera sensor. If the effective pixel size on the camera chip is equal in the horizontal and vertical directions ( $s_x = s_y$ ), the pixel displacements in the image will be:

$$\Delta y_{pix} = \frac{Z_D f \varepsilon}{Z_B s_x} \quad (6.14)$$

Therefore, the final equations for pixel displacement are derived. These equations will be used in the next sections to model the changes in the pattern image because of the density gradient in the tip vortex.

## 6.5 Density and displacement estimation in a tip vortex

For estimating the density distribution within the tip vortex, we need to estimate the circulation and vortex core diameter. For a crude estimation of the circulation, a closed loop is assumed in one pitch of the tip vortex behind the turbine (Figure 6.4).

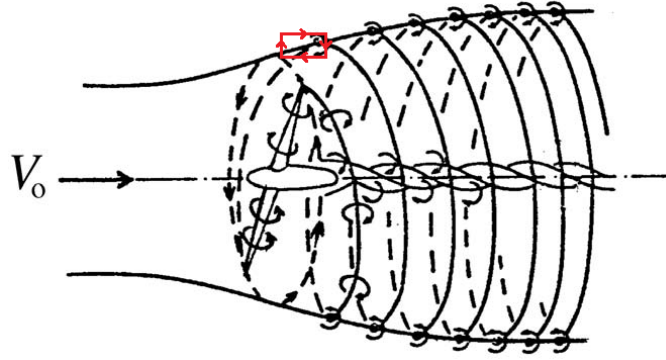


**Figure 6.4:** Rectangular loop in a vortex pitch [18]

The circulation is given by

$$\Gamma = \oint \vec{U} \cdot d\vec{l} \quad (6.15)$$

For the current closed loop in Figure 6.4, velocity on the upper side is equal to free stream wind speed  $V_0$ , and on the lower side, it is equal to the wind velocity in the turbine wake  $u$ .

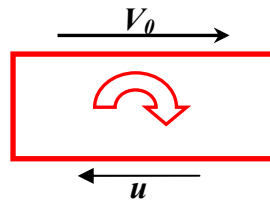


**Figure 6.5:** Velocities on the rectangular loop sides in a vortex pitch

As the velocities on the two other sides of the closed loop are perpendicular to the sides, the circulation according to equation (6.15) is given by:

$$\Gamma = \oint \vec{U} \cdot d\vec{l} = lV_0 - lu = l(V_0 - u) = l\Delta u \quad (6.16)$$

where  $\Delta u$  is defined as the velocity deficit and  $l$  is the vortex pitch. Regarding the actuator disk theory (momentum theory), the wind velocity in the turbine wake is:

$$u = (1 - a)V_0 \quad (6.17)$$

where  $a$  is the axial induction factor [18]. As the turbine has three blades, the vortex moves three pitches in each cycle of rotation; thus, the pitch length is:

$$l = u \frac{T}{3} \xrightarrow{r = \frac{60}{\omega}} l = \frac{20u}{\omega} \quad (6.18)$$

where  $T$  is the time period of the turbine rotation and  $\omega$  is the turbine rotational speed in  $rpm$ .

In this chapter, the tip vortices that are shed from the Nordtank turbine blades are going to be studied. The rotor diameter is  $41\text{ m}$ , and the turbine is ideally rotating with  $27\text{ rpm}$ . For the first try, as it can be seen in Figure 6.6 and Figure 6.7, the pattern that includes 100 horizontal lines with a distance of  $1\text{ cm}$  and 5 vertical lines, each  $10\text{ cm}$  apart, was installed on the turbine tower that is  $2.9\text{ m}$  away from the blade tip.



**Figure 6.6:** First position of the pattern in BOS test

As the turbine is  $35\text{ m}$  tall and the rotor diameter is  $41\text{ m}$ , the distance between the camera and pattern is large; hence, a telephoto lens with the focal length of  $300\text{ mm}$  was chosen for photographing the pattern. The camera was placed about  $30\text{ m}$  away from the turbine to obtain a high resolution image that only includes the pattern.



**Figure 6.7:** Position of the pattern while the blade is passing in front of it

If the axial induction factor and free stream wind speed are assumed to be  $a = \frac{1}{3}$  and  $V_0 = 8\text{ m/s}$ , then according to equations (6.17), (6.18) and (6.16),  $u = 5.33\text{ m/s}$ ,

$l = 3.95 \text{ m}$  and  $\Gamma = 10.53 \text{ m}^2 / \text{s}$ , respectively. With a rough estimation, the vortex core diameter is also assumed to be 10 cm according to the flow visualization done on a 100 KW wind turbine [19]. See Figure 6.8.

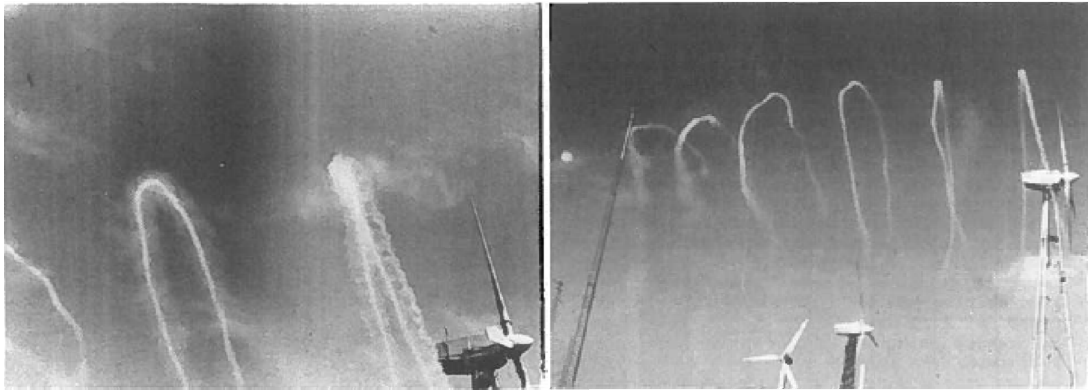


**Figure 6.8:** The smoke emitted from the tip in wind speed 6–8 m/s [19]

Density and density gradient in the tip vortex for the current experiment design are calculated by equation (6.7).

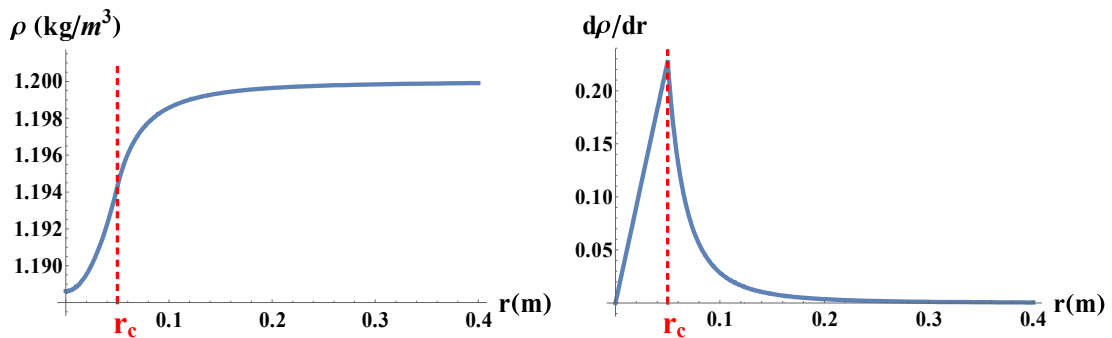


**Figure 6.9:** Density and density gradient in the tip vortex

Figure 6.9 shows that the density grows faster through the vortex core than outside the core and it has the minimum value in the vortex centre.

The angular deflection and displacement is now obtained by equations (6.10) and (6.13), as shown in Figure 6.10.

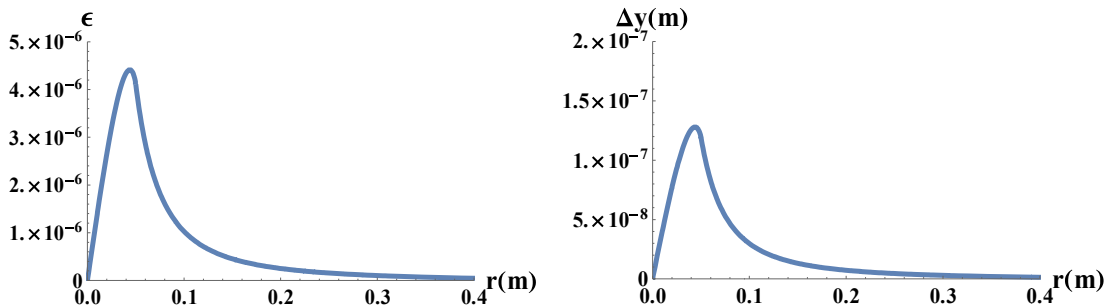


**Figure 6.10:** Angular deflection and displacement in the tip vortex



$\Delta y$  is the displacement due to the density change of the vortex on the camera sensor. The pixel size on the current Basler camera (that was used in chapter 3 and 4) sensor is  $5.5 \mu m$ ; therefore, the pixel displacements in the image is given in Figure 6.11.

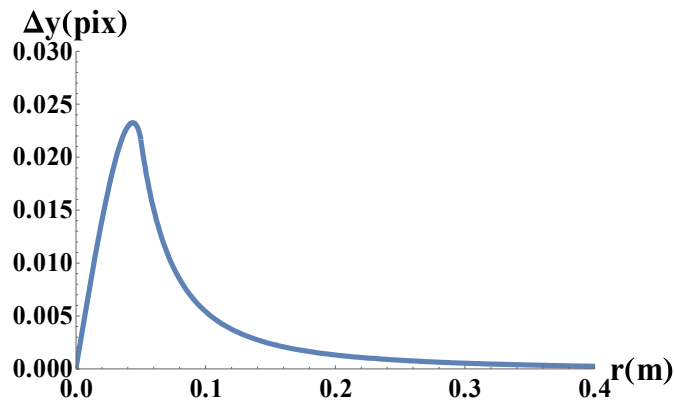


**Figure 6.11:** Displacement in the image plane for the first experiment design

As it is obvious in Figure 6.11, the pixel displacement in the image is less than 0.025 pixel that discovering this small value in the image is an experimental challenge. Hence, in the next section, we try to design a new setup with larger possible displacement in the image plane.

## 6.6 New setup

The vortex properties, such as core size and the pressure drop inside the tip vortex core, are not yet well defined in the real experiment, and it is more likely that the tip vortices have larger diameter or less circulation which lead to even smaller displacement in the image plane. Equation (6.14) shows that  $\Delta y$  will increase with  $Z_d$ ; hence, we need to increase the distance between the tip vortex and the poster to make a larger pixel displacement in the image. In the new setup, the background pattern was horizontally placed on the nacelle while the camera was on the ground to look at the pattern with a small angle. The poster was installed under a balcony behind the nacelle (Figure 6.12) with  $Z_d$  about the blade length (20.5 m).

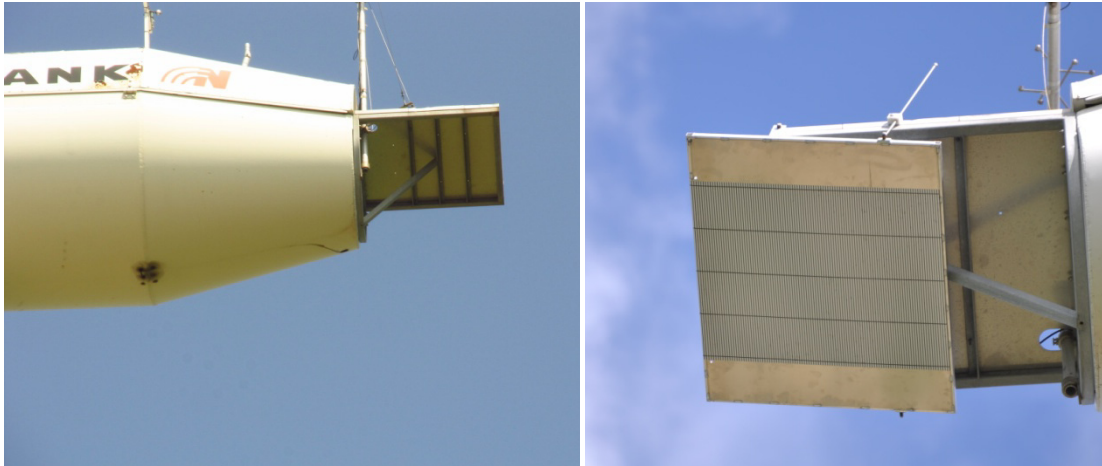


**Figure 6.12:** The new placement of the pattern

By assuming experimental conditions that is mentioned in section 6.5 ( $a = \frac{1}{3}$ ,  $V_0 = 8 \text{ m/s}$  and  $\omega = 27 \text{ rpm}$ ) for the current setup, the pixel displacement due to a tip vortex with 10 cm diameter is estimated, as shown in Figure 6.13.

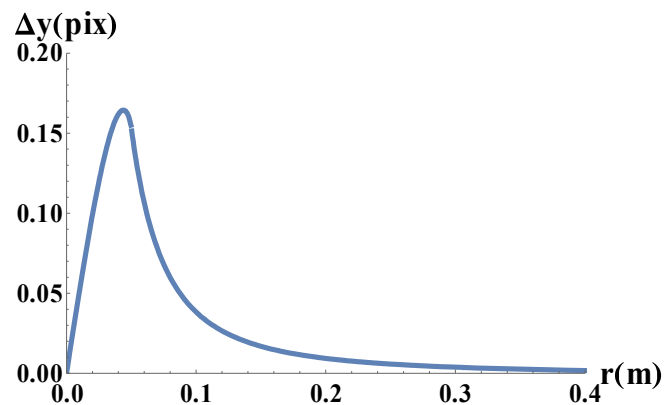


**Figure 6.13:** Displacement in the image plane for the second experiment setup

As shown in Figure 6.13, the predicted pixel displacement in the current experiment design increased by about 7 times.

The experiment was conducted with the new setup by taking the images at 187 frames per second during a day with a predicted wind speed of 8-10  $\text{m/s}$ . However, after analysing the images, the BOS effect was not detected. As the density change due to the turbine tip vortices is not as strong as the high Mach number tip vortices, the vortices can be washed away by the relatively high turbulence. To avoid this effect, the experiment was planned to be conducted again during the night when the atmosphere is more stable due to the lack of heating of the ground by the sun. Therefore, a  $100 \times 10$  LED array was designed as the pattern in the BOS experiment (Figure 6.14).



**Figure 6.14:** LED array designed for the BOS experiment

The exact dimensions of the LED array are shown in Figure 6.15.

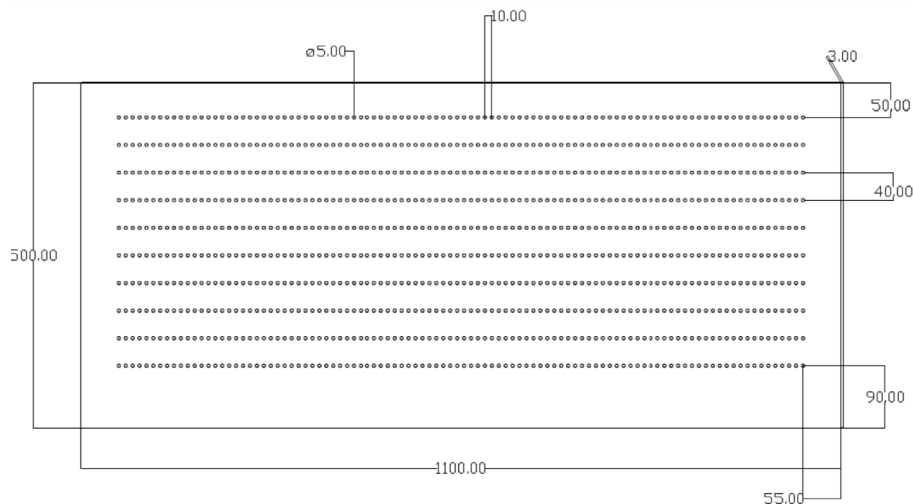


**Figure 6.15:** Dimensions of the LED array in millimetres

Regarding the expected helical path of the tip vortex propagation, the largest density gradient due to the vortices will more likely appear perpendicular to the rotor plane. Thus, the distance between the LEDs is smaller in this direction to catch the refractive

index changes.

The camera should take pictures of the LED array from the side to prevent falling in the tower wake because the wake destroys the tip vortex. However, if the LEDs are photographed from the side and from a relatively small distance, the scatter of the light around them will blur their images, as shown in Figure 6.16.

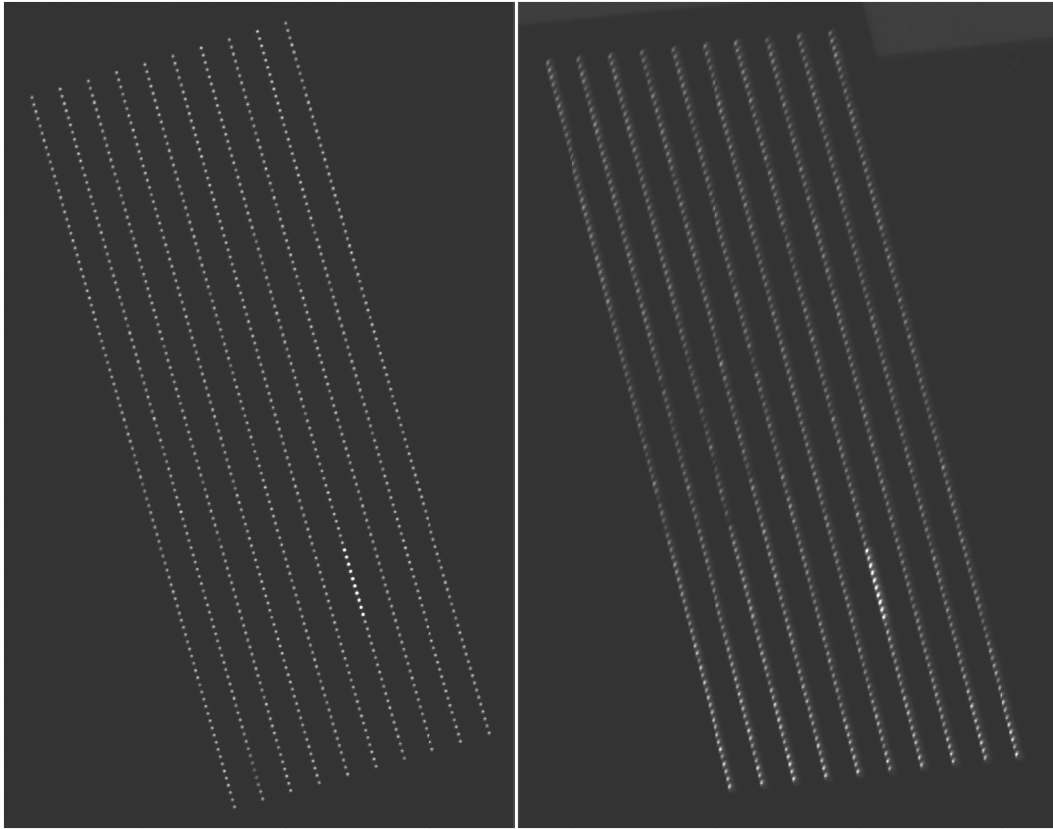


**Figure 6.16:** The left picture is taken from below the array and the right picture is taken from the side with the same exposure time of  $5 \text{ ms}$ <sup>1</sup>

The distance between the camera and turbine was increased to avoid the light scattering problem around the LEDs. In the new experiment setup,  $z_B \approx 42 \text{ m}$ , and the camera took 187 frames per second of the pattern. The exposure time was  $5 \text{ ms}$  and the focal length was chosen to be  $300 \text{ mm}$ .

---

<sup>1</sup> There are 10 LEDs brighter than others that is due to the Electrical circuits builder.



Figure 6.17: Final experiment setup

By taking the same assumptions as before ( $a = \frac{1}{3}$  and  $V_0 = 8 \text{ m/s}$  and  $\omega = 27 \text{ rpm}$ ), the expected pixel coordinates are plotted in Figure 6.18.

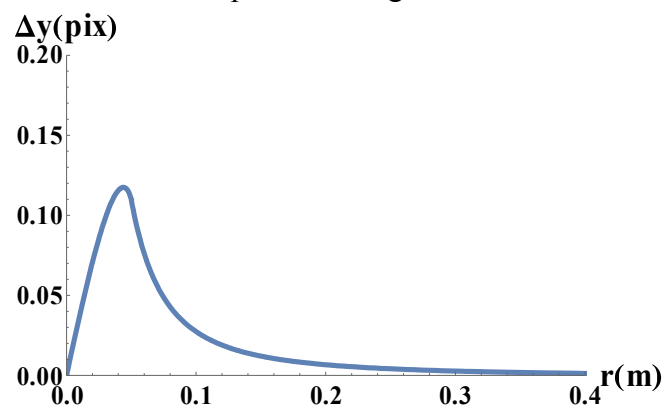


Figure 6.18: Displacement in the image plane for the last experiment setup with LED array

## 6.7 Estimation of the tip vortex parameters

According to the weather forecast, a night with a reasonably high wind speed and

stable weather condition was chosen for conducting the experiment (predicted maximum wind speed value of 8–10 m/s). In addition, the predicted wind profiles in different heights were convincingly apart, which indicates a stable atmospheric condition.

The turbine was locked during the experiment to avoid yawing, and 4000 images were taken to investigate the tip vortex characteristics.

Figure 6.19 shows one of the images taken from the LED array during the experiment.

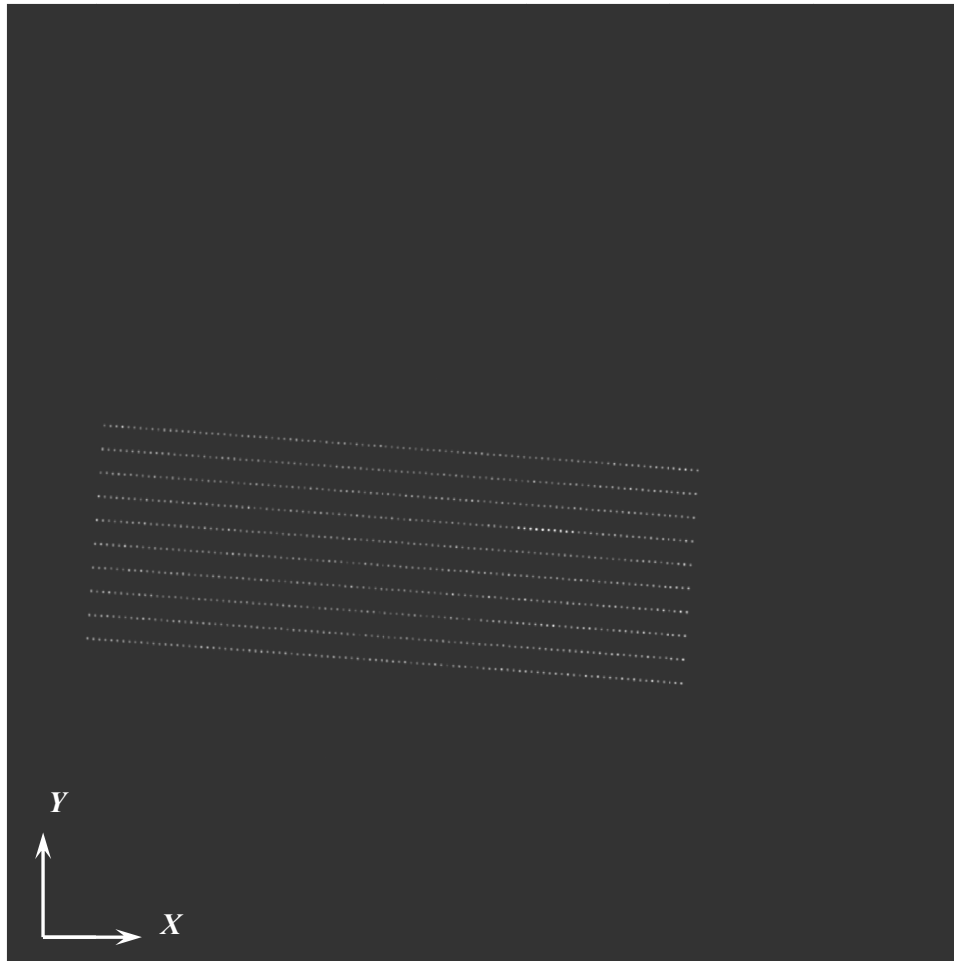


**Figure 6.19:** One of the 4000 images in the BOS experiment

The position of each of the LEDs was defined as follows:

- 1- The corners of the LED array were identified
- 2- The approximate position of each points was found using interpolation between corner points
- 3- A window was made around the approximate position of each LED
- 4- The final position of the LED was defined using the intensity median of each window.

The first set of images was taken with the turbine stopped as reference images. Then,



the turbine yawed towards the wind and started running. After reaching the stable rotational speed, it was locked during the photography in the second set. After the turbine yawed, the LED frame shifted in the image plane and the relative distances between the LEDs changed due to the changes in the location of the LED array and viewing angles. Therefore, the position of the LEDs in the two sets of the images will not be accurately comparable for the vortex characterization. Accordingly, instead of comparing the images with the reference images, the distance between the LEDs in the same image set is studied. It is expected that the effect of the tip vortex travelling through the LEDs will be observed.

Investigation of the distance between the LED rows starts with the estimation of the expected vortex direction in the images. To estimate the vortex line direction, the vortex path is modelled as a helix with the following parametric equation of  $S(t, u)$  :

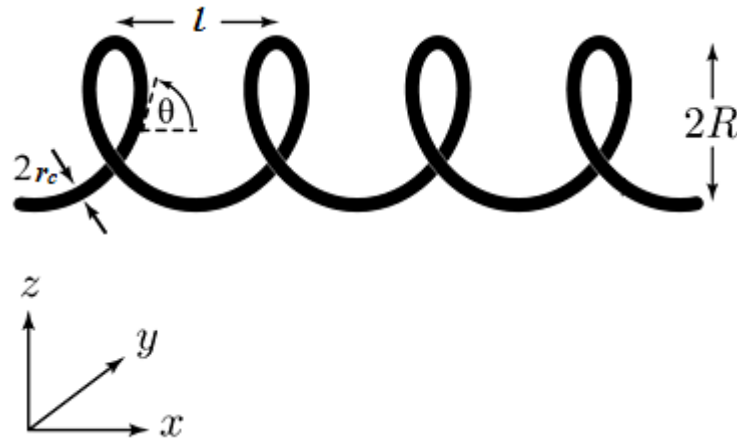


**Figure 6.20:** Helix geometry

$$\begin{aligned}
 S(t, u) &= \vec{r}(t) + a\vec{n}(t) \cos u + a\vec{b}(t) \sin u \\
 \vec{r}(t) &= (ht, R \cos t, R \sin t) \\
 \vec{n}(t) &= (0, -\cos t, \sin t) \\
 \vec{b}(t) &= \frac{1}{\sqrt{R^2 + h^2}} (R, h \sin t, -h \cos t)
 \end{aligned}
 \tag{6.19}$$

Where  $h = l / 2\pi$  and  $R$  is the helix radius. According to the data from the closest met mast, averaged yaw error during the experiment was about  $10^\circ$ <sup>1</sup>; thus, the tip vortex will rotate around the propagation axis of the helix that is now deviated  $10^\circ$  from the rotor axis.

The yaw error was relatively high and for such a high yaw error the tip vortex will not be a helix anymore, but will instead have a more complicated geometry where the tip

<sup>1</sup> The turbine was locked to yaw towards the wind direction during the measurement, and it leads to a large yaw error.

vortices travel on ellipses instead of circular rings. However we assumed the tip vortex path as a helix with several simplifications. The deviated helical path of the tip vortex for the averaged wind speed of  $7.5 \text{ m/s}$ , the rotational speed of  $2 \text{ rpm}$ <sup>1</sup> and the induction factor of  $1/3$  are plotted in Figure 6.21.

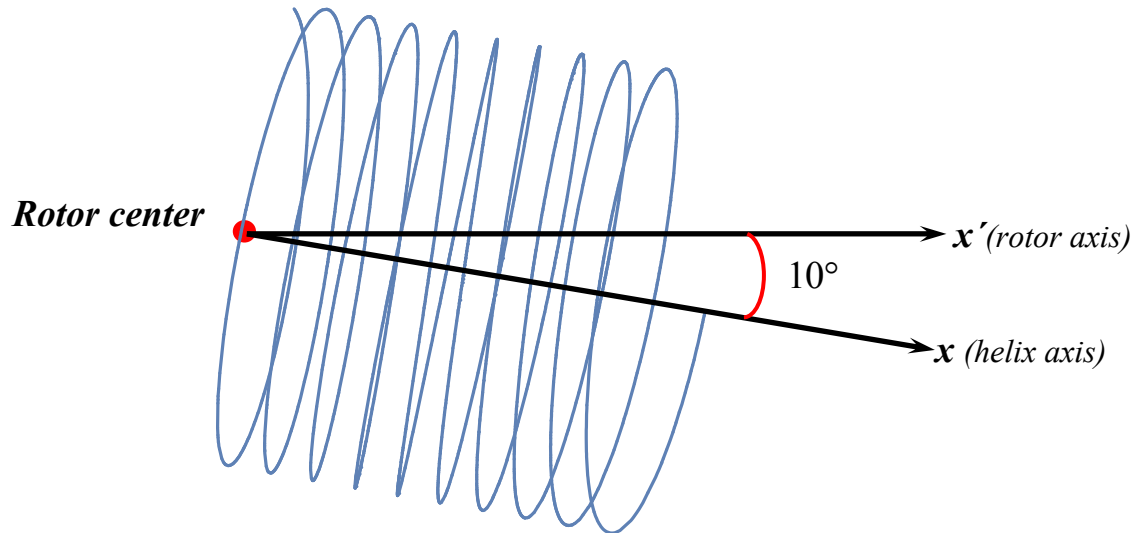


**Figure 6.21:** Top view of the deviated helix (for  $r_c = 0$ ) because of the yaw error

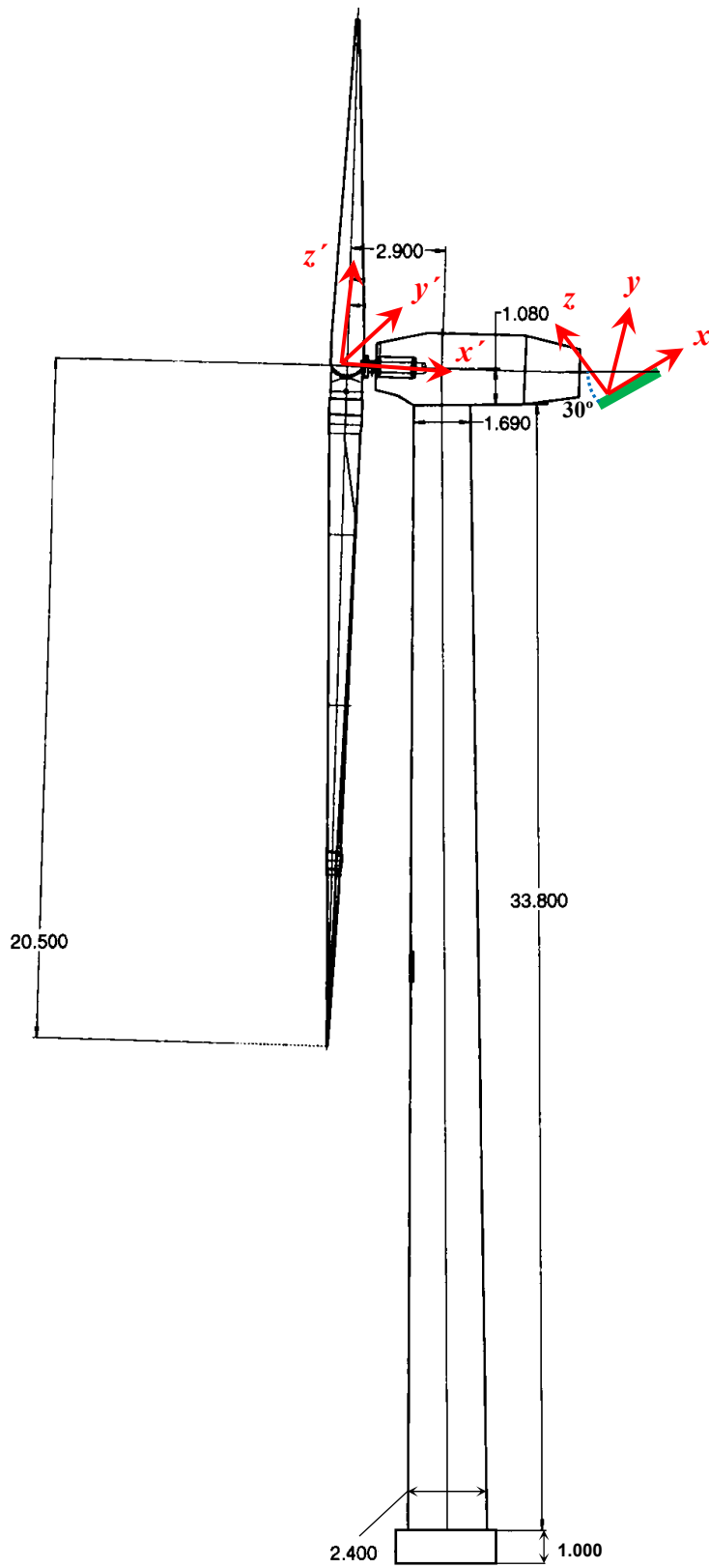
The vortex line direction in the image was estimated in the following steps:

- 1- The camera is calibrated using the LED array as the calibration board (the calibration process has been explained in section 3.5.1).
- 2- The transformation matrices (translation and rotation) between the turbine coordinate system ( $x',y',z'$ ) and the LED array coordinate system ( $x,y,z$ ) are found according to the geometrical setup (see Figure 6.22).
- 3- The helix equation that is written in the turbine coordinate is translated to the LED array coordinate system using the transformation matrices obtained in step 2-.
- 4- The helical path of the tip vortex in the LED array coordinate system is projected on to the image using the calibration matrices calculated in step 1-.

---

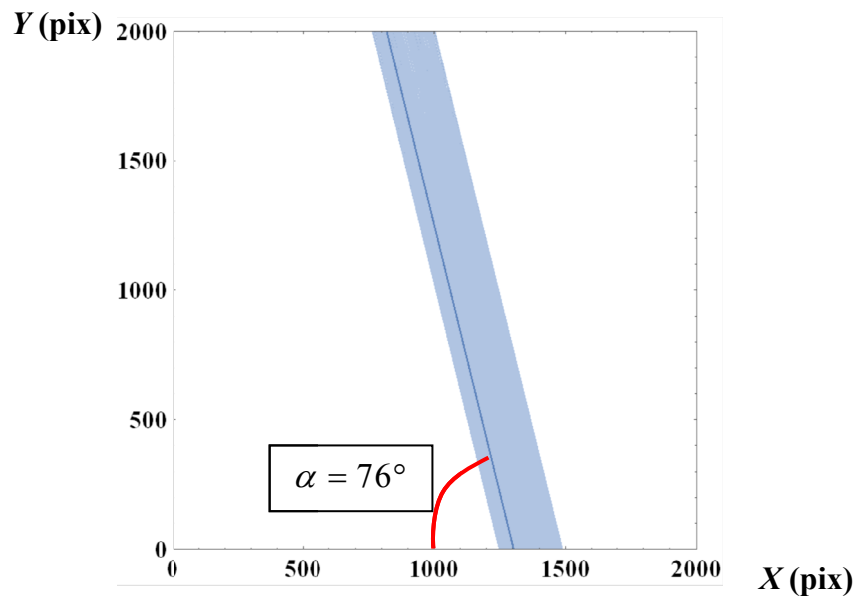
<sup>1</sup> The averaged wind speed and turbine rotational speed are measured during the BOS experiment. It will be explained in more detail in the following section.





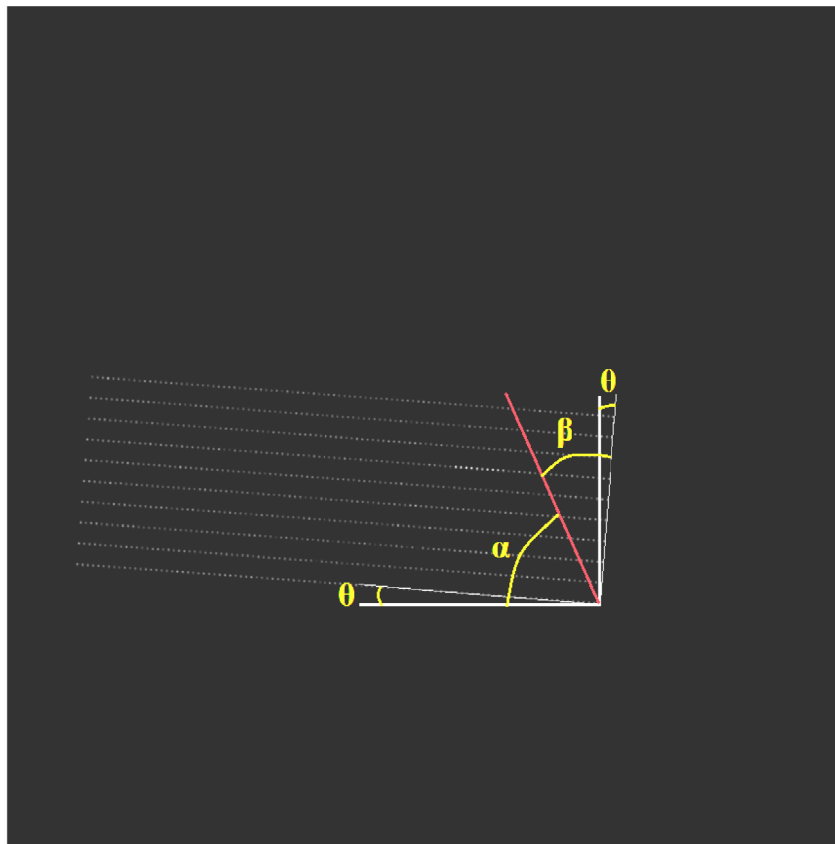
**Figure 6.22:** Turbine coordinate system  $(x', y', z')$  and the LED array coordinate system  $(x, y, z)$

Figure 6.23 shows the projected vortex line on to the image plane for  $r_c = 5$  cm, wind speed of 7.5 m/s, induction factor of 1/3 and the rotational speed of 27 rpm.



**Figure 6.23:** Estimated vortex line direction in the image plane

Then, the following angles that are shown in Figure 6.24 are identified.



**Figure 6.24:** Angles between projected vortex line (Red line) with LED array edges

From the positions of the LED array corners,  $\theta = 4^\circ$  and  $\beta = 90 - (\alpha - \theta) = 18^\circ$ . By knowing the above angles, the distances between the LEDs are averaged along the estimated projected vortex line, and this averaged value will be studied during the time of experiment.

After finding the projected vortex line in the image, the positions of LEDs that are in the same direction with the vortex line were stored in a matrix. Yellow lines in Figure 6.25 represent the vortex line direction in the image. The coordinates of the coincidence points of each of the yellow lines with the LEDs are saved in the new matrix rows.

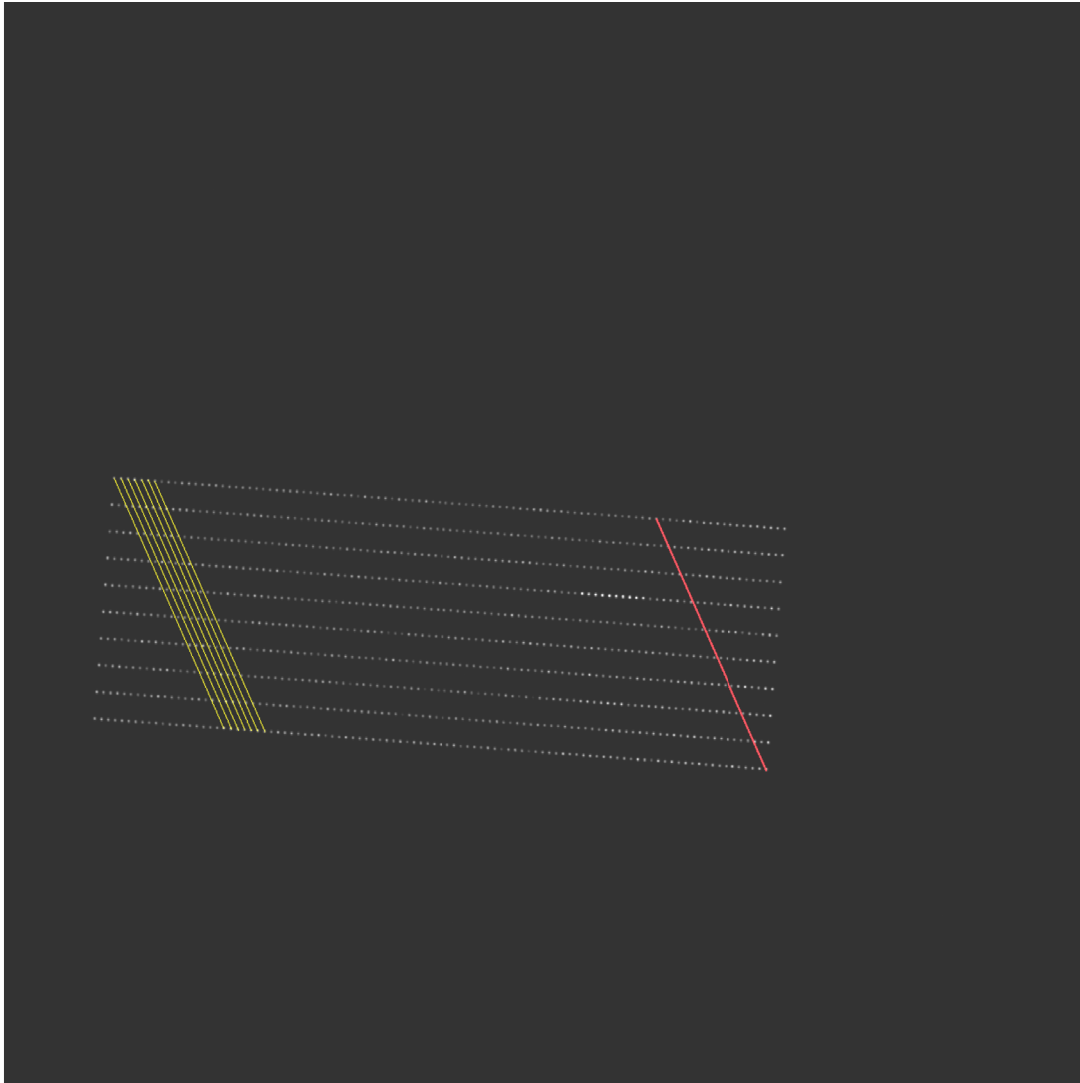


**Figure 6.25:** Yellow: the first seven lines parallel to the vortex line, Red: vortex line direction

The distance between each LED in each of the matrix rows is calculated with respect to the other LED in the same column but 30 rows apart. Finally, the LED distances are averaged over the columns that indicate the vortex direction. Figure 6.26 shows

the averaged distance between the LEDs that are 30 rows apart minus its averaged value in time.

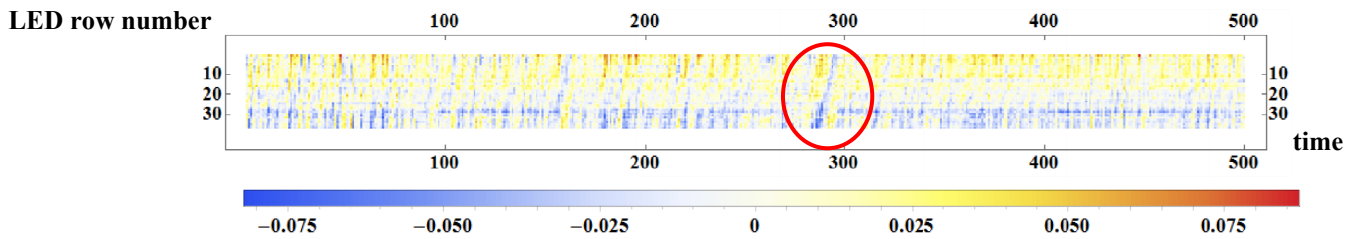


**Figure 6.26:** the colour of the plot indicates the distance between the LEDs 30 rows apart minus its averaged value in pixels. The vertical axis is the LED row number whose distance is presented from the other LED row 30 rows apart and the horizontal axis is time with intervals of  $1/187$  s

In Figure 6.26, there is a line around time of  $300/187$  s which indicates that the distance between the LEDs has successively changed, and it seems that a tip vortex has been passing the LED plate.

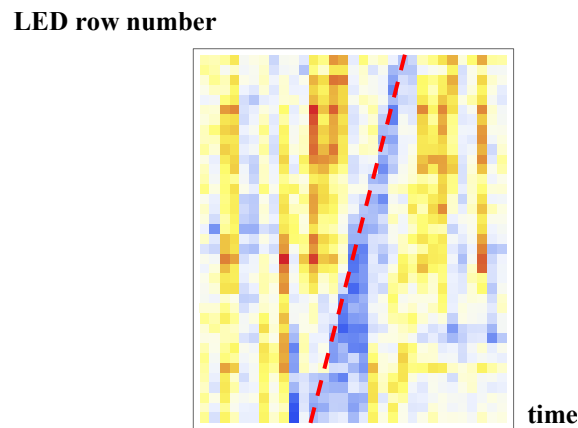


**Figure 6.27:** Zoomed picture of the area highlighted by a red ellipse in Figure 6.26. Red dashed line shows the vortex passing the LED plate in time

The changes of the averaged LED distance around the red dashed line (Figure 6.27) are calculated for each row number. These changes are averaged over the LED rows, as shown in Figure 6.28.

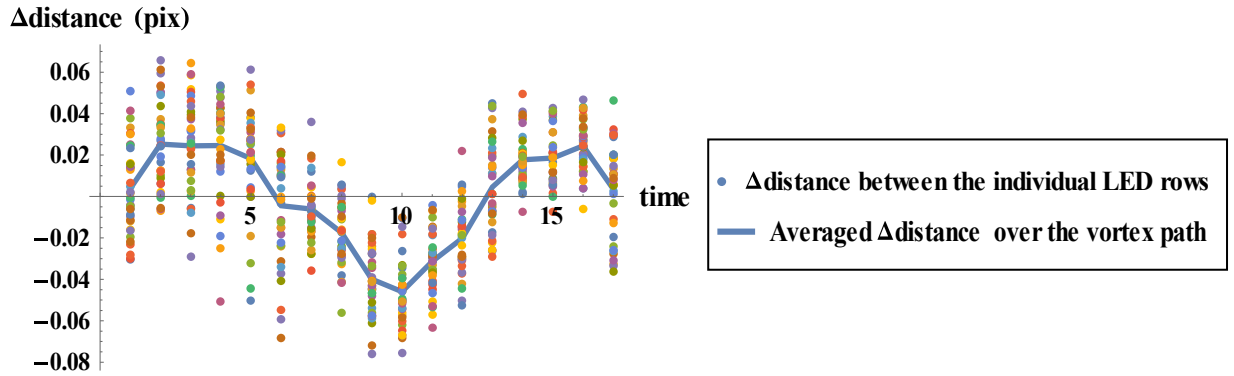


**Figure 6.28:** LED distances around the vortex path. Time step on the horizontal axis is  $1/187 s$ .

Blue curve in Figure 6.28 shows that the distance between the LEDs started to change when the vortex started travelling over the LEDs and returned to the previous value when the vortex went out of the area between two LEDs. In the meantime, the vortex travels the distance between the LEDs (which are 30 rows apart) in addition to the tip vortex diameter. Therefore, the vortex speed can be estimated by dividing the distance that it travels since it enters the area between two LEDs till it goes out of it by the travelling time.

For estimating the vortex pitch and circulation, the instantaneous wind speed in the measurement time is needed. The wind speed and the temperature in different heights were measured by the measurement system on the closest met mast to the Nordtank turbine:

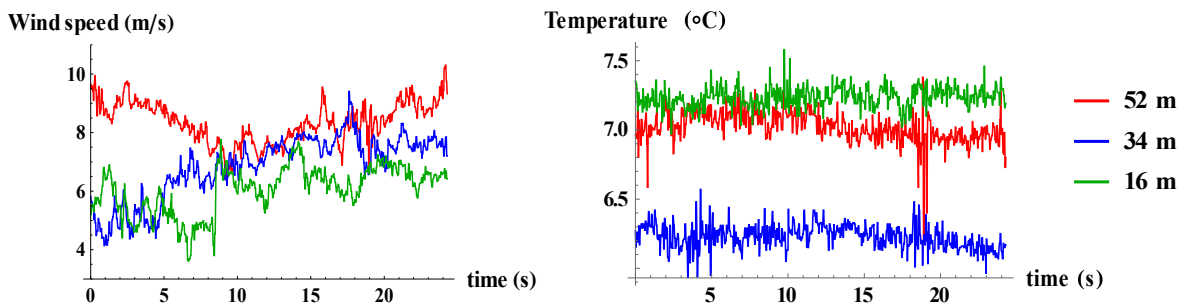


**Figure 6.29:** Wind speed and temperature in different heights were measured by the measurement system on the closest met mast to the Nordtank turbine almost during the experiment time

As the measurement system is not exactly synchronized with the current image acquisition system, instead of using instantaneous wind speed, the averaged wind speed around  $300/187 s$  was used and it was found to be  $V_0 = 7.5 m/s$ . The averaged rotational speed of the turbine during the experiment was around  $27 rpm$ .

By having vortex pitch, circulation and the yaw error, an iterative procedure has been designed to estimate the vortex radius:

- 1- Assuming an initial value for  $r_c$ ; in the current case, it is  $r_{c_0} = 5 cm$ .

- 2- Estimating the projected vortex core radius in the image, as shown in Figure 6.30.

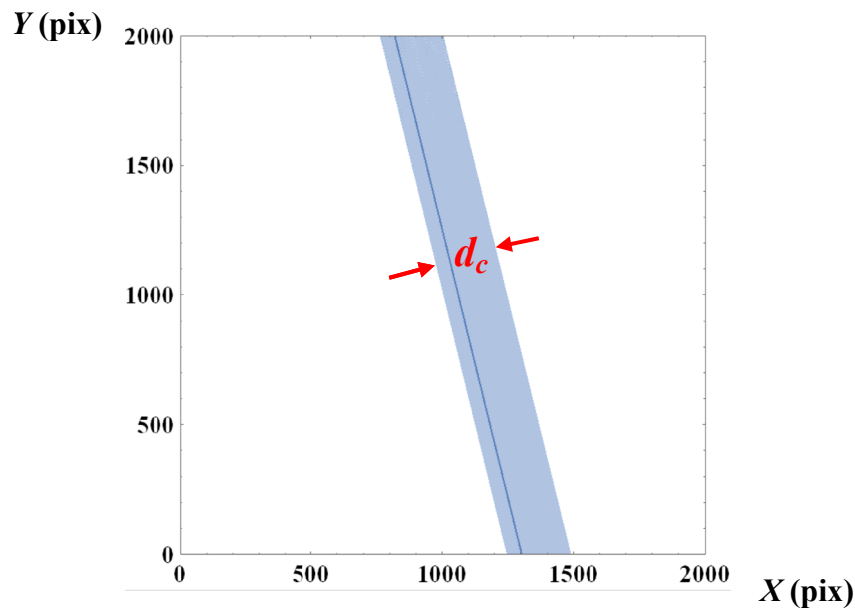


**Figure 6.30:** Projected vortex core diameter  $d_c$

- 3- By having circulation and  $r_c$ , the pixel displacements in the image can be estimated using the procedure explained in section 6.5.
- 4- The changes of the distance between two LEDs is modelled when the vortex is passing one of them
- 5- The distance between two LEDs with 30 intervals is modelled when the tip vortex starts travelling from one LED and goes out from the other one with the estimated speed of  $u$  that changes with  $r_c$ , for example, for  $r_{c_0} = 5 \text{ cm}$ ,  $u = 4.81 \text{ m/s}$ .
- 6- The model from step 5 is compared with the experimental changes (blue dots in Figure 6.31) and all the steps will be iterated for different values of  $r_c$  to get a good match between the model and the experimental data.

As it has been mentioned in step 1, the iterative procedure starts with an initial value of  $r_{c_0} = 5 \text{ cm}$ , and finally, in  $r_c = 10 \text{ cm}$ , it reaches a relatively good agreement between the modelled and experimental distance.

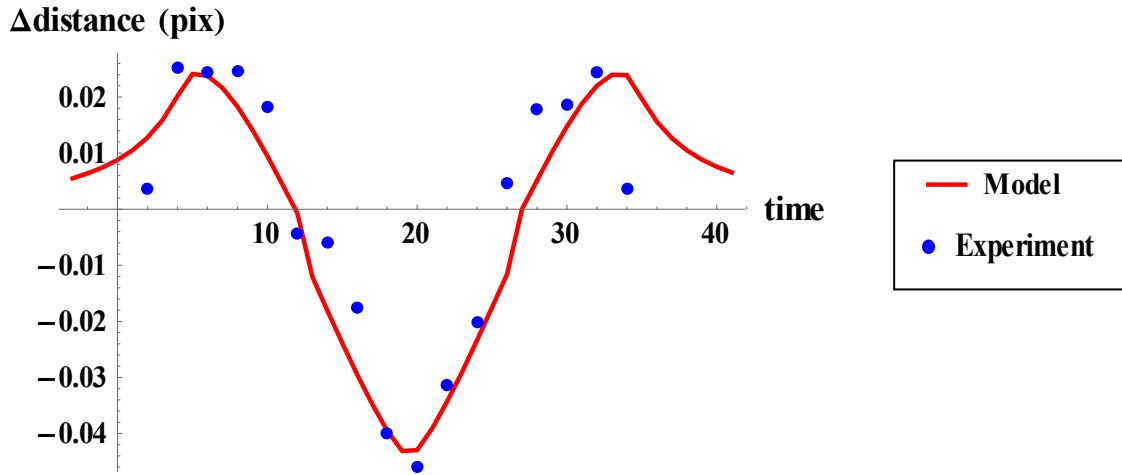


**Figure 6.31:** The modelled and experimental distance between two LEDs 30 intervals apart for  $r_c = 10 \text{ cm}$ . Time step on the horizontal axis is  $1/(2 \times 187) \text{ s}$ .

Therefore, the final vortex speed is  $u = 4.81 \text{ m/s}$ , the velocity deficit will be  $\Delta u = V_0 - u = 2.69 \text{ m/s}$  and the pitch and circulation are  $l = \frac{1}{2} V_0 \frac{T}{3} = 3.56 \text{ m}$  and

$\Gamma = l \Delta u = 9.58 \text{ m/s}^2$ , respectively.

Finally, from the model, the density distribution in the tip vortex is found and plotted in Figure 6.32.

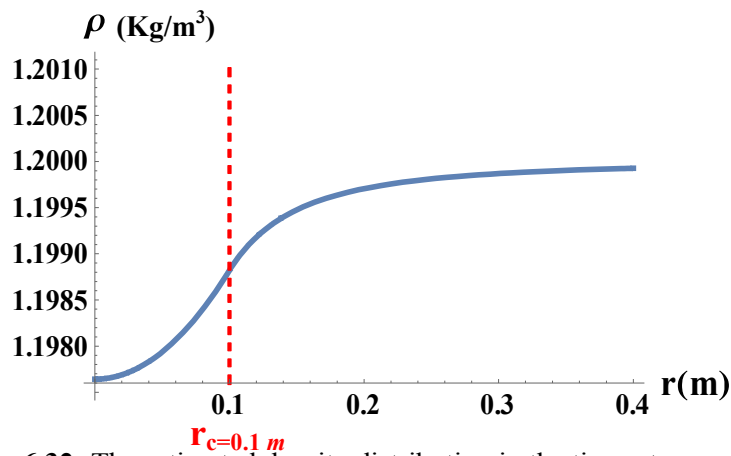


**Figure 6.32:** The estimated density distribution in the tip vortex

The minimum pressure appears at the centre of the vortex; thus, the maximum pressure drop is calculated by replacing the estimated density in the vortex centre in equation (6.3):

$$\Delta p = p_\infty - p_\infty \left( \frac{\rho}{\rho_\infty} \right)^\gamma = 279 \text{ Pa}$$

We expect to observe repeating vortex lines in the experimental results which change the distance between the LEDs in a periodic manner; however, only one vortex line is

pronounced during the measurement time. The final pressure drop drop which is about 0.003 atm, shows that the tip vortices in the current case are relatively weak; hence, the reason for not seeing the tip vortices regularly in the images can be that they are washed away and distorted by the turbulence before they are captured by the camera. However the density change due to the turbulent velocity fluctuations that are normally about 0.2 m/s, is quite small compared with the current case with the tip speed of about 60 m/s, hence according to  $\frac{\Delta\rho}{\rho} \approx \frac{1}{2}Ma^2$ ,  $Ma \ll 1$ , it does not interfere with vortex density gradient.

## 6.8 Conclusion

The BOS method was applied to study the turbine tip vortices behind a Nordtank wind turbine. A preliminary estimation was used to determine the refractive index change due to the turbine tip vortices in the BOS test and a setup was chosen so as to have detectable displacements in the image due to the tip vortex. The BOS experiment was conducted in windy and stratified stable weather condition. A model was devised to estimate the changes of the distance between LEDs due to the tip vortex passing, and the vortex parameters were estimated by comparing the results from the experiment and the model output. The pressure drop in the vortex centre was also calculated using the estimated density distribution in the vortex core. Therefore, the turbine tip vortex was found to have a core diameter of 20 cm and a maximum pressure drop of 279 Pa.



## References

- [1] Dobrev, I., Maalouf, B., Troldborg, N., and Massouh, F. (2008): Investigation of the Wind Turbine Vortex Structure, 14th Int on Application of Laser Techniques to Fluid Mechanics, Lisbon, Portugal.
- [2] Richard, H., and Raffel, M. (2001): Principle and Application of the background Oriented Schlieren (BOS) Method, pp. 1576-1585, Journal of Measurement Science and Technology 12.
- [3] Hernandez, R., Heine, B., Schneider, O., Chernukha, P., and Raffel, M. (2013): Visualization and Computation of Quantified Density Data of the Rotor Blade Tip Vortex, pp. 321-329, Notes on Numerical Fluid Mechanics and Multidisciplinary Design 121.
- [4] Klinge, F., Krimse, T., and Kompenhans, J. (2003): Application of Quantitative Background Oriented Schlieren (BOS): Investigation of a Wing Tip Vortex in a Transonic Wind Tunnel, Proceedings of PSFVIP-4, Jun 3-5, Chamonix, France.
- [5] Bagai, A., and Gordon Leishman, J. (1993): Flow visualization of Compressible Vortex Structures Using Density Gradient Techniques, pp. 431-442, Journal of Experiments in Fluids 15.
- [6] Elsinga, G. E. (2003): Master of Science Thesis: Density Measurement by means of Schlieren Methods: Assessment and Application of Calibrated color Schlieren and Background Oriented Schlieren,
- [7] Lira, T. H., and Keller, R. H. (1994): Reconstruction of an axisymmetric refractive index distribution using speckle photography, pp. 493-502, Proceedings Of SPIE 2340, The International Society For Optical Engineering, Vol. 2340, December 1994.
- [8] Richard, h., et al (2002): Demonstration of the Applicability of a Background Oriented Schlieren (BOS) method, pp. 145-156, Journal of Laser Techniques for Fluid Mechanics.
- [9] Dalziel, S. B., Hughes, G. O., Sutherland, B. R. (2000): Whole-field density measurements by 'synthetic schlieren', pp. 322-335, Journal of Experiments in Fluids 28.
- [10] Richard, H., and Raffel, M. (2001): Background Oriented Schlieren Demonstrations, Final Report for the European Research Office Edison House, Deutsches Zentrum für Luft- und Raumfahrt, Göttingen, Germany.
- [11] Ventakakrishnan, G. E., and Meier, G. E. A. (2004): Density Measurements Using the Background Oriented Schlieren Technique, pp. 237-247, Journal of Experiments in Fluids 37.
- [12] Reinholtz, C. K., Heltsley, F. L., Scott, K. E. (2010): Visualization of Jettison Motor Plumes from an Orion Launch Abort Vehicle Wind Tunnel Model Using Background-Oriented Schlieren, U.S. Air Force T&E Days 2010, 2-4 February, Nashville, Tennessee.
- [13] Wilson, R., E. (1980): Wind Turbine Aerodynamics, pp. 357-372, Journal of Industrial Aerodynamics 5.
- [14] Hand, M., M. (2003): Mitigation of Wind Turbine/Vortex Interaction Using Disturbance Accommodating Control, NREL/TP-500-35172, Technical Report of National Renewable Energy Laboratory (NREL).
- [15] Huang, A. (2011): Mind The Gap: Tip Leakage Vortex Dynamics and Cavitation in Axial Turbines, MSc Thesis in Aeronautics and Astronautics, Massachusetts Institute of Technology.
- [16] Dreyer, M. (2015): Investigation of the Wind Turbine Vortex Structure, PhD thesis in Hydrolic mechanics, École Polytechnique Fédérale de Lausanne (EPFL), Switzerland.
- [17] Rubinstein, R., and Greenberg, P. S. (1994): Rapid Inversion of Angular Deflection Data for Certain Axisymmetric Refractive Index Distributions, pp. 1141-1144, Journal of Applied Optics 33.
- [18] Hansen, O. L. H. (2008): Aerodynamics of Wind Turbines, Second edition, Published by Earthscan in the UK and USA.
- [19] Pedersen, T. F., and Antoniou, I. (1989): Visualization of Flow through a Stall Regulated Wind Turbine Rotor, pp. 83-89, European Wind Energy Conference and Exhibition, EWEC'89, Part 1, Peter Peregrinus Ltd., London.

## 7. Conclusions and future work

### 7.1 Conclusions

Vision technologies are improving and widely used in science and industry to monitor motion of an object. In the present thesis two modern vision technologies are developed and used to study wind turbines: stereo vision to study dynamics of a VAWT via operational modal analysis (OMA), and background-oriented schlieren method (BOS) to study tip vortices of a HAWT blades. After introducing the stereo vision technique and operational modal analysis, two main experiments are designed to prove the reliability of stereo vision in studying the dynamic behavior of the structures and investigate the challenges.

In the first experiment, the modal behavior of a Troposkien blade was studied by analyzing the displacement time series obtained by stereo vision. Two Basler cameras (acA2040-180km) were used to take pictures of the blade and a proper image processing algorithm was developed to obtain the displacement of 11 paper markers on half of the blade during the experiment time. Due to the hardware limitation, the displacements were acquired for about 9 seconds which is too short to be analyzed with OMA and within the short term measurement all the blade natural frequencies might not be excited. Thus an averaged approach of the covariance-driven SSI (SSI-COV) is developed to involve several measurements in the analysis. Therefore according to the spectra of the displacement time series, three short time series were chosen to cover the first four frequencies and their covariance matrices were averaged to be analysed with SSI-COV method. In addition, the blade was numerically simulated using COMSOL and also the classical modal analysis with hammering (EMA) was conducted on the blade to validate the stereo vision experiment. The first four natural frequencies from stereo vision experiment fairly agreed with simulation and EMA, with minor differences due to the assumptions in the simulation. During the processing the images and post processing the pixel information to get the 3D displacement, a few remarks were reached for improving the displacement measurement accuracy, such as the proper illumination with constant light intensity over the time to avoid reflection and shadows on the surface or changing the marker to a black circle with strong contrast with the background and with the size of 10-20 pixels in the image.

In the second experiment, the stereo vision was carried out in the wind tunnel of Politecnico Di Milano University to study the dynamic behavior of a 1 kW 3-bladed vertical axis wind turbine rotor during standstill. The black circles were printed on the long tapes with a distance of 10 cm and stuck to the blades and rotor shaft, and two Basler cameras recorded the displacement of the markers while the rotor was vibrating due to the wind at speed of 25 m/s. We also had hardware limitations regarding the data acquisition system in this experiment, therefore only a part of the rotor containing 2

blades and the rotor shaft were captured in the stereo images for about 30 s and the third blade dynamic behavior had to be predicted according to the simulations and aerodynamic loadings during the test. The data-driven SSI code was developed for OMA due to the good convergence and direct use of the measurement data. After analyzing the displacement time series by SSI the physical frequencies including structural modes, guy wire and vortex shedding frequencies were identified. To validate the structural modes and distinguish them from the other physical frequencies, the rotor structure was simulated with HAWC2 without considering aerodynamic interactions. The first 7 structural natural frequencies agreed well with the simulation results but the mode shapes were different because of the aerodynamics. For explaining the differences between the mode shapes, the lift and drag and consequently the edgewise and flatwise forces are estimated according to the angles of attack, and the resultant aerodynamic damping interpreted the differences. The dynamic behavior of the third mode was also predicted regarding to the HAWC2 simulations and estimated aerodynamic forces. The guy wire frequencies were identified as the harmonics of the first wire frequency and using the corresponding theoretical equation. The vortex shedding frequency behind the rotor shaft was also calculated using the dimensions and the wind speed which was compatible with one of the natural frequencies identified by SSI. The singular value plot is also obtained via developed FDD code to be compared with the SSI results. The peaks in the singular value plot confirmed the modes estimated by SSI, however for very closely spaced modes, the performance of the DD-SSI is better than FDD. Finally a classical modal analysis with PULSE measurement system was conducted on the rotor bolted to the floor in the workshop to verify the structural modes estimated with OMA. There were some differences between the identified natural frequencies due to the different boundary condition of the rotor in EMA test but with considering these differences the result of EMA and OMA are compatible.

After conducting the above-mentioned stereo vision experiments, the uncertainty of the measured displacement is evaluated by a generalized method based on the law of error propagation in a linear camera model of a stereo vision system. In this method, the uncertainty in stereo reconstruction propagates through two stages: calibrations of the cameras and the 3D triangulation to obtain the 3D coordinates from 2D projections in the images. In the blade experiment, three measurement sets were involved in operational modal analysis, the first and second had almost the same baseline length and the third one had a shorter baseline. Then the uncertainties associated with the first and third measured displacement time series were evaluated to investigate also the effect of baseline length. The mean value of the averaged uncertainty of all the points in  $x$ ,  $y$  and  $z$  direction is  $(\text{mean}(\text{mean}(u_x)) , \text{mean}(\text{mean}(u_y)) , \text{mean}(\text{mean}(u_z))) = (0.969, 0.453, 3.800)$  and  $(\text{mean}(\text{mean}(u_x)) , \text{mean}(\text{mean}(u_y)) , \text{mean}(\text{mean}(u_z))) = (0.387, 0.370, 0.972)$  mm for the first and third measurements respectively. The uncertainty for the blade experiment illustrates the importance of a number of factors to decrease the stereo reconstruction uncertainty, such as precision of the calibration grid

points, baseline length and the distance between the cameras and the object to be measured. These factors were considered in the VAWT experiment in wind tunnel with providing precise calibration grid and markers, increasing the base line length and decreasing the distance between the cameras and the rotor according to the existing restrictions to improve the accuracy of the displacement measurements. As the new markers were fully circular, the perspective error due to the 2D projection of the circle to an ellipse was corrected in the image processing algorithm to decrease the bias error. Finally the averaged of the mean uncertainty for all of the markers is:  $(\text{mean}(\text{mean}(u_x)), \text{mean}(\text{mean}(u_y)), \text{mean}(\text{mean}(u_z))) = (0.145, 0.456, 1.636) \text{ mm}$ .

In the last part of the thesis, the tip vortices behind a Nordtank HAWT are studied via the BOS method that is based on the density gradient in a transparent medium. In BOS a medium is located between a background and a camera. The density gradient of the medium changes the refractive index and it leads to a displacement of the background image on the camera sensor. The BOS experimental setup is quite simple compared to the other similar methods like Schlieren method and it does not need complicated equipment such as special cameras or seeded flow, thus it is a proper method to study large scale flows. However the Mach number in the current case (HAWT tip vortex) is about 0.19 which is significantly smaller than the other flows studied by BOS ( $\text{Ma} > 0.4$ ). Therefore detecting the displacement due to the density change in the current tip vortex is a serious challenge that requires considerable effort. To address this issue, the pixel displacement in the image due to the density change in the tip vortex is modeled using Rankine vortex assumption and several experimental setups were designed to make the pixel displacement visible. In the first setup the background pattern was installed on the turbine tower but the estimated pixel displacement due to the density change was too small for this setup. In the next setup the background was installed behind the turbine nacelle to increase pixel displacement by increasing the distance between the background and the tip vortex. This change made the estimated displacement about 7 times larger but still there was no displacement visible after processing the BOS images. As the density gradient in the tip vortex it not as strong as the high Mach number flows, we guessed that it might be washed away by the turbulence. Afterwards, we designed an LED array to conduct the experiment during a windy night when the atmosphere was more stable. The final experiment was carried out in a night with predicted maximum wind speed of 8-10 m/s and stable atmosphere. Before processing the images, the traveling path of the tip vortex behind the turbine was roughly estimated by knowing the yaw error and assuming it as a helical path. In the next step the projection of the helical path was found in the image using the camera calibration and the relative position of the LED array relative to the rotor center. Afterwards the averaged distances between the LED rows along the projected vortex line in the image were studied during the experiment time. It was observed that in a particular time period, the distance between the LEDs has changed successively. Therefore a model was devised to estimate the changes of the distance between LEDs due to the tip vortex passing through them.

The model result for different values of vortex core diameter was compared to the experimental observations in order to reach to a vortex size for which the experiment and the model agree together. Therefore the turbine tip vortex was found to have the core diameter of 20 *cm* and maximum pressure drop of 279 *Pa*.

## 7.2 Future work

Using displacement compared to the acceleration as output, has demonstrated easier, cheaper, and direct procedures. The current study shows the reliability of the stereo vision technique to study the dynamic behaviour of the large structures via obtaining the displacement time series. By upgrading the image acquisition system, the displacement measurement system can be used for modal identification and health monitoring of the large structures such as operating or parked horizontal axis wind turbines. In addition, by adding extra cameras, the displacements of more complicated structures such as VAWTs in operation can also be monitored.

In BOS study we have shown that this technique also works with lower Mach numbers compared to the other studies. We obtained quantitative information of the tip vortex behind a Nortank HAWT. This experiment can be even improved more by using larger backgrounds and having paper reflective markers on the pattern. Another improvement that can be made in the BOS experiment setup is providing a background with adjustable angle to avoid scattering of the light in the LED images when the pictures are taken from the side.

DTU Wind Energy is a department of the Technical University of Denmark with a unique integration of research, education, innovation and public/private sector consulting in the field of wind energy. Our activities develop new opportunities and technology for the global and Danish exploitation of wind energy. Research focuses on key technical-scientific fields, which are central for the development, innovation and use of wind energy and provides the basis for advanced education at the education.

We have more than 240 staff members of which approximately 60 are PhD students. Research is conducted within nine research programmes organized into three main topics: Wind energy systems, Wind turbine technology and Basics for wind energy.

---

**Technical University of Denmark**  
Department of Wind Energy  
Frederiksborgvej 399

Building 118

4000 Roskilde  
Denmark

Telephone 46 77 50 85

[info@vindenergi.dtu.dk](mailto:info@vindenergi.dtu.dk)  
[www.vindenergi.dtu.dk](http://www.vindenergi.dtu.dk)